Advances in Materials Science and Engineering

Development and Engineering Application of Large Deformation Strengthening Material for Geotechnical Engineering

Lead Guest Editor: Manchao He
Guest Editors: Ren Fuqiang and Hongyu Wang

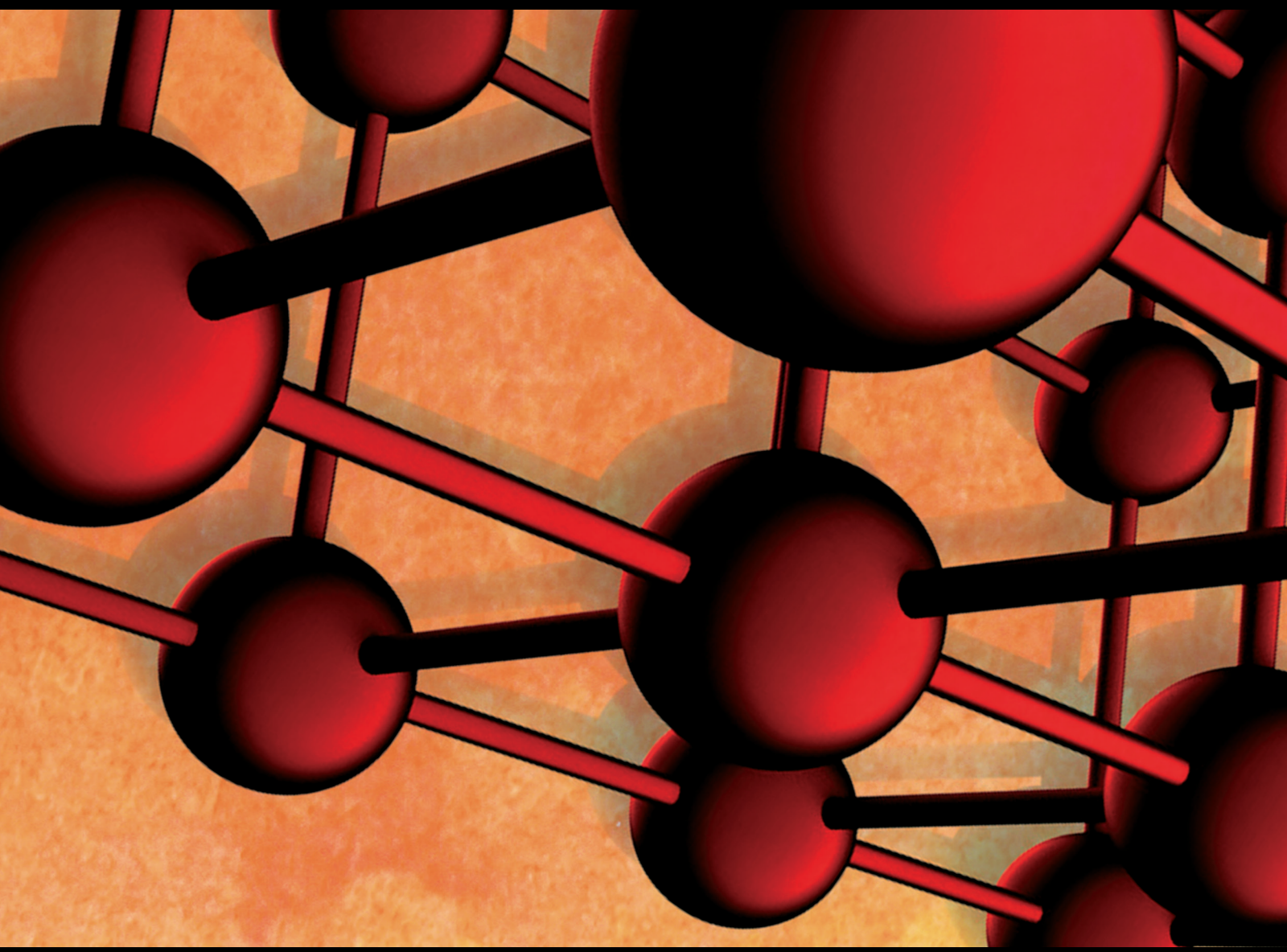

Development and Engineering Application of Large Deformation Strengthening Material for Geotechnical Engineering

Advances in Materials Science and Engineering

Development and Engineering Application of Large Deformation Strengthening Material for Geotechnical Engineering

Lead Guest Editor: Manchao He
Guest Editors: Ren Fuqiang and Hongyu Wang

Copyright © 2022 Hindawi Limited. All rights reserved.

This is a special issue published in “Advances in Materials Science and Engineering.” All articles are open access articles distributed under the Creative Commons Attribution License, which permits unrestricted use, distribution, and reproduction in any medium, provided the original work is properly cited.

Chief Editor

Amit Bandyopadhyay, USA

Associate Editors

Vamsi Balla, India
Mitun Das, USA
Sandip Harimkar, USA
Ravi Kumar, India
Peter Majewski, Australia
Enzo Martinelli, Italy
Luigi Nicolais, Italy
Carlos R. Rambo, Brazil
Michael J. Schütze, Germany
Kohji Tashiro, Japan
Zhonghua Yao, China
Dongdong Yuan, China
Wei Zhou, China

Academic Editors

Antonio Abate, Germany
Hany Abdo, Saudi Arabia
H.P.S. Abdul Khalil, Malaysia
Ismael alejandro Aguayo villarreal, Mexico
Sheraz Ahmad, Pakistan
Michael Aizenshtein, Israel
Jarir Aktaa, Germany
Bandar AlMangour, Saudi Arabia
Huaming An, China
Alicia Esther Ares, Argentina
Siva Avudaiappan, Chile
Habib Awais, Pakistan
NEERAJ KUMAR BHOI, India
Enrico Babilio, Italy
Renal Backov, France
M Bahubalendruni, India
Sudharsan Balasubramanian, India
Markus Bambach, Germany
Irene Bavasso, Italy
Stefano Bellucci, Italy
Brahim Benmokrane, Canada
Jean-Michel Bergheau, France
Guillaume Bernard-Granger, France
Giovanni Berselli, Italy
Patrice Berthod, France
Michele Bianchi, Italy
Hugo C. Biscaia, Portugal
Antonio Boccaccio, Italy
Mohamed Bououdina, Saudi Arabia
Gianlorenzo Bussetti, Italy
Antonio Caggiano, Germany
Marco Cannas, Italy
Qi Cao, China
Gianfranco Carotenuto, Italy
Paolo Andrea Carraro, Italy
Jose Cesar de Sa, Portugal
Wen-Shao Chang, United Kingdom
Qian Chen, China
Francisco Chinesta, France
Er-Yuan Chuang, Taiwan
Francesco Colangelo, Italy
María Criado, Spain
Enrique Cuan-Urquizo, Mexico
Lucas Da Silva, Portugal
Angela De Bonis, Italy
Abílio De Jesus, Portugal
José António Fonseca De Oliveira Correia, Portugal
Ismail Demir, Turkey
Luigi Di Benedetto, Italy
Maria Laura Di Lorenzo, Italy
Marisa Di Sabatino, Norway
Luigi Di Sarno, Italy
Ana María Díez-Pascual, Spain
Guru P. Dinda, USA
Hongbiao Dong, China
Mingdong Dong, Denmark
Frederic Dumur, France
Stanislaw Dymek, Poland
Kaveh Edalati, Japan
Philip Eisenlohr, USA
Luís Evangelista, Norway
Michele Fedel, Italy
Francisco Javier Fernández Fernández, Spain
Isabel J. Ferrer, Spain
Massimo Fresta, Italy
Samia Gad, Egypt
Pasquale Gallo, Finland
Sharanabasava Ganachari, India
Santiago Garcia-Granda, Spain
Carlos Garcia-Mateo, Spain

Achraf Ghorbal, Tunisia
Georgios I. Giannopoulos, Greece
Ivan Giorgio, Italy
Andrea Grilli, Italy
Vincenzo Guarino, Italy
Daniel Guay, Canada
Jenö Gubicza, Hungary
Xuchun Gui, China
Benoit Guiffard, France
Zhixing Guo, China
Ivan Gutierrez-Urrutia, Japan
Weiwei Han, Republic of Korea
Simo-Pekka Hannula, Finland
A. M. Hassan, Egypt
Akbar Heidarzadeh, Iran
Yi Huang, United Kingdom
Joshua Ighalo, Nigeria
Saliha Ilican, Turkey
Md Mainul Islam, Australia
Ilia Ivanov, USA
Jijo James, India
Hafsa Jamshaid, Pakistan
Hom Kandel, USA
Kenji Kaneko, Japan
Rajesh Kannan A, Democratic People's Republic of Korea
Mehran Khan, Hong Kong
Akihiko Kimura, Japan
Ling B. Kong, Singapore
Pramod Koshy, Australia
Hongchao Kou, China
Alexander Kromka, Czech Republic
Abhinay Kumar, India
Avvaru Praveen Kumar, Ethiopia
Sachin Kumar, India
Paweł Kłosowski, Poland
Wing-Fu Lai, Hong Kong
Luciano Lamberti, Italy
Fulvio Lavecchia, Italy
Laurent Lebrun, France
Joon-Hyung Lee, Republic of Korea
Cristina Leonelli, Italy
Chenggao Li, China
Rongrong Li, China
Yuanshi Li, Canada
Guang-xing Liang, China
Barbara Liguori, Italy
Jun Liu, China
Yunqi Liu, China
Rong Lu, China
Zhiping Luo, USA
Fernando Lusquiños, Spain
Himadri Majumder, India
Dimitrios E. Manolakos, Greece
Necmettin Maraşlı, Turkey
Alessandro Martucci, Italy
Roshan Mayadunne, Australia
Mamoun Medraj, Canada
Shazim A. Memon, Kazakhstan
Pratima Meshram, India
Mohsen Mhadhbi, Tunisia
Philippe Miele, France
Andrey E. Miroshnichenko, Australia
Ajay Kumar Mishra, South Africa
Hossein Moayedi, Vietnam
Dhanesh G. Mohan, United Kingdom
Sakar Mohan, India
Namdev More, USA
Tahir Muhmood, China
Faisal Mukhtar, Pakistan
Dr. Tauseef Munawar, Pakistan
Roger Narayan, USA
Saleem Nasir, Pakistan
Elango Natarajan, Malaysia
Rufino M. Navarro, Spain
Miguel Navarro-Cia, United Kingdom
Behzad Nematollahi, Australia
Peter Niemz, Switzerland
Hiroshi Noguchi, Japan
Dariusz Oleszak, Poland
Laurent Orgéas, France
Togay Ozbakkaloglu, United Kingdom
Marián Palcut, Slovakia
Davide Palumbo, Italy
Gianfranco Palumbo, Italy
Murlidhar Patel, India
Zbyšek Pavlík, Czech Republic
Alessandro Pegoretti, Italy
Gianluca Percoco, Italy
Andrea Petrella, Italy

Claudio Pettinari, Italy
Giorgio Pia, Italy
Candido Fabrizio Pirri, Italy
Marinos Pitsikalis, Greece
Alain Portavoce, France
Simon C. Potter, Canada
Ulrich Prahl, Germany
Veena Ragupathi, India
Kawaljit singh Randhawa, India
Baskaran Rangasamy, Zambia
Paulo Reis, Portugal
Hilda E. Reynel-Avila, Mexico
Yuri Ribakov, Israel
Aniello Riccio, Italy
Anna Richelli, Italy
Antonio Riveiro, Spain
Marco Rossi, Italy
Fernando Rubio-Marcos, Spain
Francesco Ruffino, Italy
Giuseppe Ruta, Italy
Sachin Salunkhe, India
P Sangeetha, India
Carlo Santulli, Italy
Fabrizio Sarasini, Italy
Senthil Kumaran Selvaraj, India
Raffaele Sepe, Italy
Aabid H Shalla, India
Poorva Sharma, China
Mercedes Solla, Spain
Tushar Sonar, Russia
Donato Sorgente, Italy
Charles C. Sorrell, Australia
Damien Soulat, France
Adolfo Speghini, Italy
Antonino Squillace, Italy
Koichi Sugimoto, Japan
Jirapornchai Suksaeree, Thailand
Baozhong Sun, China
Sam-Shajing Sun, USA
Xiaolong Sun, China
Yongding Tian, China
Hao Tong, China
Achim Trampert, Germany
Tomasz Trzepieciński, Poland
Kavimani V, India
Matjaz Valant, Slovenia
Mostafa Vamegh, Iran
Lijing Wang, Australia
Jörg M. K. Wiezorek, USA
Guosong Wu, China
Junhui Xiao, China
Guoqiang Xie, China
YASHPAL YASHPAL, India
Anil Singh Yadav, India
Yee-wen Yen, Taiwan
Hao Yi, China
Wenbin Yi, China
Tetsu Yonezawa, Japan
Hiroshi Yoshihara, Japan
Bin Yu, China
Rahadian Zainul, Indonesia
Lenka Zaji#c#kova#, Czech Republic
Zhigang Zang, China
Michele Zappalorto, Italy
Gang Zhang, Singapore
Jinghuai Zhang, China
Zengping Zhang, China
You Zhou, Japan
Robert Černý, Czech Republic

Contents

Steel Wire Mechanical Property Degradation Study Based on Numerical Simulation
Jiangjiang Li and Xuanyu Zhang
Research Article (11 pages), Article ID 2207585, Volume 2022 (2022)

Study on the Law of Rock Anelastic Recovery and the Characteristics of In Situ Stress Field of 2000 m Deep Stratum in Metal Mines of Coastal Area
Yuezheng Zhang, Hongguang Ji, and Hanhua Xu
Research Article (11 pages), Article ID 2152814, Volume 2022 (2022)

Strength Characteristics and Failure Mechanism of Granite with Cross Cracks at Different Angles Based on DIC Method
Xu Wu, Liyuan Zhang, Jinglai Sun, Qifeng Guo, Jiliang Pan, and Jun Gao
Research Article (9 pages), Article ID 9144673, Volume 2022 (2022)

Analysis of Instability Mechanism and Induced Cause of Urban Pavement in Xining City, China
Gan Qi, Zhenyu Wang, Yu Chen, Chun Zhu, Dazhong Ren, Tao Tian, and Fu Yang
Research Article (12 pages), Article ID 3365402, Volume 2022 (2022)

Fractal Study on the Failure Evolution of Concrete Material with Single Flaw Based on DIP Technique
Lulin Zheng, Hao Liu, Yujun Zuo, Quanping Zhang, Wei Lin, Qing Qiu, Xiaorong Liu, and Ziqi Liu
Research Article (15 pages), Article ID 6077187, Volume 2022 (2022)

Monitoring and Analysis of a High-Performance Concrete Shaft Lining: A Case Study
Daolu Quan, Hongguang Ji, Xiaobo Su, Hui Cao, and Juanhong Liu
Research Article (11 pages), Article ID 7692772, Volume 2022 (2022)

Predicting the Remaining Service Life of Civil Airport Runway considering Reliability and Damage Accumulation
Baoli Wei and Chengchao Guo
Research Article (11 pages), Article ID 6494812, Volume 2022 (2022)

Hindawi
Advances in Materials Science and Engineering
Volume 2022, Article ID 2207585, 11 pages
https://doi.org/10.1155/2022/2207585

Research Article

Steel Wire Mechanical Property Degradation Study Based on Numerical Simulation

Jiangjiang Li[1,2] **and Xuanyu Zhang**[3]

[1]*School of Highway, Chang'an University, Xi'an, Shaanxi 710064, China*
[2]*Middle Section of the South Second Ring Road, Xi'an, Shaanxi 710064, China*
[3]*Shandong Hi-Speed Company Limited, Long'ao North Road, Jinan, Shandong 250000, China*

Correspondence should be addressed to Jiangjiang Li; lijiangjilin@chd.edu.cn

Received 8 March 2022; Revised 8 April 2022; Accepted 11 April 2022; Published 9 June 2022

Academic Editor: REN Fuqiang

Copyright © 2022 Jiangjiang Li and Xuanyu Zhang. This is an open access article distributed under the Creative Commons Attribution License, which permits unrestricted use, distribution, and reproduction in any medium, provided the original work is properly cited.

With the rapid development of underground engineering construction, such as deep mining of mineral resources and tunnel excavation under complex geological conditions, the existing support methods cannot meet the deformation requirements. It is necessary to conduct in-depth research on the stress status and damage evolution of the hanger rods, to establish a theoretical basis for the design principles and criteria of key components. In this paper, the degradation law of the mechanical properties of the hanger steel wire with the degree of corrosion is analyzed in detail. The results show that the corrosion changes the geometry of the cross section of the steel wire, which leads to the degradation of the mechanical properties of the steel wire. With the increase of corrosion length and depth, the strength, stiffness, and ultimate strain of the steel wire are reduced to varying degrees, and the effect of pitting corrosion is more significant than that of uniform corrosion. The closer the holes are, the greater the corrosion effect is.

1. Introduction

Since the 1980s, with the development of large-scale highway and urban construction, the construction of highways and urban bridges, mining of mineral resources, and excavation of tunnels have been greatly developed in our country [1–5]. Steel wire is commonly used in many engineering fields, such as tunnel excavation, underground space structure, and so on [6, 7]. According to the "2006 Statistical Bulletin on the Development of Highway and Waterway Transportation Industry" of the Ministry of Communications, by the end of 2006, the total number of highway bridges in China had reached 533,600, with a total of 20,399,100 meters, including 1,036 extra-large bridges, 1,714,500 meters, and 30,982 bridges, 6,385,800 meters. There are 121,100 middle bridges, but the cross-section is still circular [8–10]. A large number of representative world-class bridges have been built over the Yangtze River, Yellow River, Pearl River, and other major rivers and coastal waters.

However, with the rapid development of bridge construction in China, the destruction of bridges during construction or operation also occurs from time to time, resulting in heavy casualties and property losses, as well as extremely bad social impacts. Among the bridge damage accidents in the past ten years, the middle and bottom-bearing arch bridges are the worst. Among them, the bridge decks of the Yibin Nanmen Bridge in Sichuan (Figure 1(a)) and the Xinjiang Kongque River Bridge (Figure 1(b)) collapsed in 2001 and 2011, respectively.

From the analysis of the existing accident causes, in addition to factors such as construction, material quality, and overloading, another important reason is the lack of a deep enough understanding of the structural mechanical behavior and damage mechanism of middle and bottom-bearing arch bridges [11–17]. Based on the ANSYS finite element software, this study simulates the effects of uniform corrosion and pitting corrosion on the mechanical properties of the steel wire and analyzes the degradation law of the mechanical properties of the steel wire under different

(a) (b)

Figure 1: Damage forms of different bridge decks.

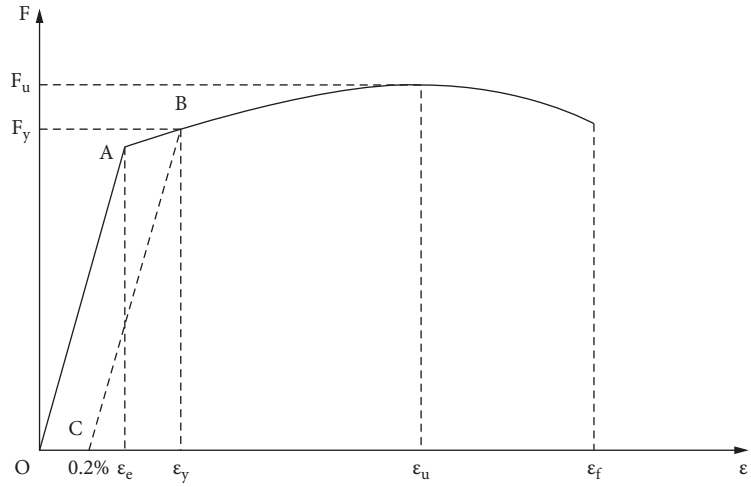

Figure 2: F-ε curve of steel wire and the mechanical meaning of each symbol.

corrosion depths or lengths [18]. Before discussing the degradation law of the mechanical properties of the steel wire with the degree of corrosion, the symbols in this study are explained in Figure 2 [19–23].

2. Stress-Strain Relationship of Damaged Steel Wire

With the increase of corrosion degree, the mechanical properties such as stiffness, strength, and ultimate strain of steel wire will be reduced to different degrees. After analyzing the results of tensile tests of damaged steel wires, Elachachi et al. proposed the following constitutive relation [24]:

$$\begin{cases} \sigma = Ee, & 0 < \varepsilon \le E_e, \\ E - \sigma_e + \dfrac{E(\varepsilon - \varepsilon_e)}{1 + C(\varepsilon - \varepsilon_e)}, & \varepsilon \le \varepsilon \le \varepsilon_f, \end{cases} \tag{1}$$

where $c = E\varepsilon L_u - \sigma_u / (\sigma_u - \sigma_e)(\varepsilon_u \varepsilon_e)$.

In order to study the degradation law of mechanical properties of steel wire, Xu [25] conducted corrosion detection and monotonic tensile tests on damaged steel wires. Two data reflecting the corrosion degree of steel wire are obtained by testing: the average diameter d_{mean} (reflects the average corrosion degree of steel wire specimens) and the minimum diameter $d_{\min}$ (reflects the local corrosion degree of the steel wire specimen). Also, four mechanical performance parameters of each damaged steel wire including yield bearing capacity F_y, yield strain ε_y, ultimate bearing capacity F_u, and ultimate strain ε_y were measured by tensile tests. It can be seen from the test results that the constitutive relation of each damaged steel wire basically conforms to equation (1). The force-strain curves of some steel wires under different corrosion grades are plotted in Figure 3.

It can be seen that with the increase of the degree of corrosion, the mechanical properties such as stiffness, strength, and ultimate strain of the steel wire are reduced to varying degrees. The changing law is shown in Figures 4(a)–4(e).

It can be seen from Figure 4 that the axial stiffness of the steel wire decreases nonlinearly with the increase of the corrosion degree. There is an approximately linear relationship between yield capacity and ultimate capacity and minimum diameter. When $d_{\min}$ changed from 5.00 mm to 2.94 mm, F_y decreased from 29.06 kN to 15.15 kN, a decrease of 47.87%; F_u decreased from 33.41 kN to 17.28 kN, a decrease of 48.28%. The ultimate strain ε_u decreases linearly with the decrease of the minimum diameter $d_{\min}$ of the steel

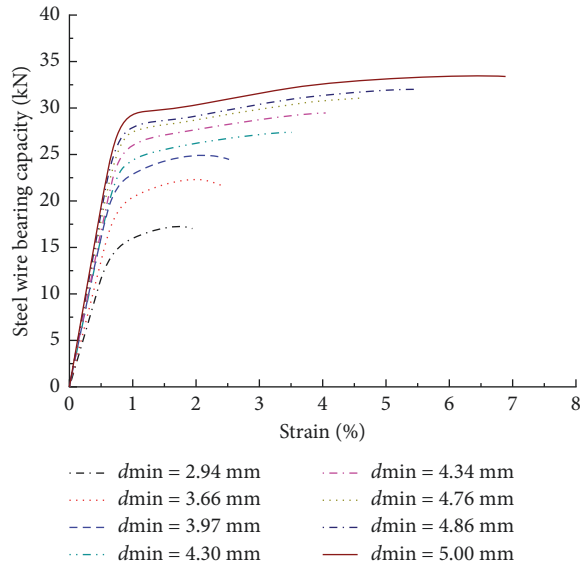

Figure 3: Bearing capacity-strain curve of damaged steel wire.

wire, and the relationship between the two can be approximated by an exponential function, as shown in the following equation:

$$\varepsilon_u = 1.9591 + 3.43542 \times 10^{-4} e^{d\,\min/0.52505}. \quad (2)$$

3. Establishment of Finite Element Model of Damaged Steel Wire

Both uniform corrosion and pitting corrosion change the cross-sectional geometry of the steel wire, but their contributions to the brittle fracture of the steel wire are not the same. Uniform corrosion uniformly reduces the area of the cross section of the wire, but the cross section is still circular and it only changes the cylindrical shape of the wire in the longitudinal direction. The local pitting corrosion changes the cross section of the steel wire due to the formation of local corrosion pits on the surface of the steel wire, so that the cross section changes from circular to noncircular. The authors in [26–29] pointed out that the ultimate ductility of high-strength steel wire is determined by the geometry of the steel wire, and the change of the cross-sectional geometry of the steel wire is determined by the degree of uniform corrosion and pitting corrosion. When the geometry of the longitudinal cylinder of the steel wire changes due to uniform corrosion, the ultimate ductility of the steel wire decreases, and the fracture originates at the center of the cross section and then spreads to the outer surface. When corrosion holes are formed on the surface of the steel wire, the ultimate ductility of the steel wire decreases more, and the fracture originates from the deepest corrosion hole on the surface of the steel wire.

Corrosion not only results in a reduction in the ductility of the wire but also results in a reduction in its strength and stiffness. The authors in [26, 30, 31] only considered ductility reduction when simulating steel wire corrosion, and their research conclusions need to be further expanded. On the basis of that research, this section also considers the influence of ductility reduction, strength reduction, and stiffness reduction of steel wire to study and discuss the degradation law of the mechanical properties of damaged steel wire in the section of the boom.

3.1. Defining Model Types, Element Types, and Material Properties. The steel wire adopts SOLID45 three-dimensional solid element, and the yield criterion adopts von Mises yield criterion [32]. According to this yield criterion, the critical shear stress of the steel wire under uniaxial tension is taken as $\sigma_y/3$ (σ_y is the yield stress of the wire).

3.2. Establishing a Steel Wire Model. The finite element model was first established with intact steel wire, with a length of 25.4 cm and a diameter of 4.877 mm. The corrosion section is located in the middle section of the steel wire and has a length of 5 mm. The steel wire can be divided into 16 segments longitudinally, and the dimensions are 4×31.115 mm + 8×0.625 mm + 4×31.115 mm. Among them, the middle 8 sections are used to simulate uniform corrosion and pitting corrosion. The cross section of the steel wire is composed of the following parts: (1) 16 square units in the middle with an area of 1.016 mm × 1.016 mm; (2) 4 inner rings to the outer diameter of 2.131 mm; (3) 6 intermediate rings to an outer diameter of 2.371 mm; and (4) 8 outer rings to the 2.438 mm outer diameter. In the model, 8 outer rings are used to simulate uniform corrosion, and 6 middle rings are used to simulate pitting corrosion. The geometric model and meshing of the steel wire are shown in Figure 5, and the total number of elements is 9216.

3.3. Simulation of Corrosion in the Model. In the finite element model of steel wire, the stress concentration at the crack tip is ignored, and the change of material properties caused by hydrogen embrittlement is not considered. Using the accelerated corrosion test data of high-strength steel wire in the literature [26], that is, the uniform corrosion rate of 0.0838 μm/h, the pitting corrosion rate is taken as 0.3848 μm/h. To analyze the effect of pitting pits and irregularities in the geometry of the wire section, 4 different corrosion conditions were simulated:

(1) A, uniform corrosion and pitting corrosion in the direction of 0° of the cross section.

(2) B, uniform corrosion and pitting corrosion in the direction of 0° and 90° of the cross section.

(3) C, uniform corrosion and pitting corrosion of 0° and 90° of the cross section.

(4) D, uniform corrosion + pitting corrosion at 3 points of 0°, 45°, and 90° of the cross section.

The solid model of the steel wire does not consider the large strain property, and the material nonlinearity adopts the multilinear isotropic strengthening stress-strain relationship MISO. The ultimate strain of the steel wire is taken as 5.7%, and all elements whose strain exceeds the ultimate strain are passivated, that is, multiplying their stiffness by

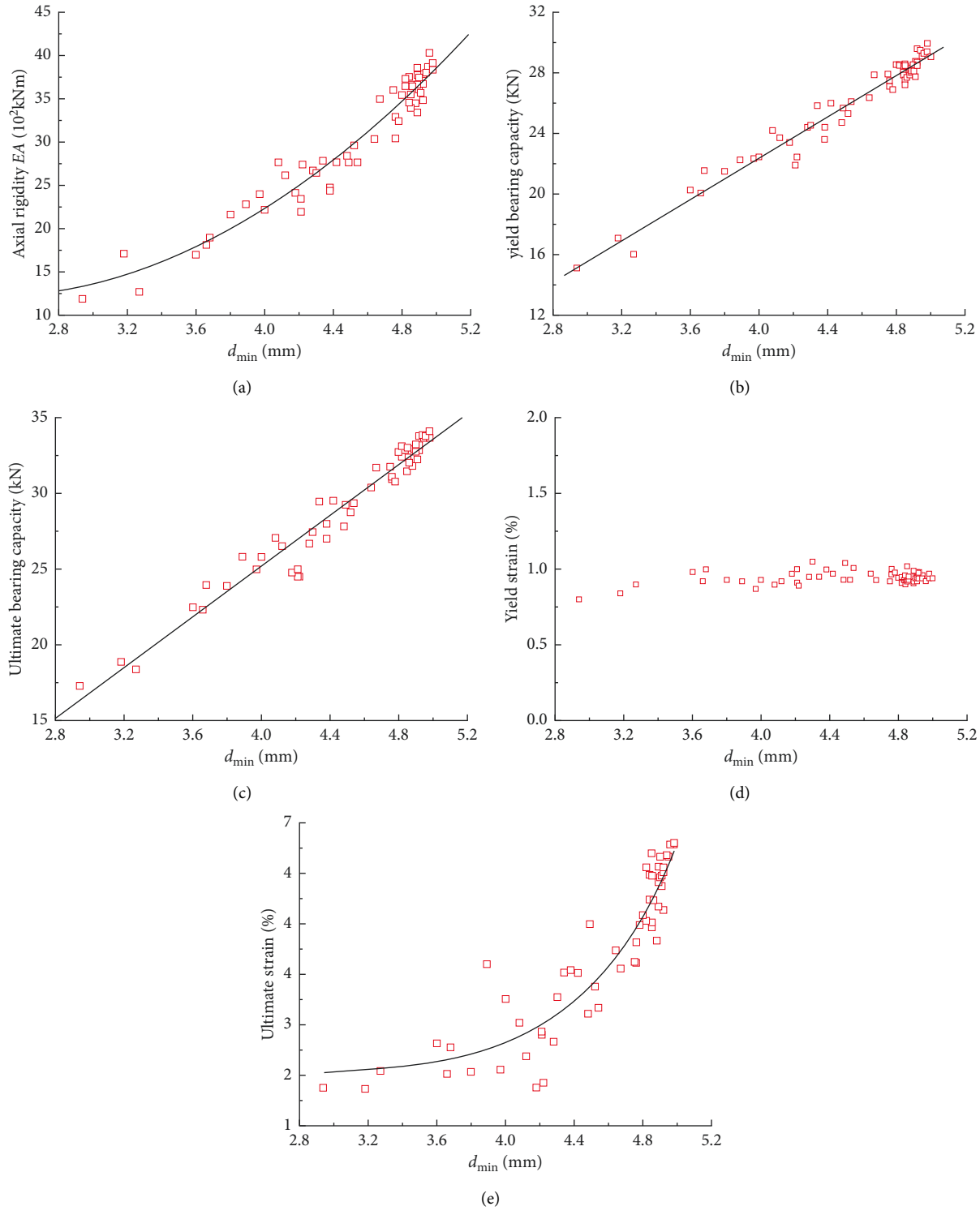

Figure 4: Change law of different mechanical parameters. (a) Axial stiffness degradation. (b) Yield bearing capacity degradation. (c) Deterioration of ultimate bearing capacity. (d) Yield strain degradation. (e) Ultimate strain degradation.

1.0×10^{-5}. When the nonlinear solution converges, if no element is passivated, the end displacement is increased by 0.01 and the solution is continued; if any element is passivated, the end displacement is not increased and the solution is continued. This cycle is repeated until the whole wire breaks.

4. The Effect of Uniform Corrosion on the Mechanical Properties of Steel Wire

The uniform corrosion conditions of different corrosion lengths and depths were simulated, respectively (32 models in total), and the ultimate strain of the steel wire under each

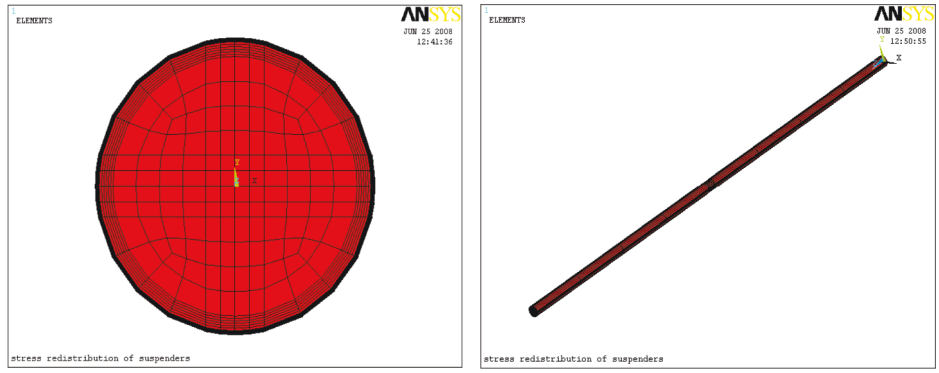

Figure 5: Wire model and meshing diagram.

Table 1: Ultimate strain of steel wire under uniform corrosion.

Corrosion time (h)	Corrosion length (mm)	Corrosion depth (mm)	Ultimate strain	Corrosion time (h)	Corrosion length (mm)	Corrosion depth (mm)	Ultimate strain
100	1.25	0.008	0.046	500	1.25	0.042	0.041
	2.50	0.008	0.045		2.50	0.042	0.038
	3.75	0.008	0.044		3.75	0.042	0.037
	5.00	0.008	0.044		5.00	0.042	0.033
200	1.25	0.017	0.045	600	1.25	0.05	0.039
	2.50	0.017	0.044		2.50	0.05	0.036
	3.75	0.017	0.043		3.75	0.05	0.034
	5.00	0.017	0.042		5.00	0.05	0.031
300	1.25	0.025	0.043	700	1.25	0.059	0.037
	2.50	0.025	0.042		2.50	0.059	0.034
	3.75	0.025	0.041		3.75	0.059	0.032
	5.00	0.025	0.038		5.00	0.059	0.029
400	1.25	0.034	0.043	800	1.25	0.067	0.036
	2.50	0.034	0.04		2.50	0.067	0.033
	3.75	0.034	0.038		3.75	0.067	0.031
	5.00	0.034	0.036		5.00	0.067	0.027

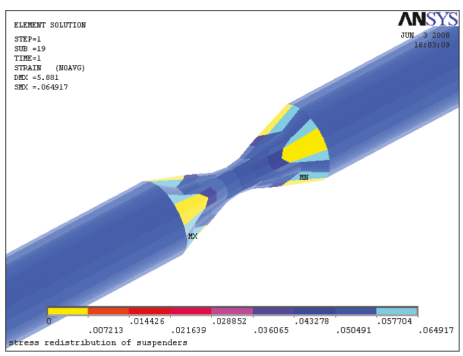

Figure 6: "Cup-cone" fracture of the uniformly corroded steel wire.

working condition is shown in Table 1. The data show that the ultimate strain of steel wire not only decreases with the extension of the uniform corrosion length but also decreases with the increase of the uniform corrosion depth. When the steel wire is intact, the fracture type is a cup-cone fracture (see Figure 6); when the steel wire is uniformly corroded, the fracture originates from the center of the wire and then expands outward, with the fracture retaining the cup-cone shape.

4.1. Influence of Uniform Corrosion Depth on Mechanical Properties of Steel Wire. Under the condition of uniform corrosion at different depths, the evolution law of mechanical properties of steel wire is shown in Figures 7 and 8.

It can be clearly seen from Figures 7 and 8 that when the uniform corrosion depth of the steel wire gradually develops from 8.38 (100 h) to 0.067 mm (800 h), the ultimate strain of the steel wire decreases nonlinearly, from 0.046 to 0.027, but the reduction in the strength and stiffness of the steel wire is not significant. At the same time, with the increase of the uniform corrosion depth, the cross section of the steel wire becomes smaller, and its cross section shape is still circular. Because the brittle fracture of the steel wire is greatly affected by the change of the geometric shape of the steel wire cross section, the brittle fracture mechanism of the steel wire does not change under the condition of uniform corrosion at different depths, and it all originates from the center of the steel wire cross section, which is a cup-cone fracture.

4.2. Influence of Uniform Corrosion Length on Mechanical Properties of Steel Wire. Under the condition of uniform corrosion of different lengths, the evolution law of mechanical properties of steel wire is shown in Figures 9 and 10.

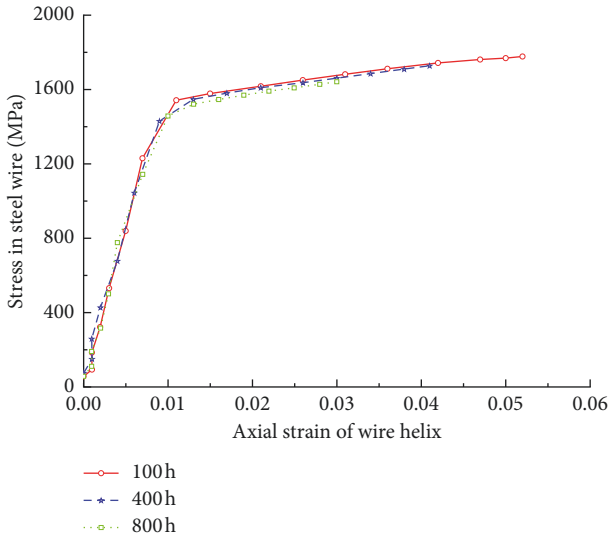

Figure 7: Effect of uniform corrosion depth on mechanical properties of steel wire.

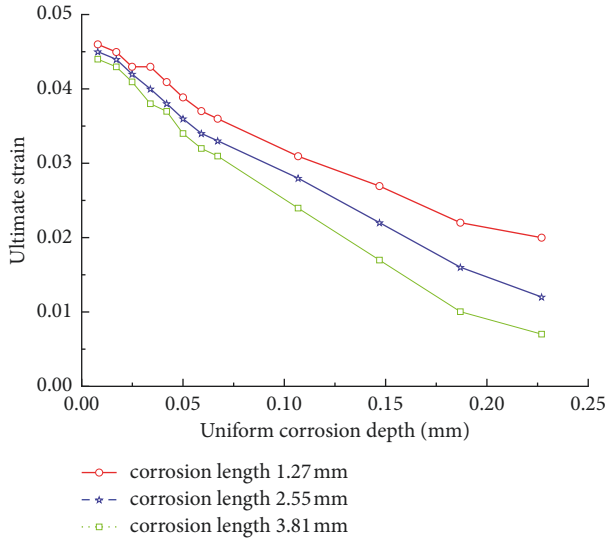

Figure 8: Influence of uniform corrosion depth on ultimate strain of steel wire.

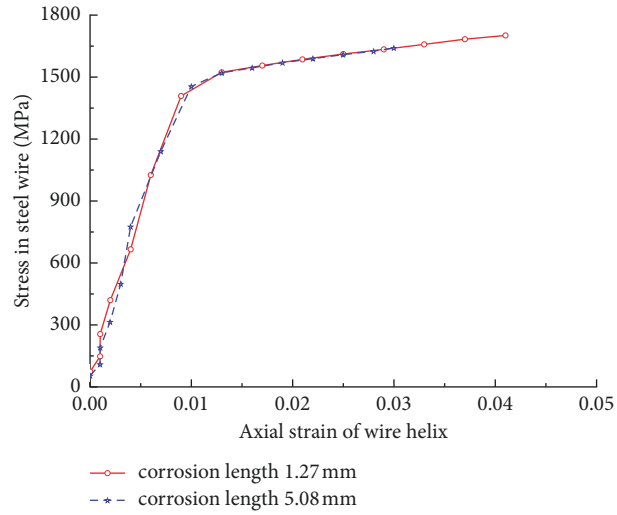

Figure 9: Effect of uniform corrosion depth on mechanical properties of steel wire.

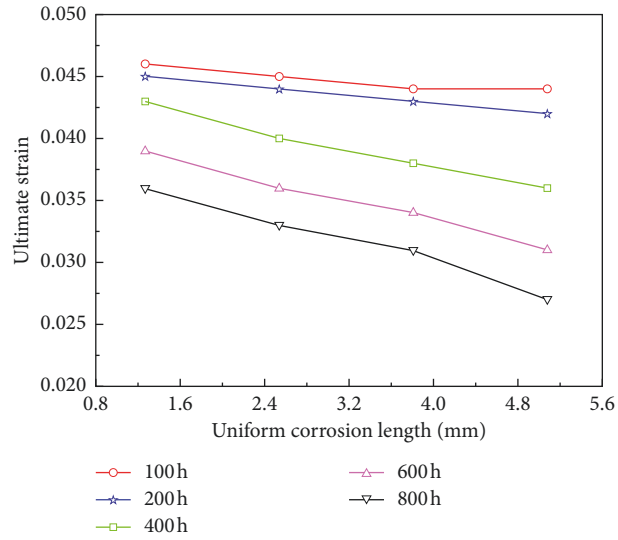

Figure 10: Influence of uniform corrosion depth on ultimate strain of steel wire.

It can be seen from the figures that when the uniform corrosion length of the steel wire gradually develops from 1.25 mm to 5.00 mm, the ultimate strain of the steel wire basically decreases linearly. Compared with the effect of corrosion depth, under the condition of uniform corrosion of different lengths, the reduction in strength and stiffness of steel wire is less obvious.

5. Influence of Pitting Corrosion on Mechanical Properties of Steel Wire

Table 2 shows the simulation results of the ultimate strain of the steel wire under different length and depth pitting corrosion conditions. The results show that the mechanical properties of the steel wire not only decrease with the extension of the pitting corrosion length but also decrease with the increase of the pitting corrosion depth, and with the increase of the number of corrosion holes, the mechanical properties of the steel wire decrease more, but not significantly. Pitting corrosion results in a significant change in the cross-sectional geometry of the steel wire, from circular to noncircular. Therefore, compared with uniform corrosion, the mechanical properties of the steel wire decrease more, and the brittle fracture mechanism also changes, which originates from the corrosion holes on the surface of the steel wire.

5.1. Influence of Pitting Depth on Mechanical Properties of Steel Wire. The evolution law of mechanical properties of steel wire under different depth pitting corrosion conditions is shown in Figures 11 and 12.

Table 2: Ultimate strain of steel wire under pitting corrosion at different positions.

Corrosion time (h)	Pitting length (mm)	Pitting depth (mm)	Ultimate strain under each working condition				
			A	B	C	D	Average value
100	1.25	0.038	0.046	0.046	0.045	0.044	0.045
	2.50	0.038	0.045	0.045	0.043	0.043	0.044
	3.75	0.038	0.045	0.044	0.042	0.042	0.043
	5.00	0.038	0.048	0.048	0.047	0.045	0.047
200	1.25	0.077	0.042	0.040	0.050	0.038	0.043
	2.50	0.077	0.040	0.039	0.037	0.035	0.038
	3.75	0.077	0.039	0.038	0.036	0.034	0.037
	5.00	0.077	0.047	0.045	0.043	0.037	0.043
300	1.25	0.115	0.038	0.038	0.034	0.033	0.036
	2.50	0.115	0.036	0.035	0.032	0.031	0.034
	3.75	0.115	0.035	0.034	0.031	0.030	0.033
	5.00	0.115	0.045	0.039	0.035	0.031	0.038
400	1.25	0.154	0.033	0.033	0.030	0.029	0.031
	2.50	0.154	0.033	0.031	0.028	0.027	0.030
	3.75	0.154	0.033	0.031	0.028	0.026	0.030
	5.00	0.154	0.041	0.035	0.031	0.025	0.033
500	1.25	0.192	0.031	0.031	0.026	0.025	0.028
	2.50	0.192	0.030	0.028	0.024	0.022	0.026
	3.75	0.192	0.030	0.027	0.024	0.021	0.026
	5.00	0.192	0.038	0.032	0.028	0.021	0.030
600	1.25	0.230	0.028	0.028	0.024	0.022	0.026
	2.50	0.230	0.028	0.027	0.021	0.019	0.024
	3.75	0.230	0.028	0.026	0.021	0.018	0.023
	5.00	0.230	0.036	0.029	0.024	0.018	0.027
700	1.25	0.269	0.027	0.025	0.022	0.020	0.024
	2.50	0.269	0.026	0.024	0.020	0.017	0.022
	3.75	0.269	0.027	0.024	0.020	0.016	0.022
	5.00	0.269	0.034	0.026	0.020	0.016	0.024
800	1.25	0.307	0.029	0.028	0.020	0.019	0.024
	2.50	0.307	0.031	0.028	0.019	0.016	0.024
	3.75	0.307	0.032	0.025	0.018	0.014	0.022
	5.00	0.307	0.032	0.023	0.018	0.013	0.022

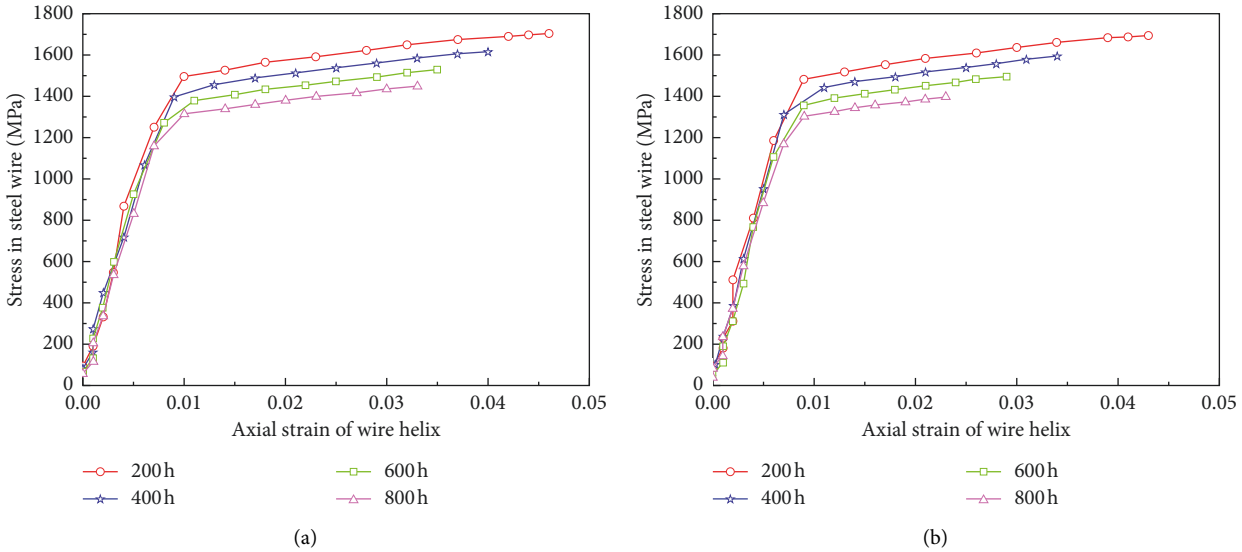

Figure 11: Continued.

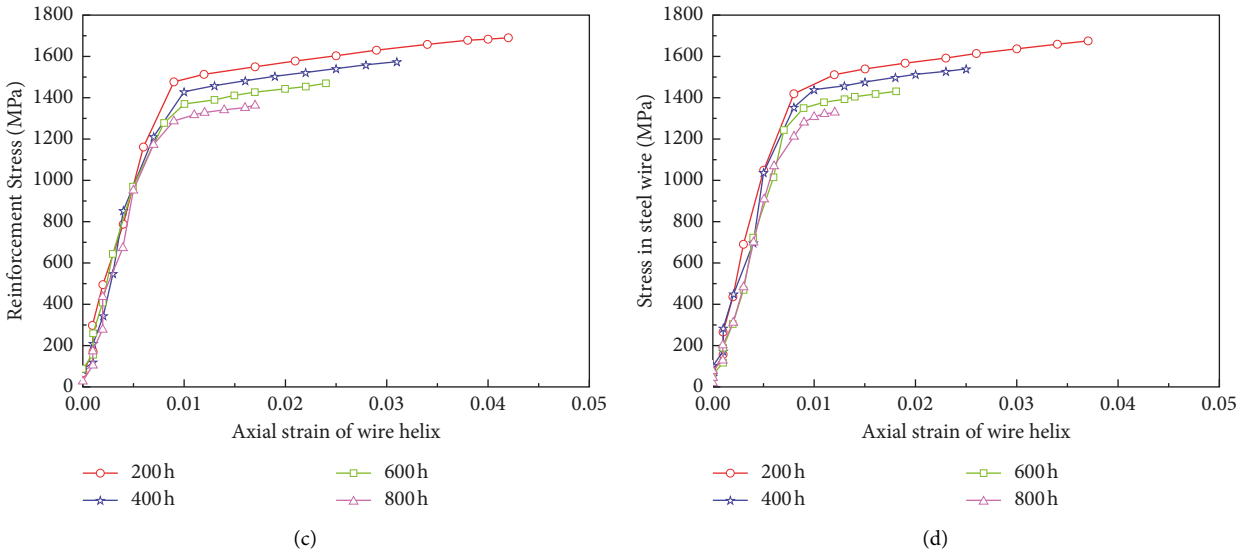

Figure 11: Changes in mechanical properties of steel wire at different depths of pitting corrosion.

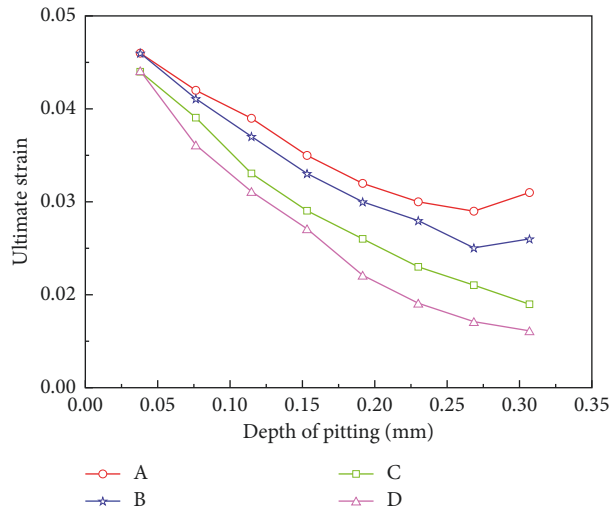

Figure 12: Influence of pitting depth on the ultimate strain of steel wire.

It can be seen from the figures that when the pitting corrosion depth of the steel wire gradually develops from 0.03848 mm (100 h) to 0.3078 mm (800 h), the ultimate strain, strength, and stiffness of the steel wire are reduced to varying degrees. When the steel wire has one corrosion hole, the impact of pitting depth on the mechanical properties of the steel wire is relatively minimal; when there are two corrosion holes, the effect is centered, but the closer the corrosion holes are, the greater the impact is; when there are three corrosion holes, the impact is the greatest.

Under the same corrosion depth, pitting corrosion has a greater impact on the mechanical properties of the steel wire than uniform corrosion. At the same time, with the increase of pitting corrosion depth, the cross-sectional geometry of the steel wire changes greatly, and the brittle fracture mechanism of the steel wire changes: the fracture originates from the deepest corrosion hole on the surface of the steel wire.

5.2. Effect of Pitting Corrosion Length on Mechanical Properties of Steel Wire. In the case of pitting corrosion of different lengths, the evolution law of the mechanical properties of the steel wire is shown in Figures 13 and 14.

It can be seen from the figures that when the uniform corrosion length of the steel wire gradually develops from 1.25 mm to 5.00 mm, the ultimate strain, strength, and stiffness of the steel wire all have a certain amount of reduction, but it is not significant. Compared with the corrosion conditions A~D, the effect of pitting corrosion length on the mechanical properties of the steel wire has little difference. At the same time, the impact of the pitting corrosion length on the mechanical properties of the steel wire is much smaller than that of the pitting corrosion depth, which indicates that the pitting corrosion depth and location of the steel wire are much smaller. The impact on its brittle fracture is obvious.

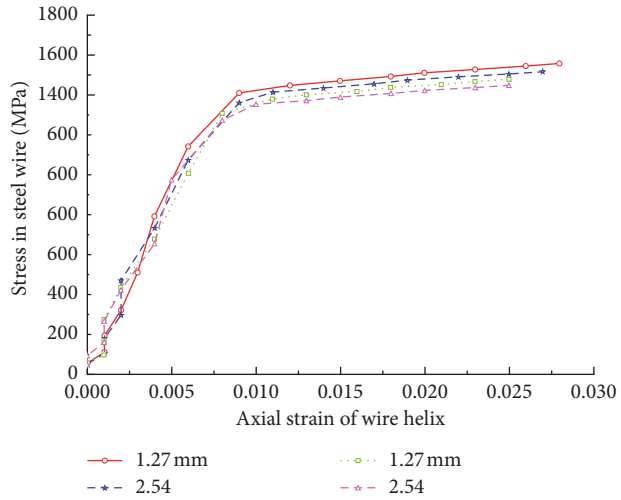

Figure 13: Influence of pitting corrosion length on mechanical properties of steel wire (condition D).

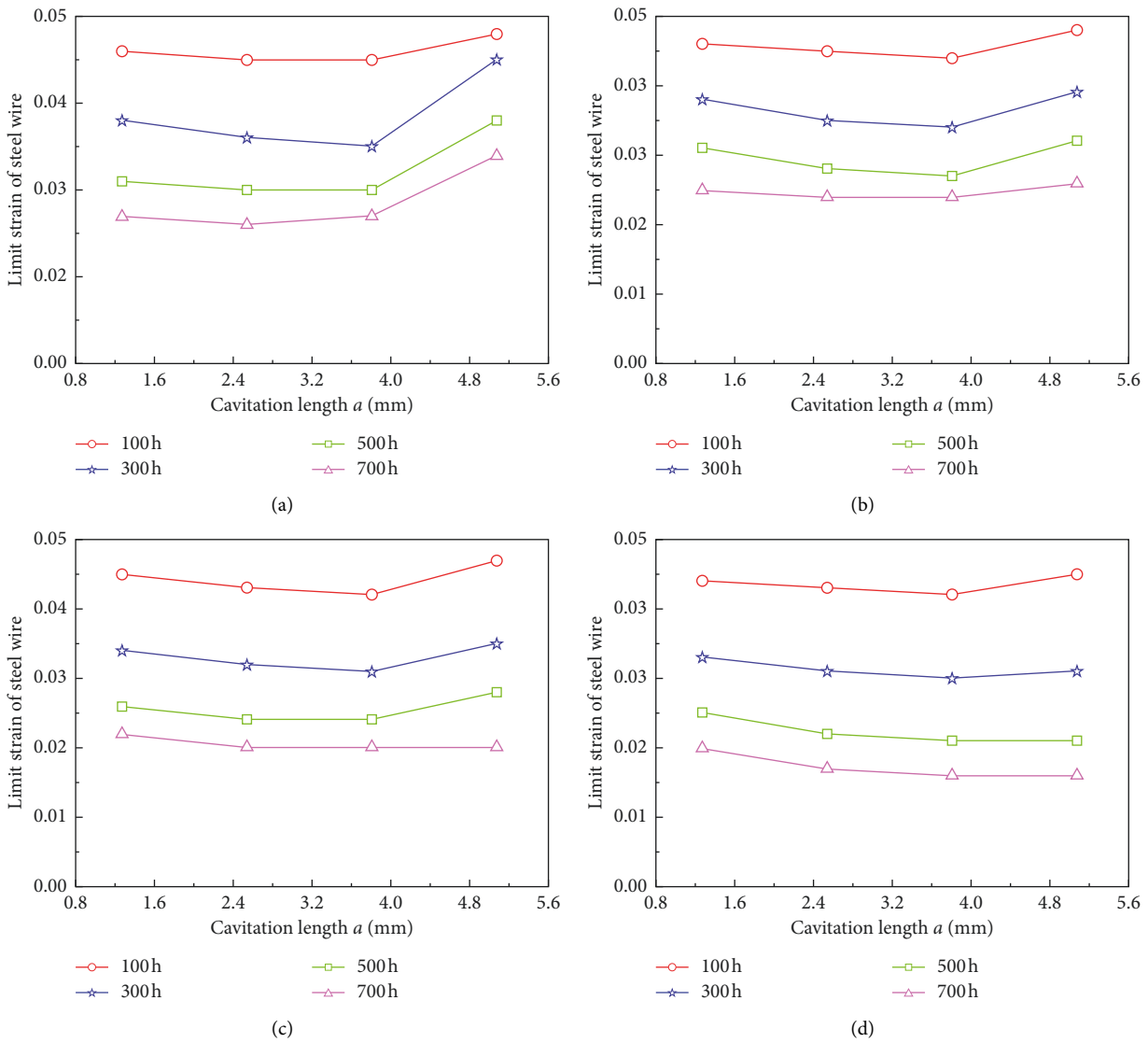

Figure 14: Influence of pitting length on the ultimate strain of steel wire under different working conditions.

6. Conclusion

In this paper, based on the ANSYS finite element platform, the degradation law of the mechanical properties of the hanger steel wire with the degree of corrosion is analyzed. Based on the simulations, we draw the following conclusions:

(1) The geometry of the cross section of the steel wire is one of the key factors leading to the degradation of the mechanical properties of the steel wire. The change of the geometry of the cross section of the steel wire is mainly determined by the degree of uniform corrosion and pitting corrosion.

(2) When the steel wire is in good condition, the fracture type is cup-conical fracture; in the case of uniform corrosion, the fracture originates in the center of the wire and then expands outward, with the fracture retaining a cup-conical shape; in pitting corrosion, the fracture originates from the corrosion hole on the surface of the steel wire.

(3) With the increase of the uniform corrosion depth and length, the ultimate strain of the steel wire decreases, but its strength and stiffness are not significantly reduced; with the increase of the depth and length of the pitting corrosion, the ultimate strain, strength, and stiffness of the steel wire are reduced to different degrees. The effect of uniform corrosion is more pronounced.

(4) The position and number of corrosion holes have a certain influence on the mechanical properties of the degraded steel wire: when the steel wire has one corrosion hole, the impact of pitting corrosion on the mechanical properties of the steel wire is relatively small; when there are two corrosion holes, the effect is centered, and the closer the two corrosion holes, the greater the impact; when there are three corrosion holes, the impact is the greatest.

Appendix

A

The line segment OA in the figure is parallel to BC, and the meanings of the symbols are as follows.

ε_e: ultimate elastic strain
ε_y: yield strain
ε_u: ultimate strain
ε_f: failure strain
F_y: yield bearing capacity of steel wire
F_u: ultimate bearing capacity of steel wire
E: elastic modulus of steel wire.

Data Availability

The experimental data used to support the findings of this study are included within the article.

Conflicts of Interest

The authors declare that there are no conflicts of interest regarding the publication of this paper.

References

[1] C. Liu, Y. Wang, X. Hu, Y. Han, X. Zhang, and L. Du, "Application of GA-BP neural network optimized by Grey Verhulst model around settlement prediction of foundation pit," *Geofluids*, vol. 2021, Article ID 5595277, 16 pages, 2021.

[2] A. Carpinteri and R. Brighenti, "Part-through cracks in round bars under cyclic combined axial and bending loading," *International Journal of Fatigue*, vol. 18, no. 1, pp. 33–39, 1996.

[3] P. Zhang, D. F. Zhang, Y. Yang et al., "A case study on intergrated modeling of spatial information of a complex geological body," *Lithosphere*, vol. 2022, no. s10, Article ID 2918401, 2022.

[4] L. Wang, X. Lu, L. Liu et al., "Influence of MgO on the hydration and shrinkage behavior of low heat Portland cement-based materials via pore structural and fractal analysis," *Fractal and Fractional*, vol. 6, no. 1, p. 40, 2022.

[5] L. Han, L. Wang, X. Ding, H. Wen, X. Yuan, and W. Zhang, "Similarity quantification of soil parametric data and sites using confidence ellipses," *Geoscience Frontiers*, vol. 13, no. 1, Article ID 101280, 2022.

[6] J. I. Xiao-Ming and L. Wei, "Review of research on instability failure mechanism and stability control of tunnel surrounding rock in water-bearing sandy ground," *Rock and Soil Mechanics*, vol. 30, 2009.

[7] Z. Liu, C. Y. Zhou, and M. Fang, "Failure criterion and deformation instability evaluation analysis of a tunnel by nonlinear dynamics," *Yantu Lixue/Rock and Soil Mechanics*, vol. 31, no. 12, pp. 3887–3893, 2010.

[8] L. Fang and D. Shao, "Application of long short-term memory (LSTM) on the prediction of rainfall-runoff in karst area," *Frontiers in Physics*, p. 685, 2022.

[9] B. Chen, W. Zhao, Y. Wang, and S. Xie, "Finite element analysis of cervical spine plate using double cage fusion," in *Proceedings of the 4th International Conference on Bioinformatics and Biomedical Engineering*, pp. 1–5, IEEE, Chengdu, China, July2010.

[10] J. P. Wang, Z. C Zhong, C. K Cheng et al., "Finite element analysis of the spondylolysis in lumbar spine," *Bio-Medical Materials and Engineering*, vol. 16, no. 5, pp. 301–308, 2006.

[11] J. Llorca and V. Sánchez-Gálvez, "Fatigue limit and fatigue life prediction in high strength cold drawn eutectoid steel wires," *Fatigue and Fracture of Engineering Materials and Structures*, vol. 12, no. 1, pp. 31–45, 1989.

[12] N. Couroneau and J. Royer, "Simplifying hypotheses for the fatigue growth analysis of surface cracks in round bars," *Computers & Structures*, vol. 77, no. 4, pp. 381–389, 2000.

[13] X. Zheng, X. Xie, and X. Li, "Experimental study and residual performance evaluation of corroded high-tensile steel wires," *Journal of Bridge Engineering*, vol. 22, no. 11, p. 04017091, 2017.

[14] Z. Dou, S. Tang, X. Zhang et al., "Influence of shear displacement on fluid flow and solute transport in a 3D rough fracture," *Lithosphere*, vol. 2021, 2021.

[15] D. Chen, H. Chen, W. Zhang, J. Lou, and B. Shan, "An analytical solution of equivalent elastic modulus considering confining stress and its variables sensitivity analysis for fractured rock masses," *Journal of Rock Mechanics and Geotechnical Engineering*, 2021.

[16] C. Cao, W. Zhang, J. Chen, B. Shan, S. Song, and J. Zhan, "Quantitative estimation of debris flow source materials by integrating multi-source data: a case study," *Engineering Geology*, vol. 291, Article ID 106222, 2021.

[17] G. Li, Y. Hu, S.-m. Tian, M. weibin, and H.-l. Huang, "Analysis of deformation control mechanism of prestressed anchor on jointed soft rock in large cross-section tunnel," *Bulletin of Engineering Geology and the Environment*, vol. 80, no. 12, pp. 9089–9103, 2021.

[18] C. Liu, L. Du, X. Zhang, Y. Wang, X. Hu, and Y. Han, "A new rock brittleness evaluation method based on the complete stress-strain curve," *Lithosphere*, vol. 2021, Article ID 4029886, 2021.

[19] J. Toribio, J. Matos, and B. González, "Micro-and macro-approach to the fatigue crack growth in progressively drawn pearlitic steels at different R-ratios," *International Journal of Fatigue*, vol. 31, no. 11-12, pp. 2014–2021, 2009.

[20] A. Carpinteri, R. Brighenti, and A. Spagnoli, "Part-through cracks in pipes under cyclic bending," *Nuclear Engineering and Design*, vol. 185, no. 1, pp. 1–10, 1998.

[21] J. Toribio and M. Toledano, "Fatigue and fracture performance of cold drawn wires for prestressed concrete," *Construction and Building Materials*, vol. 14, no. 1, pp. 47–53, 2000.

[22] B. Yuan, Z. Li, Z. Zhao, H. Ni, Z. Su, and Z. Li, "Experimental study of displacement field of layered soils surrounding laterally loaded pile based on transparent soil," *Journal of Soils and Sediments*, vol. 21, no. 9, pp. 3072–3083, 2021.

[23] B. Yuan, Z. Li, Y. Chen et al., "Mechanical and microstructural properties of recycling granite residual soil reinforced with glass fiber and liquid-modified polyvinyl alcohol polymer," *Chemosphere*, vol. 286, Article ID 131652, 2022.

[24] S. M. Elachachi, D. Breysse, S. Yotte, and C. Cremona, "A probabilistic multi-scale time dependent model for corroded structural suspension cables," *Probabilistic Engineering Mechanics*, vol. 21, no. 3, pp. 235–245, 2006.

[25] J. Xu, *Damage Evolution Mechanism and Remained Service Lives Evaluation of Stayed Cables*, Tongji University, Shanghai, China, 2006.

[26] J. Lemaitre and J.-L. Chaboche, *Mechanics of Solid Materials*, Cambridge University Press, Chennai, 1994.

[27] X. Li, Q. Li, Y. Hu et al., "Study on three-dimensional dynamic stability of open-pit high slope under blasting vibration," *Lithosphere*, vol. 2021, no. Special 4, p. 6426550, 2022.

[28] C. Zhu, M. Karakus, M. He et al., "Volumetric deformation and damage evolution of Tibet interbedded skarn under multistage constant-amplitude-cyclic loading," *International Journal of Rock Mechanics and Mining Sciences*, vol. 152, Article ID 105066, 2022.

[29] Y. Wang, H. Yang, J. Han, and C. Zhu, "Effect of rock bridge length on fracture and damage modelling in granite containing hole and fissures under cyclic uniaxial increasing-amplitude decreasing-frequency (CUIADF) loads," *International Journal of Fatigue*, vol. 158, Article ID 106741, 2022.

[30] Y.-q. Su, F.-q. Gong, S. Luo, and Z.-x. Liu, "Experimental study on energy storage and dissipation characteristics of granite under two-dimensional compression with constant confining pressure," *Journal of Central South University*, vol. 28, no. 3, pp. 848–865, 2021.

[31] Z.-j. Wu, Z.-y. Wang, L.-f. Fan, L. Weng, and Q.-s. Liu, "Micro-failure process and failure mechanism of brittle rock under uniaxial compression using continuous real-time wave velocity measurement," *Journal of Central South University*, vol. 28, no. 2, pp. 556–571, 2021.

[32] S. Maleki and S. Bagheri, "Behavior of channel shear connectors, Part II: analytical study," *Journal of Constructional Steel Research*, vol. 64, no. 12, pp. 1341–1348, 2008.

Hindawi
Advances in Materials Science and Engineering
Volume 2022, Article ID 2152814, 11 pages
https://doi.org/10.1155/2022/2152814

Research Article

Study on the Law of Rock Anelastic Recovery and the Characteristics of In Situ Stress Field of 2000 m Deep Stratum in Metal Mines of Coastal Area

Yuezheng Zhang,[1] **Hongguang Ji**,[1] **and Hanhua Xu**[2]

[1]*Beijing Key Laboratory of Urban Underground Space Engineering, University Of Science & Technology Beijing, Beijing 100083, China*
[2]*Kunming Prospecting Design Institute of China Nonferrous Metals Industry Co.Ltd, Kunming 650051, China*

Correspondence should be addressed to Yuezheng Zhang; yuezheng20053660@163.com

Received 3 March 2022; Accepted 15 March 2022; Published 12 April 2022

Academic Editor: Ren Fuqiang

Copyright © 2022 Yuezheng Zhang et al. This is an open access article distributed under the Creative Commons Attribution License, which permits unrestricted use, distribution, and reproduction in any medium, provided the original work is properly cited.

In situ stress field in deep strata is dominated by self-weight stress and tectonic stress, which is the dynamic source of a series of mining dynamic disasters such as rock burst, mine earthquake, and collapse. To develop deep resources and build deep engineering construction, the distribution characteristics of the in situ stress field must first be ascertained, so as to provide a basic basis for the engineering surrounding rock support design and disaster risk prevention and control. In this paper, taking the Sanshandao Gold Mine in the coastal area as the engineering background, in the early stage of the construction of the 2000 m deep shaft, the anelastic strain recovery method was used to measure the deep in situ stress field. The laws and characteristics of hysteretic elastic recovery of rock at different depths are obtained through experiments, and the effects of temperature, time, and other factors on strain recovery are revealed. The in situ stress test results are basically consistent with the traditional test methods. This method has low operational complexity and better application effect in deep formations. The research has accumulated test experience and basis for carrying out in situ stress measurement in the range of 2000 m and even deeper.

1. Introduction

In situ stress is the fundamental force causing deformation and failure of mining and other underground projects, and its level and direction have a great impact on the stability of roadway surrounding rock. In situ stress measurement is a necessary prerequisite for determining the mechanical properties of engineering rock mass, analyzing the stability of surrounding rock, and realizing the scientific excavation design of underground engineering [1–5]. In the deep mining of 2000 m, the geological conditions of resource occurrence are complex, the in situ stress increases, the ground temperature increases, and the degree of rock fracture and water pressure increase, which makes it more difficult to carry out in situ stress tests [6–9]. Under the action of high ground stress, the deeply buried rock mass shows different mechanical properties from the shallow rock mass. The rock shows stronger rheological properties and greater anelastic recovery deformation. Therefore, this feature of rock can be used to carry out the experiment of deep stress measurement by using the anelastic recovery method [10, 11].

It is used in combination with the drilling caving method and the hydraulic fracturing method to obtain more abundant in situ stress data [12]. Especially in the early stage of deep engineering construction, when the stress relief method and hydraulic fracturing method cannot be used, the ASR method can still obtain relatively reliable data and has wider applicability. Voight first proposed the anelastic strain recovery method (ASR method), which considers that the rock has creep (anelasticity), and the anelastic strain of the rock recovery is proportional to the stress state before the

isotropic rock strain recovery [13]. Blanton developed the theory of calculating the magnitude of horizontal principal stress, vertical stress, and Poisson's ratio using recovered anelastic strain, which is based on the belief that rock is linear viscoelastic, homogeneous, and isotropic [14]. Lin Weiren applied the anelastic strain recovery method to test the deep core, and the measurement results were in good agreement with the measurement results obtained by other methods [15]. After the 5.12 Wenchuan earthquake, this method was applied to the measurement of in situ stress in scientific boreholes for the first time in mainland China. The research results have a certain reference value for understanding the dynamic mechanism of the Wenchuan earthquake [16].

In order to study the engineering problems of the wellbore, roadway, large deformation of surrounding rock, and rockburst in Sanshandao Gold Mine in the depth range below −2000 m, the ASR method was used to carry out the measurement of the deep in situ stress field.

2. Principle of ASR Method (Constitutive Equation)

2.1. Arrangement of Strain Gauge. The anelastic strain recovery measurement of the measuring core shall ensure that the strain recovery value is not less than six independent directions. Two methods of strain rosette or strain gauge can be used, and the strain rosette method is used in this experiment. The core is taken out from the drilled hole, with the top of the specimen facing upwards, and the surface is ground after cleaning the core. The strain flowers were pasted on the surface of the core along the baselines at −45°, 0°, 45°, and 90°, respectively, as shown in Figure 1.

The direction of the long axis of the variable plate is called the axial direction. The experimental strain gauge has a total of 9 axes from a1 to a9. The relationship between the 9 axes and the coordinate axes is as follows: the axis a1 is parallel to the x-axis and perpendicular to the y and z axes; the axis a2 is parallel to the y axis and is parallel to the x and z axes. The axis is vertical; the axis a3 is parallel to the z-axis and perpendicular to the x and y axes; the axis a4 is oblique to the x and y axes by 45°; the axis a5 is oblique to the x and y axes by 45° and is perpendicular to the z-axis; the x and z axes are obliquely intersected by 45°; the axes a8 and a9 are obliquely intersected with the y and z axes by 45°, as shown in Figure 2.

2.2. Constitutive Equations. K. Matsuki proposed an ASR measurement method to determine three-dimensional in situ stress [17]. For isotropic viscoelastic materials, the local stress and pore water pressure are gradually released at $t = 0$, and the normal anelastic strain recovers in time from 0 to t, which is represented as follows:

$$\varepsilon_{\mathrm{a}}(\mathrm{t}) = \left(\frac{1}{3}\right)\left[\left(3l^2 - 1\right)\sigma_x + \left(3m^2 - 1\right)\sigma_y + \left(3n^2 - 1\right)\sigma_z + 6lm\tau_{\mathrm{xy}} + 6mn\tau_{\mathrm{yz}} + 6nl\tau_{\mathrm{zx}}\right]\mathrm{Jas}(t) + \left(\sigma_m - p_0\right)\mathrm{Jav}(t) + \alpha_T \Delta T(t). \tag{1}$$

where l, m, and n are direction cosines of the strain axis, corresponding to the x, y, and z axes; $\sigma_x, \sigma_y, \sigma_z$, τ_{xy}, τ_{yz}, and τ_{zx} are stress components; σ_m is the average normal stress; p_0 is the pore water pressure; α_T is the linear thermal expansion coefficient; $\Delta T(t)$ is the temperature change during measurement; and $\mathrm{Jas}(t)$ and $\mathrm{Jav}(t)$ are the ASR compliance in shear mode and volume mode, respectively.

The above equations provide the computational basis for the ASR measurement method. The anelastic strain depends on the in situ stress tensor component, pore water pressure, temperature changes in the core during the experiment, and anelastic strain recovery compliance in shear and bulk modes. Therefore, if the material constant ($\mathrm{Jas}(t)$, $\mathrm{Jav}(t)$, α_T) and pore water pressure are known, and the temperature is constant during the test, the three-dimensional in situ stress tensor can be obtained by measuring the anelastic strain in no less than six independent directions.

For an isotropic viscoelastic material, the three principal directions of the in situ stress are consistent with the three principal directions of the anelastic strain. Therefore, it is only necessary to determine the direction of the principal strain to obtain the direction of the principal stress.

The principal stress deviator is given by the following:

$$s_i = \sigma_i - \sigma_m (i = 1, 2, 3). \tag{2}$$

In the formula, s_i is the principal stress deviation (s_1, s_2, s_3); σ_i is the three principal stresses $(\sigma_1, \sigma_2, \sigma_3)$; and σ_m is the average principal stress, $\sigma_m = (\sigma_1 + \sigma_2 + \sigma_3)/3$.

The principal strain deflection is given by the following:

$$e_i = \varepsilon_i - e_m (i = 1, 2, 3). \tag{3}$$

In the formula, e_i is the principal strain deflection e_1, e_2, e_3; ε_i is the three principal strains $\varepsilon_1, \varepsilon_2, \varepsilon_3$; and e_m is the average principal strain, $e_m = (\varepsilon_1 + \varepsilon_2 + \varepsilon_3)/3$.

Through theoretical tests, it can be proved that the ratio of the deviated components of the principal stress is given by the ratio of the deviated components of the anelastic strain [18, 19]. If the rock material is isotropic, the ratio of the direction of the in situ principal stress to the principal stress deviator can be determined without knowing the anelastic strain recovery flexibility of the two modes.

2.3. Calculation of Principal Strain. The core coordinate system is set as o-xyz, and the z-axis is the same as the radial

direction of the core. Then, the relationship between the strain value measured by the rosette attached to the core surface and the strain tensor can be written as the following formula:

$$A\varepsilon = b. \tag{4}$$

In the formula, $\varepsilon = [\varepsilon_x, \varepsilon_y, \varepsilon_z, \varepsilon_{xy}, \varepsilon_{yz}, \varepsilon_{zx}]^T$ represents the strain tensor of the rock, $b = [b_1, b_2, b_3, b_4, b_5, b_6, b_7, b_8, b_9]^T$ is the strain value measured by the strain gauge pasted on the core surface, and $b_1, b_2, b_3, b_4, b_5, b_6, b_7, b_8, b_9$ corresponds to the axial strain acquisition values of a1–a9 in this measurement. A is the coefficient matrix, and the expansion formula (5) of A is as follows:

$$A = \begin{bmatrix} l_1^2 & m_1^2 & n_1^2 & 2l_1m_1 & 2m_1n_1 & 2n_1l_1 \\ l_2^2 & m_2^2 & n_2^2 & 2l_2m_2 & 2m_2n_2 & 2n_2l_2 \\ l_3^2 & m_3^2 & n_3^2 & 2l_3m_3 & 2m_3n_3 & 2n_3l_3 \\ l_4^2 & m_4^2 & n_4^2 & 2l_4m_4 & 2m_4n_4 & 2n_4l_4 \\ l_5^2 & m_5^2 & n_5^2 & 2l_5m_5 & 2m_5n_5 & 2n_5l_5 \\ l_6^2 & m_6^2 & n_6^2 & 2l_6m_6 & 2m_6n_6 & 2n_6l_6 \\ l_7^2 & m_7^2 & n_7^2 & 2l_7m_7 & 2m_7n_7 & 2n_7l_7 \\ l_8^2 & m_8^2 & n_8^2 & 2l_8m_8 & 2m_8n_8 & 2n_8l_8 \\ l_9^2 & m_9^2 & n_9^2 & 2l_9m_9 & 2m_9n_9 & 2n_9l_9 \end{bmatrix}. \tag{5}$$

l_i, m_i, n_i is the cosine of the axis a1–a9 relative to the coordinate system *o-xyz*. From the pasting method of the strain gauge, we can see that the cosine of each strain axis is shown in Table 1.

Substituting the data in the table into the expansion of A, the coefficient matrix A can be obtained as the following formula:

$$A = \begin{bmatrix} 1 & 0 & 0 & 0 & 0 & 0 \\ 0 & 1 & 0 & 0 & 0 & 0 \\ 0 & 0 & 1 & 0 & 0 & 0 \\ 0.5 & 0.5 & 0 & 1 & 0 & 0 \\ 0.5 & 0.5 & 0 & -1 & 0 & 0 \\ 0.5 & 0 & 0.5 & 0 & 0 & -1 \\ 0.5 & 0 & 0.5 & 0 & 0 & 1 \\ 0 & 0.5 & 0.5 & 0 & -1 & 0 \\ 0 & 0.5 & 0.5 & 0 & 1 & 0 \end{bmatrix}. \tag{6}$$

The number of unknowns in the strain component (1) is $n = 6$, and the number of independent equations is $m = 9$. The most accurate solution can be obtained by using the least-squares method to solve the above overdetermined equations. The least-squares method is used to solve the following equation (7), and the solution process is as follows:

$$A^T A\varepsilon = A^T b. \tag{7}$$

The solved equation is as follows:

$$\varepsilon = \left(A^T A\right)^{-1} A^T b. \tag{8}$$

The strain component ε can be solved from this, and it can be represented by three principal strains, and the magnitude of the principal strain can be obtained by solving the following equation:

$$\begin{bmatrix} \varepsilon_x - \lambda & \varepsilon_{xy} & \varepsilon_{xz} \\ \varepsilon_{yx} & \varepsilon_y - \lambda & \varepsilon_{yz} \\ \varepsilon_{zx} & \varepsilon_{zy} & \varepsilon_z - \lambda \end{bmatrix} \begin{Bmatrix} l \\ m \\ n \end{Bmatrix} = 0. \tag{9}$$

To solve the above system of linear homogeneous equations, the determinant coefficient can be 0 to solve. The specific solution process is as follows:

$$\begin{vmatrix} \varepsilon_x - \lambda & \varepsilon_{xy} & \varepsilon_{xz} \\ \varepsilon_{yx} & \varepsilon_y - \lambda & \varepsilon_{yz} \\ \varepsilon_{zx} & \varepsilon_{zy} & \varepsilon_z - \lambda \end{vmatrix} = 0. \tag{10}$$

The determinant is expanded to a cubic equation in one variable:

$$\varepsilon^3 - (\varepsilon_1 + \varepsilon_2 + \varepsilon_3)\varepsilon^2 + (\varepsilon_2\varepsilon_3 + \varepsilon_3\varepsilon_1 + \varepsilon_1\varepsilon_2)\varepsilon - \varepsilon_1\varepsilon_2\varepsilon_3 = 0, \tag{11}$$

where $\varepsilon_1 + \varepsilon_2 + \varepsilon_3 = \varepsilon_x + \varepsilon_y + \varepsilon_z$, $\varepsilon_2\varepsilon_3 + \varepsilon_3\varepsilon_1 + \varepsilon_1\varepsilon_2 = \varepsilon_y\varepsilon_z + \varepsilon_z\varepsilon_x + \varepsilon_x\varepsilon_y - \varepsilon_{yz}^2 - \varepsilon_{zx}^2 - \varepsilon_{xy}^2$, $\varepsilon_1\varepsilon_2\varepsilon_3 = \varepsilon_x\varepsilon_y\varepsilon_z - \varepsilon_x\varepsilon_{yz}^2 - \varepsilon_y\varepsilon_{zx}^2 - \varepsilon_z\varepsilon_{xy}^2 + 2\varepsilon_{yz}\varepsilon_{zx}\varepsilon_{xy}$.

The result of solving the above one-dimensional cubic equation is the three principal strain values.

It can be seen that the solution process of the above equations is actually to find the eigenvalues and eigenvectors of the matrix. The eigenvalues of the matrix are the principal strains, and the eigenvectors are the direction cosines of the principal strains. Therefore, knowing the geographic direction of the principal strain will know the geographic direction of the principal stress [20, 21].

2.4. Calculation of Principal Stress. The magnitude of the principal stress $\sigma_i\,(i = 1, 2, 3)$ calculated by the anelastic strain recovery method can be obtained from the following:

$$\sigma_i = \frac{e_i(t)}{\mathrm{Jas}(t)} + \frac{\{e_m(t) - \alpha_T \Delta T(t)\}}{\mathrm{Jav}(t)} + p_0. \tag{12}$$

In the experiment, the constant temperature water tank ensures that the temperature change is 0, so as long as $\mathrm{Jas}(t)$, $\mathrm{Jav}(t)$, and the in situ principal stress can be obtained according to the deviatoric strain and pore water pressure. Then, the vertical stress can be expressed by the following formula:

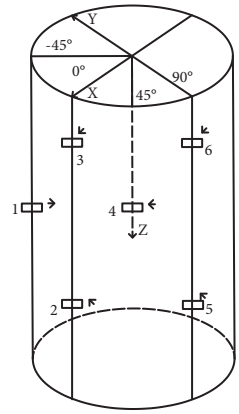

Figure 1: Schematic diagram of the arrangement of strain gauges on the core surface.

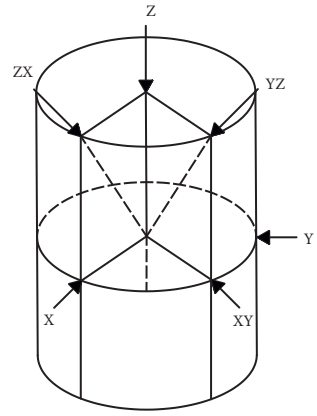

Figure 2: Corresponding axial positions of the strain gauges.

$$\sigma_v = \frac{\left\{\left(\left[l_p^2 e_1(t) + m_p^2 e_2(t) + n_p^2 e_3(t)\right] / (\mathrm{Jas}(t)/\mathrm{Jav}(t))\right) + e_m(t)\right\}}{\mathrm{Jav}(t)} + p_0, \tag{13}$$

where l_p, m_p, n_p is the cosine of the direction between the vertical stress and the three principal strain axes.

$\mathrm{Jas}(t), \mathrm{Jav}(t)$ is the anelastic strain recovery flexibility under the two modes, which can generally be obtained from experiments. Some literature approximates the ratio of the two [22, 23]. At the same time, the vertical principal stress is equal to the gravity of the overburden:

$$\sigma_v = \rho g h. \tag{14}$$

Therefore, it can be obtained from the previous article, and (12)–(14) can be combined to complete the stress solution, thereby obtaining the values of the maximum principal stress, the intermediate principal stress, and the minimum principal stress.

3. Field Experiment of ASR Method

3.1. Engineering Background. The Sanshandao Gold Mine is located in Laizhou City, Shandong Province. From the perspective of regional structural conditions, it is located on the east side of the Yimu fault zone. The geology of the mining area is controlled by the regional EW tectonic system and the NNE trending Neocathaysian tectonic system. In order to meet the development and utilization of deep mineral resources in the Sanshandao Gold Mine, a shaft with a diameter of 10 m and a depth of −2000 m is proposed to be built in the Xiling mining area as an auxiliary shaft in the mining area. During the preliminary engineering survey, the drilling depth of the exploration hole is −2017 m. The lithology of the deep strata is mainly granite. Figure 3 shows the core exposure of the deep part of the formation.

After years of mining, the research experience in the Sanshandao Gold Mine shows that the deep formation is in a state of high stress and strong compression, and the rock has high hardness and high energy content. In construction disturbances, it is easy to produce strong rock dynamic disasters, which brings challenges to excavation support. Under the influence of high stress, the wall of the deep shaft and the structural material of the chamber will be deformed and damaged. As the depth increases, the in situ stress increases linearly. When reaching a certain depth, the entire deep formation rock mass is in a state of strong compressive

Table 1: Cosine values of each strain axis.

Strain axial	Direction cosine		
	l_i	m_i	n_i
a_1	1	0	0
a_2	0	1	0
a_3	0	0	1
a_4	0.7071	0.7071	0
a_5	0.7071	−0.7071	0
a_6	−0.7071	0	0.7071
a_7	0.7071	0	0.7071
a_8	0	0.7071	−0.7071
a_9	0	0.7071	0.7071

Figure 3: Core exposure of some strata (−1815.56~−1820.16 m, −1897.46~−1902.06 m).

stress due to the constraint of the surrounding rock. Once the external conditions change, the stress inside the rock mass will crush the rock, and the energy will be released rapidly, causing damage to the deep well engineering [24–26].

For this shaft engineering area, the current in situ stress test depth is about −1000 m, and the main method used is the division method that can be applied in well extension engineering. The stress status of deeper formations is still unclear, and it is urgent to carry out in situ stress tests at a depth of −2000 m for various engineering risks that may occur in well construction projects [27, 28]. Since there is no well-extension project such as roadway at this depth, the stress relief method cannot be tested, so the hydraulic fracturing method and ASR method are mainly used for testing. This paper mainly introduces the sampling test work of the ASR method in the range of −1180 m ~ −1960 m; the magnitude of the in situ stress can be obtained, and the determination of the initial direction of the core is generally obtained by the paleomagnetic method, which requires special indoor conditions and instruments to be completed. Limited by the field test conditions, the in situ stress in the deep formation is mainly measured by the ASR method, and the in situ stress field direction is obtained by the hydraulic fracturing method, which will not be introduced in this paper.

3.2. Experimental Device. ASR measurement equipment mainly includes deformation monitoring system, constant temperature system, information acquisition, and processing system. By measuring the anelastic microstrain recovery of the in situ oriented core in the deep formation, and using the acoustic monitoring system to monitor the core acoustic emission (energy) and wave velocity field evolution, the three principal stresses of the stratum where the core is located can be calculated, which provides a basis for studying the creep mechanism of rock unloading under high in situ stress.

Deformation monitoring system is used to measure the multidirectional deformation of rock samples. The Donghua test DH3816N static stress-strain test and analysis system combined with the supporting software DHDAS dynamic signal acquisition and analysis system was used to monitor the strain of the core specimen.

Constant temperature water bath system is used to provide a constant temperature test environment for rock samples. The constant temperature system is an important factor to ensure the accurate results of ASR in situ stress measurement. In this experiment, the TYC-DZ type anelastic strain recovery method three-dimensional in situ stress test system-high-precision water bath incubator is used. The temperature change range of the constant temperature water bath is within ±0.1°. The instrument is shown in Figure 4.

3.3. Experimental Process. The core used in this anelastic strain recovery method in situ stress test was taken from the auxiliary shaft exploration borehole in the Xiling mining area of the Sanshandao Gold Mine. On-site sampling needs to be taken back to the laboratory immediately after the XY-

Figure 4: High-precision water bath constant temperature system.

8 drilling rig salvages the core, and the core sample is measured immediately after the core sample is lifted from the borehole. The selection of core samples generally needs to meet the following conditions: ① the core texture is uniform and there is no original crack; ② the length of the core sample is 15–20 cm, the surface is complete, and the strain gauge can be attached; ③ the deeper the core is collected, the more accurate the calculation is. Because more stress is released and the strain recovery is larger, it is easier to calculate the in situ stress state; ④ try to stay away from the fault zone in the formation.

After past the gauge, as shown in Figure 5(a), the strain gauge is connected to the DHDAS dynamic signal strain acquisition instrument (using terminal blocks) to check whether the channel is balanced. After the inspection is correct, the core is wrapped (guaranteed to be sealed) and placed in a constant temperature water tank for testing; at the same time, the temperature of the water tank must be consistent with the in situ temperature environment of the rock sample during the test. At the same time, a core of the same lithology is used as a compensation sample to connect to the compensation channel of the strain acquisition instrument to exclude the influence of system displacement and thermal expansion of the rock. During the test, the long-term stability of the core and the equipment and the constant temperature should be ensured for about 7 days. The ASR experimental acquisition system is shown in Figure 5(b).

4. Data Analysis and Discussion

4.1. Calculation and Analysis of Measured Data. The core sample is granite with a diameter of φ60 and a length of 150~200 mm. The measurement duration for each core sample is 6–7 days. In total, anelastic strain recovery tests of five samples in the depth range of −1180 m to −2008 m were completed. The anelastic strain recovery curves are shown in Figures 6–9; in order to facilitate comparison, −1180 m rock samples are tested at room temperature, other rock samples are placed in the water bath incubator, and the data with small error and good continuity in 9 directions are selected for analysis. It can be seen from the recovery curve that the anelastic strain of each strain gauge is a tensile change, indicating that the rock sample is under compression in the in situ state. With the increase of measurement time, the strain recovery occurred in all 9 strain axes of the test core, and gradually became flat and became stable on the 5th to 7th day.

Temperature changes have a significant effect on rock hysteretic recovery. At the beginning of the experiment, core samples at a depth of -1180 m were tested at room temperature. As shown in Figure 6, with the passage of time, the overall trend of the hysteretic recovery strain curve is upward. Except the a1 strain curve, which reaches 900 microstrains, the maximum values of other strain curves are in the range of 300–550 microstrains. However, with the periodic increase and decrease of temperature between day and night, the strain curve will also change periodically, and a temperature difference between day and night can cause 150 microstrain errors. Therefore, the ASR method needs to be guaranteed under constant temperature conditions.

The four core samples in Figures 7–10 were tested under constant temperature conditions. The strain curve is relatively smooth. The temperature adjustment of the incubator has a slight but negligible effect on the curve. During the testing process of the −2008 m core sample, the a5, a7, and a8 strain gauges fell off and only the strain recovery in 6 directions was recorded, which could meet the calculation requirements.

Table 2 shows the final anelastic strain recovery measurements for the 4 specimens. The value of each strain component is in the range of 300 to 1500 microstrains, which can meet the requirements of the measurement.

After obtaining the anelastic strain values through actual measurement, firstly 6 strain values are obtained by solving the aforementioned equations (8) and (11) and then the eigenvalues and eigenvectors of the strain matrix are found, which are the directional cosines corresponding to the 3 principal strains and principal strains.

The principal stress values are solved by (12)–(14). Among them, the ratio of shear mode anelastic recovery flexibility to volume mode anelastic recovery flexibility is set as 2, and the average density of the overlying rock layer is 2.7 g/cm^3. Then, the vertical principal stress can be calculated by (14), and finally, the maximum principal stress value

(a) (b)

Figure 5: (a) Layout of core strain gauges in an actual test; (b) signal acquisition of ASR in situ stress measurement experiment.

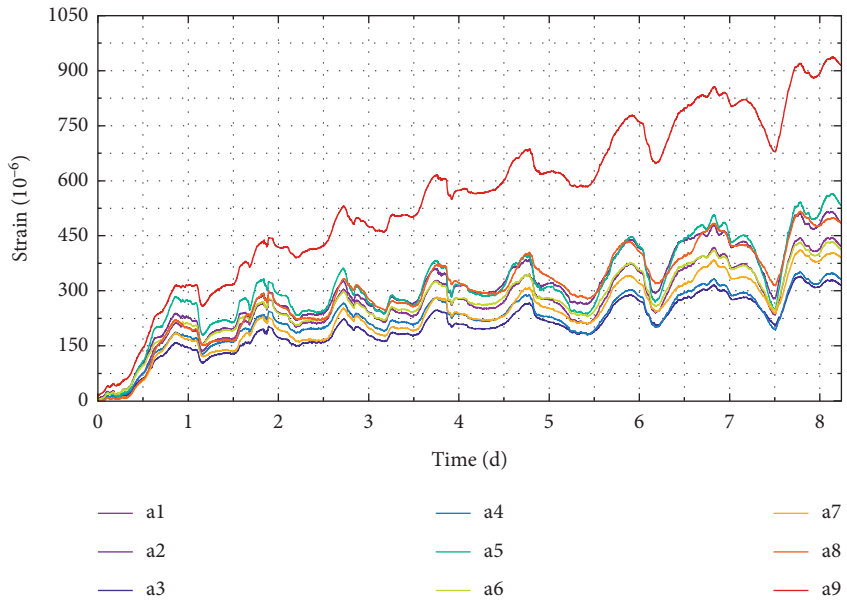

Figure 6: –1180 m core sample anelastic recovery strain curve.

and the minimum principal stress value of the corresponding depth are obtained, as shown in Table 3.

In order to verify the validity of the experimental results of the ASR method, as a reference object for comparison, this paper also gives the distribution law of the in situ stress test results obtained by the hydraulic fracturing method [29], as shown in equation (15). The maximum and minimum principal stress values corresponding to the experimental depth of the ASR method were calculated, respectively, as shown in Table 3.

$$\begin{aligned} \sigma_{\max} &= 0.030\mathrm{D} + 10.142 \\ \sigma_{\min} &= 0.019\mathrm{D} + 7.986 \\ \sigma_v &= 0.027\mathrm{D} - 0.019. \end{aligned} \tag{15}$$

Among them, D is the absolute value of drilling depth, and the unit is m; the unit of principal stress $\sigma_{\max}, \sigma_{\min}, \sigma_v$ is MPa.

Compared with the test results obtained by the hydraulic fracturing method, the results obtained by the ASR method are basically the same, and the absolute value of the error is in the range of 0.4–10.4%. Time is the most important factor affecting the test results. The time for core strain recovery to be basically completed is generally 3–5 days. With the increase of depth, the recovery time increases slightly without much change. However, after the core is separated from the in situ formation at the bottom of the hole, the elastic strain will recover rapidly in a short time, and at the same time, the anelastic strain will also begin to recover. In the drilling exploration, the core is taken out by rope coring, which takes

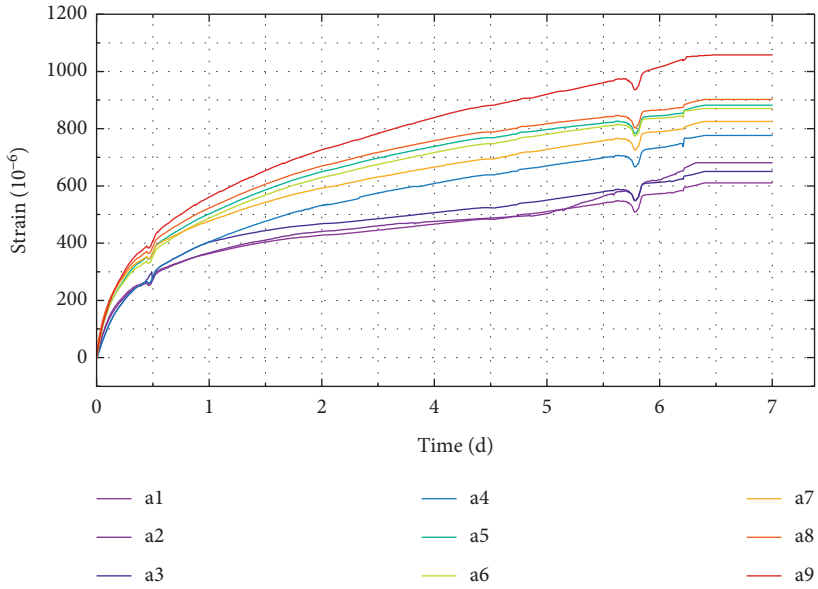

Figure 7: −1816 m core sample anelastic recovery strain curve.

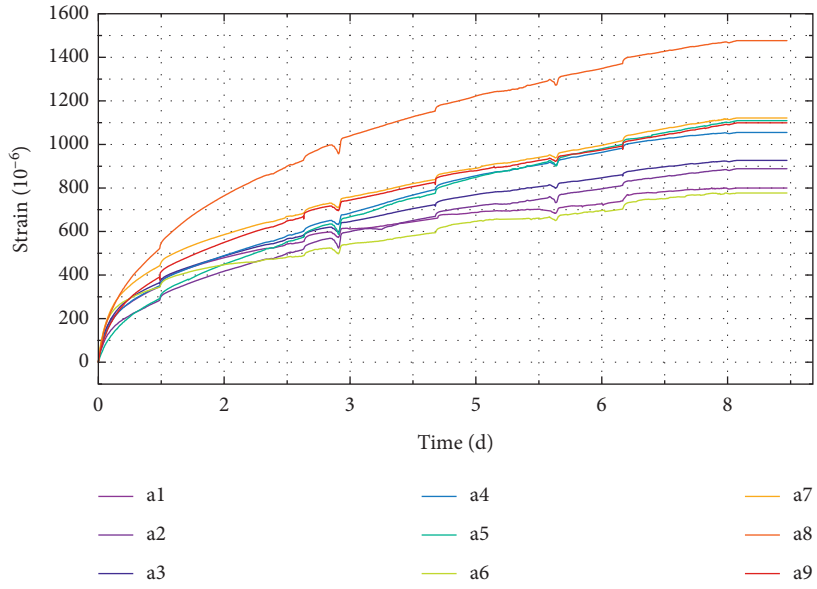

Figure 8: −1879 m core sample anelastic recovery strain curve.

about 1 hour. After that, the experimental preparation process such as pasting the strain gauges also takes about 1 hour, so the experimental measurement actually lags behind for a period of time. However, the rate of anelastic strain recovery during this period is still relatively large, resulting in the loss of some initial recovery amount, causing the anelastic strain recovery amount used in our calculation to be smaller than the actual strain amount, and the obtained stress results will also be smaller than the actual amount. To overcome the influence of time factors, it is necessary to ensure that the experiment can be carried out quickly after the core leaves the original position, so as to eliminate the error caused by the time factor as much as possible.

4.2. Discussion. The amount of anelastic strain recovery of cores at different depths is different. From the core strain recovery curves at different depths, we can see that the strain recovery is proportional to the depth, which also shows that the deep in situ stress is greater than the shallow in situ stress. Compared with the shallow part, the anelastic recovery value of the deep core is larger. In literature [18, 19], the ASR test depth is −746 m ~ −1173 m, and the maximum anelastic strain of the core reaches 600~1000 microstrains. In this experiment, the strain values measured in the −1180 m core sample ranged from 300 to 900 microstrains. However, the anelastic strain of the core at the depth of −2008 m obtained in this paper reaches 1600 microstrains, which

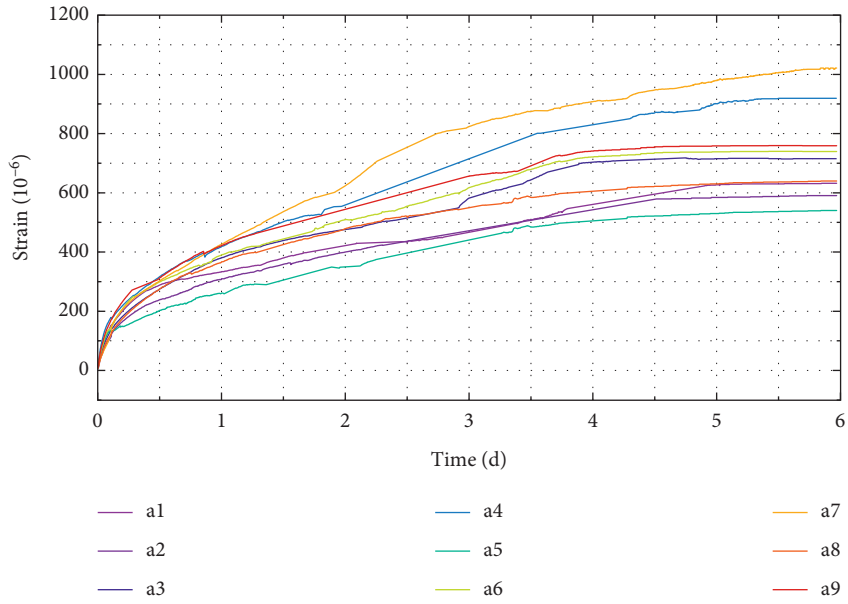

Figure 9: –1960 m core sample anelastic recovery deformation curve.

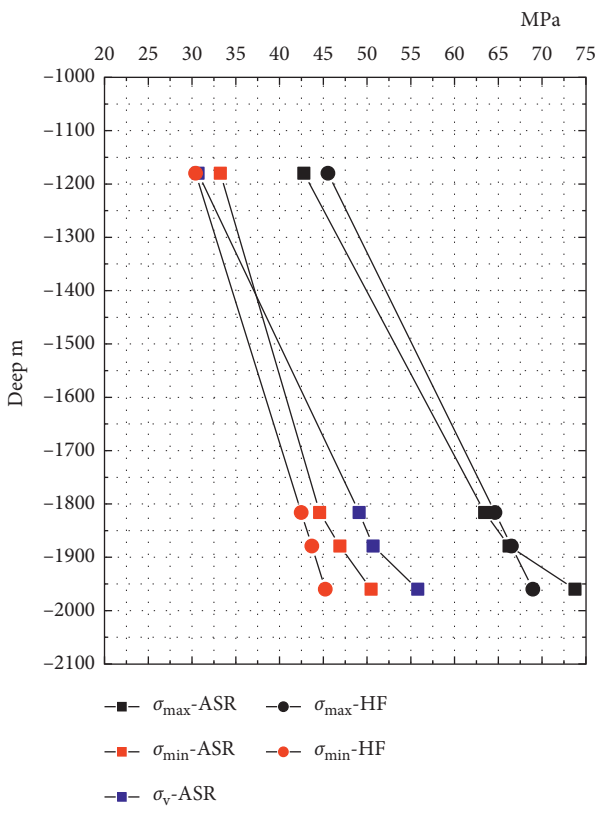

Figure 10: Comparison of test results of ASR and hydraulic fracturing.

shows that with the increase of depth, the anelastic strain recovery of the core is larger. Of course, this difference may also be caused by different lithology, and the anelastic characteristics of different mineral compositions are different. And the larger the anelastic strain recovery is, the smaller the measurement error is, and the influence on the results is relatively small. Therefore, the ASR method is more suitable for deep hole cores.

The hydraulic fracturing method has many unique characteristics in testing stress in shallow holes and has been widely used in rock engineering, oil drilling, and seismic research. There are few hydraulic fracturing tests in the literature with a depth of more than 1000 m, and most of them are concentrated in shallow formations [30, 31]. During deep hole testing, the research team found that hydraulic fracturing is affected by many factors. Deep boreholes often appear necking, collapsed, and setback, causing the test instrument to get stuck or fall off. The increase in the number of test reciprocations also causes damage to the hole wall, which ultimately results in a significant increase in the hydraulic fracturing test cycle and an increase in economic costs. In contrast, the ASR method can be performed simultaneously during the drilling process and has the advantages of simple operation, short construction period, and low cost [32, 33].

In this paper, the exploration and application of the ASR method in deep hole drilling is carried out. Under the conditions of deep well extension engineering (such as roadways and chambers with a depth of –1500 m), the test can be carried out simultaneously with the stress relief method. In addition to the paleomagnetic method, the initial orientation of the core sample can also use the borehole wall imaging technology. In the next step, when the ASR method experiment is carried out in the deep hole, the ultrasonic borehole imaging technology can be used to determine the core orientation, so as to obtain the principal stress direction. The drilling depth required by the stress relief method is shallow, generally in the range of 8 m to 12 m. Due to the short coring time, while making full use of the stress relief method to drill the core, the core orientation can also be determined by drilling TV and other techniques in this

Table 2: Strain recovery of different strain axes in deep core.

Strain axis (m)	a_1	a_2	a_3	a_4	a_5	a_6	a_7	a_8	a_9
−1180	443	513	328	347	563	432	402	497	935
−1816	611	681	651	776	882	871	825	902	1058
−1879	800	888	927	1055	1109	777	1121	1476	1099
−1960	632	590	715	919	539	739	1021	639	759

Table 3: In situ stress measurement results by ASR method and hydraulic fracturing method.

Depth (m)	ASR			Hydraulic fracturing	
	σ_{max} (MPa)	σ_{min} (MPa)	σ_v (MPa)	σ_{max} (MPa)	σ_{min} (MPa)
−1180	42.78	33.24	30.7	45.54	30.41
−1816	63.45	44.58	49.1	64.62	42.49
−1879	66.24	46.91	50.7	66.51	43.69
−1960	73.76	50.46	55.8	68.94	45.23

depth range. Therefore, the accuracy and difference of the above two methods are compared within the same surrounding rock area, and the engineering experience and scientific research data foundation are further accumulated for the improvement of the ASR method [34–36].

5. Conclusion

(1) Taking the −2000 m deep shaft of the Sanshandao Gold Mine as the engineering background, the ASR method was used to measure the deep in situ stress. The maximum principal stress values σ_{max} of −1180 m, −1816 m, −1879 m, and −1960 m are 42.78~73.76 MPa, and the minimum principal stress values σ_{min} are 33.24~50.46 MPa, respectively, which provide important basic data for shaft engineering construction, surrounding rock stability, wellbore, and roadway support design.

(2) Comparing the in situ stress measurement results of the ASR method with the hydraulic fracturing method, the two are basically consistent, and the absolute error is in the range of 0.4~10.4%. This proves the reliability of in situ stress measurement by ASR method, which can reduce the error and further improve the accuracy of ASR method by controlling the influence of time.

(3) The ASR method is more suitable for in situ stress measurement of deep rock formations with good integrity. The in situ stress level increases with depth. At the same time, the measurement error decreases with the increase of elastic strain recovery, which makes the applicability of the ASR method better.

(4) Disadvantages such as hole collapse and shrinkage can be avoided using the ASR method. It can be carried out simultaneously with the engineering exploration and drilling process in the early stage of engineering construction. The ASR method is easy to operate, does not affect the construction period, and has significant advantages in the measurement of deep in situ stress.

Data Availability

The data used to support the findings of this study are available from the corresponding author upon request.

Conflicts of Interest

The authors declare that they have no conflicts of interest.

Acknowledgments

This work was supported by the National Key Research and Development Program of China under Grant no. 2017YFC1503100 and the Major Scientific and Technological Innovation Projects in Shandong Province under Grant no. 2019SDZY02.

References

[1] C. Zhu, M. C. He, X. H. Zhang, Z. G. Tao, Q. Yin, and L. F. Li, "Nonlinear mechanical model of constant resistance and large deformation bolt and influence parameters analysis of constant resistance behavior," *Rock and Soil Mechanics*, vol. 42, no. 07, pp. 1911–1924, 2021.

[2] H. P. Kang, J. Lin, and X. Zhang, "Research and application of in-situ stress measurement in deep mines," *Chinese Journal of Rock Mechanics and Engineering*, vol. 26, no. 05, pp. 929–933, 2007.

[3] H. P. Xie, F. Gao, and Y. Ju, "Research review of the state key research development program of China: deep rock mechanics and mining theory," *Chinese Journal of Rock Mechanics and Engineering*, vol. 34, no. 11, pp. 2161–2178, 2015.

[4] M. Gao, J. Xie, Y. Gao et al., "Mechanical behavior of coal under different mining rates: a case study from laboratory experiments to field testing," *International Journal of Mining Science and Technology*, vol. 31, no. 5, pp. 825–841, 2021.

[5] H. Peng, X. M. Ma, J. J Jiang, and L. G. Peng, "Research on stress field and hydraulic fracturing in-situ stress measurement of 1000 m deep hole in Zhaolou coal mine," *Chinese Journal of Rock Mechanics and Engineering*, vol. 30, no. 08, pp. 1638–1645, 2011.

[6] L. Qiao, Y. M. Zhang, Y. Li, and S. Fu, "A non-linear elastic model and high-level biaxial loading and unloading test for CSIRO in-situ stress measurement in deep granite," *Chinese Journal of Rock Mechanics and Engineering*, vol. 38, no. 01, pp. 40–48, 2019.

[7] C. Cao, W. Zhang, J. Chen, B. Shan, S. Song, and J. Zhan, "Quantitative estimation of debris flow source materials by integrating multi-source data: a case study," *Engineering Geology*, vol. 291, Article ID 106222, 2021.

[8] M. F. Cai, "Studies of temperature compensation techniques in rock stress measurements," *Chinese Journal of Rock Mechanics and Engineering*, vol. 10, no. 03, pp. 227–235, 1991.

[9] M. F. Cai, W. D. Liu, and Y. Li, "In-situ stress measurement at deep position of Linglong gold mine and distribution law of in-situ stress field in mine area," *Chinese Journal of Rock Mechanics and Engineering*, vol. 29, no. 09, pp. 227–233, 2010.

[10] M. Z. Gao, H. C. Hao, S. N. Xue et al., "Discing behavior and mechanism of cores extracted from Songke-2 well at depths below 4,500 m," *International Journal of Rock Mechanics and Mining Sciences*, vol. 149, Article ID 104976, 2022.

[11] M. F. Cai, C. Z. Chen, H. Peng, H. G. Ji, L. Qiao, and Z. Y. Tan, "In-situ stress measurement by hydraulic fracturing technique in deep position of Wanfu coal mine," *Chinese Journal of Rock Mechanics and Engineering*, vol. 25, no. 05, pp. 1069–1074, 2006.

[12] L. J. Wang, D. S. Sun, and W. R. Lin, "Anelastic strain recovery method to determine in-situ stress and application example," *Chinese Journal of Geophysics*, vol. 55, no. 05, pp. 1674–1681, 2012.

[13] B. Voight, "Determination of the virgin state of stress in the vicinity of a borehole from measurements of a partial anelastic strain tensor in drill cores," *Felsmechanik und Ingenieurgeologie*, vol. 6, no. 04, pp. 201–215, 1968.

[14] T. L. Blanton, "The Relation between Recovery Deformation and In-Situ Stress Magnitudes," *Proceedings of the Spe/doe Low Permeability Gas Reservoirs Symposium*, Denver, Colorado, March 1983.

[15] W. R. Lin, E. C. Yeh, H. Ito et al., "Preliminary results of stress measurement using drill cores of TCDP hole-a: an application of anelastic strain recovery method to three-dimensional in-situ stress determination," *Terrestrial, Atmospheric and Oceanic Sciences*, vol. 18, no. 02, pp. 379–393, 2007.

[16] D. S. Sun, W. R. Lin, J. W. Cui et al., "Three-dimensional in situ stress determination by anelastic strain recovery and its application at the Wenchuan Earthquake Fault Scientific Drilling Hole-1 (WFSD-1)," *Science China Earth Sciences*, vol. 44, no. 03, pp. 510–518, 2014.

[17] K. Matsuki, "Three-dimensional in-situ stress measurement with anelastic strain recovery of a rock core," *Proc 7th ISRM International Congress on Rock Mechanics, Aachen*, vol. 1, pp. 557–560, 1991.

[18] L. J. Wang, J. W. Cui, and D. S. Sun, "Determination of three-dimensional in situ stresses by anelastic strain recovery in Tengchung scientific drilling hole," *Acta Geoscientia Sinica*, vol. 37, no. 01, pp. 111–115, 2016.

[19] W. R. Lin, "A core-based method to determine three-dimensional in-situ stress in deep drilling wells : anelastic strain recovery technique," *Chinese Journal of Rock Mechanics and Engineering*, vol. 27, no. 12, pp. 2387–2394, 2008.

[20] W. C. Sun, H. Min, and C. Y. Wang, "Three-dimensional geostress measurement and geomechanical analysis," *Chinese Journal of Rock Mechanics and Engineering*, vol. 27, no. S2, pp. 3778–3784, 2008.

[21] X. M. Ma, H. Peng, J. P. Bai, Z. Li, and J. J. Jiang, "Review on the research progress of the compliance of rocks in in-situ stress measurement methods of anelastic strain recovery (ASR)," *Journal of Geomechanics*, vol. 23, no. 04, pp. 526–530, 2017.

[22] T. X. Chen, *Research on In-Situ Stress Measurement and Application Based on Inelastic Strain Recovery*, Yanshan University, Hebei, China, 2020.

[23] D. S. Sun, H. T. Lv, L. J. Wang et al., "Determination of the in-situ stress state at 7 km depth under Tarim Basin by ASR and DITH methods," *Chinese Journal of Rock Mechanics and Engineering*, vol. 37, no. 02, pp. 383–391, 2018.

[24] C. Zhu, M.-C. He, B. Jiang, X.-Z. Qin, Q. Yin, and Y. Zhou, "Numerical investigation on the fatigue failure characteristics of water-bearing sandstone under cyclic loading," *Journal of Mountain Science*, vol. 18, no. 12, pp. 3348–3365, 2021.

[25] G. Li, Y. Hu, S.-M. Tian, M. weibin, and H.-L. Huang, "Analysis of deformation control mechanism of prestressed anchor on jointed soft rock in large cross-section tunnel," *Bulletin of Engineering Geology and the Environment*, vol. 80, no. 12, pp. 9089–9103, 2021.

[26] D. H. Chen, H. E. Chen, W. Zhang, J. Q. Lou, and B. Shan, "An analytical solution of equivalent elastic modulus considering confining stress and its variables sensitivity analysis for fractured rock masses," *Journal of Rock Mechanics and Geotechnical Engineering*, 2021.

[27] M. F. Cai, D. Ji, and Q. F. Guo, "Study of rockburst prediction based on in-situ stress measurement and theory of energy accumulation caused by mining disturbance," *Chinese Journal of Rock Mechanics and Engineering*, vol. 32, no. 10, pp. 1973–1980, 2013.

[28] F. Chen, C. He, and J. H. Deng, "Concept of high geostress and its qualitative and quantitative Definitions," *Rock and Soil Mechanics*, vol. 36, no. 04, pp. 971–980, 2015.

[29] K. K. Hou, Q. Z. Wu, F. P. Zhang, C. Peng, H. X. Liu, and X. Q. Liu, "Application of different in-situ stress testing methods in 2005 meters shaft-building area of Sanshandao gold mine and the distribution law of in-situ stress," *Rock and Soil Mechanics*, vol. 43, no. 04, pp. 1–10, 2022.

[30] H. P. Kang, B. D. Yin, F. Q. Gao, and H. W. Lv, "Database and characteristics of underground in-situ stress distribution in Chinese coal mines," *Journal of China Coal Society*, vol. 44, no. 01, pp. 23–33, 2019.

[31] H. J. Wang, L. Tang, X. H. Ren, L. W. Zhong, F. A. Si, and H. Ariel, "Rock deformation memory effect: applications, experiments and theories," *Chinese Journal of Geotechnical Engineering*, vol. 40, no. 09, pp. 1571–1583, 2018.

[32] T.-b. Zhao, M.-l. Xing, W.-y. Guo, C.-w. Wang, and B. Wang, "Anchoring effect and energy-absorbing support mechanism of large deformation bolt," *Journal of Central South University*, vol. 28, no. 2, pp. 572–581, 2021.

[33] Z. Dou, S. Tang, X. Zhang et al., "Influence of shear displacement on fluid flow and solute transport in a 3D rough fracture," *Lithosphere*, vol. 2021, no. 4, Article ID 1569736, 2021.

[34] D. Y. Xi, C. G. Zhou, S. L. Xu, and Y. Du, "Research of viscoelasticity attenuation mechanism of saturated sandstones," *Chinese Journal of Geophysics*, vol. 55, no. 07, pp. 2362–2370, 2012.

[35] D. A. Zhao, Z. M. Chen, and X. L. Cai, "Analysis of distribution rule of geostress in China," *Chinese Journal of Rock Mechanics and Engineering*, vol. 26, no. 06, pp. 1265–1271, 2007.

[36] T. Chen, "Engineering application of ultradeep horizontal (directional) borehole testing in Sichuan-Tibet Railway," *Chinese Journal of Engineering Geophysics*, vol. 18, no. 05, pp. 694–702, 2021.

Hindawi
Advances in Materials Science and Engineering
Volume 2022, Article ID 9144673, 9 pages
https://doi.org/10.1155/2022/9144673

Research Article

Strength Characteristics and Failure Mechanism of Granite with Cross Cracks at Different Angles Based on DIC Method

Xu Wu,[1] **Liyuan Zhang**,[2] **Jinglai Sun**,[1] **Qifeng Guo**,[3] **Jiliang Pan**,[3] **and Jun Gao**[1]

[1]*Beijing Municipal Engineering Research Institute, Beijing 100037, China*
[2]*CNBM Geological Engineering Exploration Academy Co. Ltd, Beijing 100102, China*
[3]*School of Civil and Resource Engineering, University of Science and Technology Beijing, Beijing 100083, China*

Correspondence should be addressed to Qifeng Guo; guoqifeng@ustb.edu.cn

Received 2 January 2022; Revised 12 February 2022; Accepted 21 February 2022; Published 16 March 2022

Academic Editor: REN Fuqiang

Copyright © 2022 Xu Wu et al. This is an open access article distributed under the Creative Commons Attribution License, which permits unrestricted use, distribution, and reproduction in any medium, provided the original work is properly cited.

The engineering rock mass is generally composed of the rock matrix and structural plane and is an anisotropic inhomogeneous geological body. Accidents such as roof collapse and well caving caused by joint and fissure expansion occur frequently during tunnel excavation and service, resulting in serious casualties and economic losses. It is of great theoretical significance and engineering value to study the fracture mechanism of the jointed rock mass to ensure the stability of the surrounding rock and the safe and efficient utilization of the urban underground space. To investigate the effects of crossed cracks on mechanical properties and failure characteristics of rock, wire cutting equipment is employed to make rock samples with different crossed cracks, and then acoustic emission system and digital image correlation technique are used to study the fracture process of rock samples under uniaxial compression. It has been found that the strength of rock samples with a single crack is generally larger than that of samples with cross cracks, and the strength changed with the angle of the crack in a "V" shape. When the angle of preexisting crack is 60°, the rock strength reaches the lowest. The primary crack has a more obvious influence on rock strength and is the main controlling factor of rock fracture. The initiation stress of rock samples with a single crack changes more significantly with angle. When the angle of the primary crack is 45°, the rock sample is most prone to crack initiation failure, and the crack initiation stress is only 1/4 to 1/2 of the strength. There are two types of cracks: wing and anti-wing, and the tensile cracks are the main ones. It is revealed that the fracture of cracked rock has significant directional characteristics. For the samples with cross cracks, the primary crack is the main control factor of crack initiation, and the secondary crack has a certain guiding effect on the crack.

1. Introduction

Rock mass in nature is a heterogeneous and discontinuous multiphase composite material, which contains a large number of natural defects. Under the action of external loads, these preexisting joints or fissures will expand and connect with each other, thus forming macrocracks, resulting in rock mass failure. A large number of studies show that the geometry of joints (e.g., angle, width, length, quantity, and so on) has an important effect on the strength and deformation behavior of jointed rock masses. For example, Lajtai [1–3] studied the initiation law of preexisting cracks under external loading by using rock-like materials and summarized the types and propagation modes of new cracks in detail. Chen et al. [4–6] conducted uniaxial compression tests on samples made of gypsum and studied the influence of factors such as joint spacing, dip angle, and connectivity on the strength, elastic modulus, and stress-strain relationship of a discontinuous jointed rock mass. Liu et al. [7] systematically analyzed the peak strength and failure mode of preexisting jointed rock mass under uniaxial compression under seven working conditions, including different joint dip angles, joint coherence, and number of joint groups. Wang et al. [8] studied the combined effect of joint density and dip angle on the strength and deformation characteristics of the sample with open joints under uniaxial compression. Guo et al. [9, 10] used water jet cutter technology to prepare real granite cracked samples and analyzed the crack initiation law, strength characteristics, and failure mode of the cracked rock mass under uniaxial compression.

Furthermore, Shen et al. [11] conducted uniaxial compression tests on a series of cracked gypsum samples, analyzed the coalescing and fracture mechanisms of the rock bridge, and found that they were related to the relative positions of two parallel cracks. Zhou et al. [12] conducted an experimental study on rock samples with cross cracks, which demonstrated the generation, expansion, and merger process of two three-dimensional cracks in rock-like samples under uniaxial compression. Zhang et al. [13, 14] conducted uniaxial compression tests on 20 groups of rock samples containing cross cracks, studied the influence of the angle between primary and secondary cracks on the failure mode and mechanical properties of the rock samples, and explored the failure mechanism of the cross-cracked rock mass with Abaqus numerical software. With the aid of acoustic emission technology and a surface strain measurement system, Xu et al. [15] prefabricated orthogonal cross cracks with different distribution states with wire cutting equipment and analyzed the crack initiation stress, propagation path, and stress properties of granite samples under uniaxial compression. Chen et al. [16] studied the uniaxial compression mechanical properties and deformation law of the "T" shaped cross-cracked rock samples, and the study showed that the main crack dip angle played a decisive role in the peak stress of the sample, while the secondary crack affected the peak stress of the sample to a certain extent. Based on DIC and AE techniques, Pan et al. [17] studied the prefailure energy evolution of granite with conjugate joints in uniaxial compression tests.

Cross cracks widely exist in the actual rock mass. The laboratory study on the mechanical fracture evolution of samples with cross cracks at different angles can provide important guidance for rock mass engineering [18–20]. Although a large number of studies have been carried out on the mechanical properties and damage evolution of prefabricated rock samples with fractures, there are few studies on the mechanical characteristics of rock samples with fractures, and most of them are confined to the description and qualitative interpretation of experimental phenomena [21–23]. At present, the study of cross cracks in natural rocks is a research focus in the field of rock fracture mechanics [24–26]. In this paper, uniaxial compression experiments of granite samples with cross cracks were performed using the compression-testing machine system and the AE testing system. At the same time, the DIC system was used to study the evolution of the local stress field at different loading times. Based on physical tests, this paper will explore the strength characteristics and crack propagation law of cross-cracked granite samples, reveal their fracture mechanism, and provide theoretical guidance for the stability prediction of fractured rock mass and the deformation control of underground space engineering structure.

2. Cracked Samples and Testing Methods

The matrix of granite contains fine grains, and the granite with an average porosity of 1.29% is composed of quartz, potassium feldspar, and biotite. The average density of the samples is 2.6 g/cm^3, and the P-wave velocity is about 4950 m/s. In order to facilitate the monitoring of the crack propagation path during the loading test, the granite samples are machined to be cube with 50 mm length, 25 mm width, and 100 mm height. As illustrated in Figure 1, the central position of the sample is prefabricated with a size of 20 mm × 0.3 mm (primary crack) and 15 mm × 0.3 mm (secondary crack) through cracks. The primary crack and secondary crack are indicated by red line and blue line, respectively. The angle between the primary crack and the secondary crack is α, and the included angle between the primary crack and the vertical direction of the specimen is β. In the experiment, five included angle changes of 0°, 30°, 45°, 60°, and 90° were considered, so there are 25 distribution states of cross joints. The typical samples with cross cracks are shown in Figure 2.

Uniaxial compression tests are carried out on the GAW-2000 rigid testing machine as shown in Figure 3. The loading is controlled by the apparatus displacement with a speed of 0.03 mm/min. During the loading process, acoustic emission monitoring and digital image correlation technique are used to collect the acoustic emission data and surface strain data at intervals of 0.5 s and 1 s, respectively.

3. Test Results

3.1. Strength and AE Characteristics. The stress and AE events of the samples along the loading time are obtained in Figure 4. It can be found that with the loading time increasing, the stress of the sample gradually increases to the compression strength and then decreases suddenly because of failure. During the uniaxial compression test, there are almost no acoustic emission events in the crack compaction stage and elastic stage. Only when the crack initiation stage is reached, the acoustic emission count will increase suddenly. Therefore, we take the stress when the AE counts suddenly increase as the crack initiation stress. After rock initiation, AE events continue to occur, and cracks continue to develop and expand until rock failure. As shown in Figure 4, AE events occur at different time points due to the preexisting cracks, and the initiation stress of the rock also varies greatly with the preexisting cracks. The uniaxial compression strengths (i.e., UCS) and crack initiation stresses (i.e., CIS) of the samples with different cracks are shown in Table 1.

According to the data analysis in Table 1, the uniaxial compression strength and initiation stress of the cracked samples are lower than those of the samples without the crack. When the angles of β and α are 0° (i.e., the crack is parallel to the loading direction), the average value of uniaxial compression strength is 115.65 MPa and the average value of crack initiation stress is 88.27 MPa, which are the largest in the samples. On the contrary, the compressive strength and initiation stress of rock samples are the lowest when $\beta = 60°$ and $\alpha = 60°$. The variation in crack initiation stress with crack angle is shown in Figure 5.

As shown in Figure 5(a), when the angle of β is 0°, the initiation stress of the rock samples decreases gradually with the increase of α, when the two cracks are orthogonal, the initiation stress is the lowest, and the initiation stress of the crack has an obvious response to the variation of crack angle.

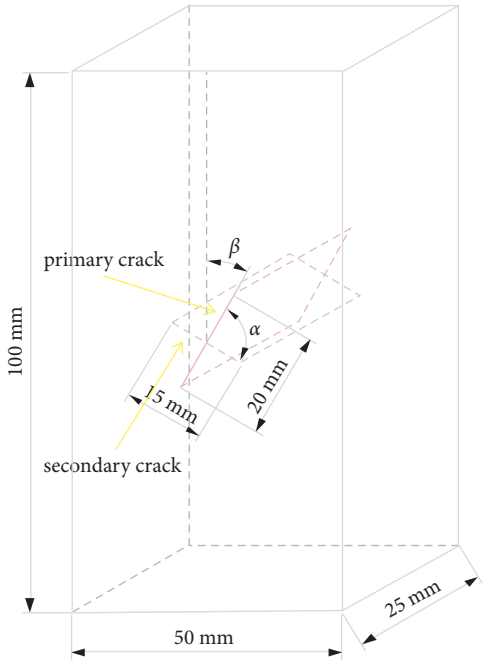

Figure 1: Illustration of the granite sample with crossed cracks.

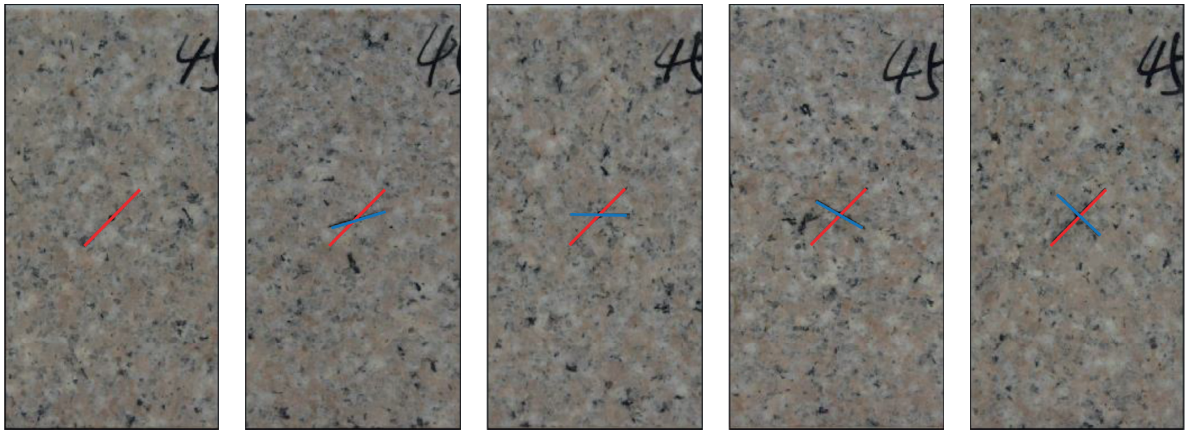

Figure 2: Cross-cracked samples: (a) $\alpha = 45^{\circ}$, $\beta = 0^{\circ}$; (b) $\alpha = 45^{\circ}$, $\beta = 30^{\circ}$; (c) $\alpha = 45^{\circ}$, $\beta = 45^{\circ}$; (d) $\alpha = 45^{\circ}$, $\beta = 60^{\circ}$; (e) $\alpha = 45^{\circ}$, $\beta = 90^{\circ}$.

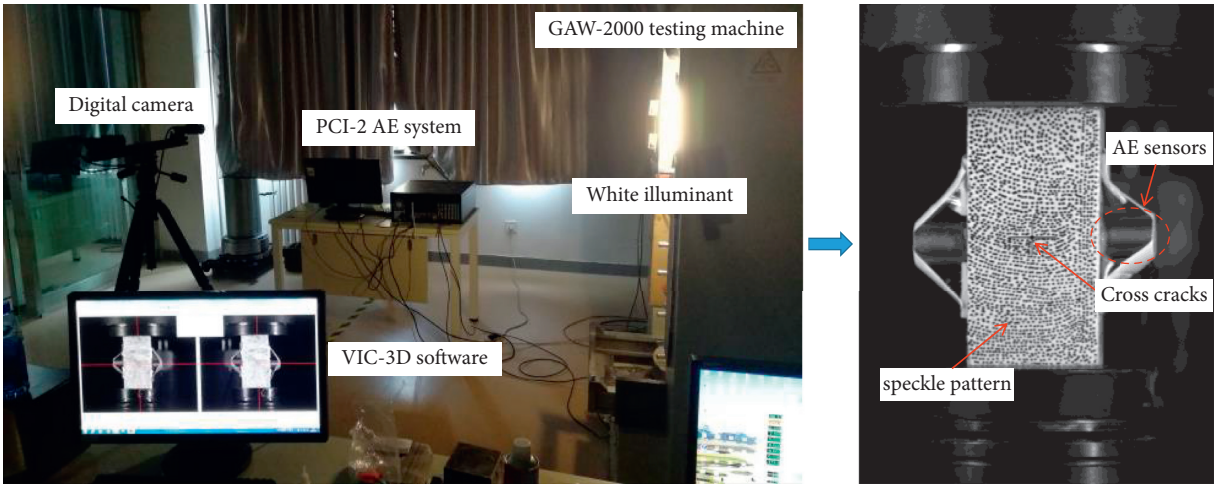

Figure 3: Testing system.

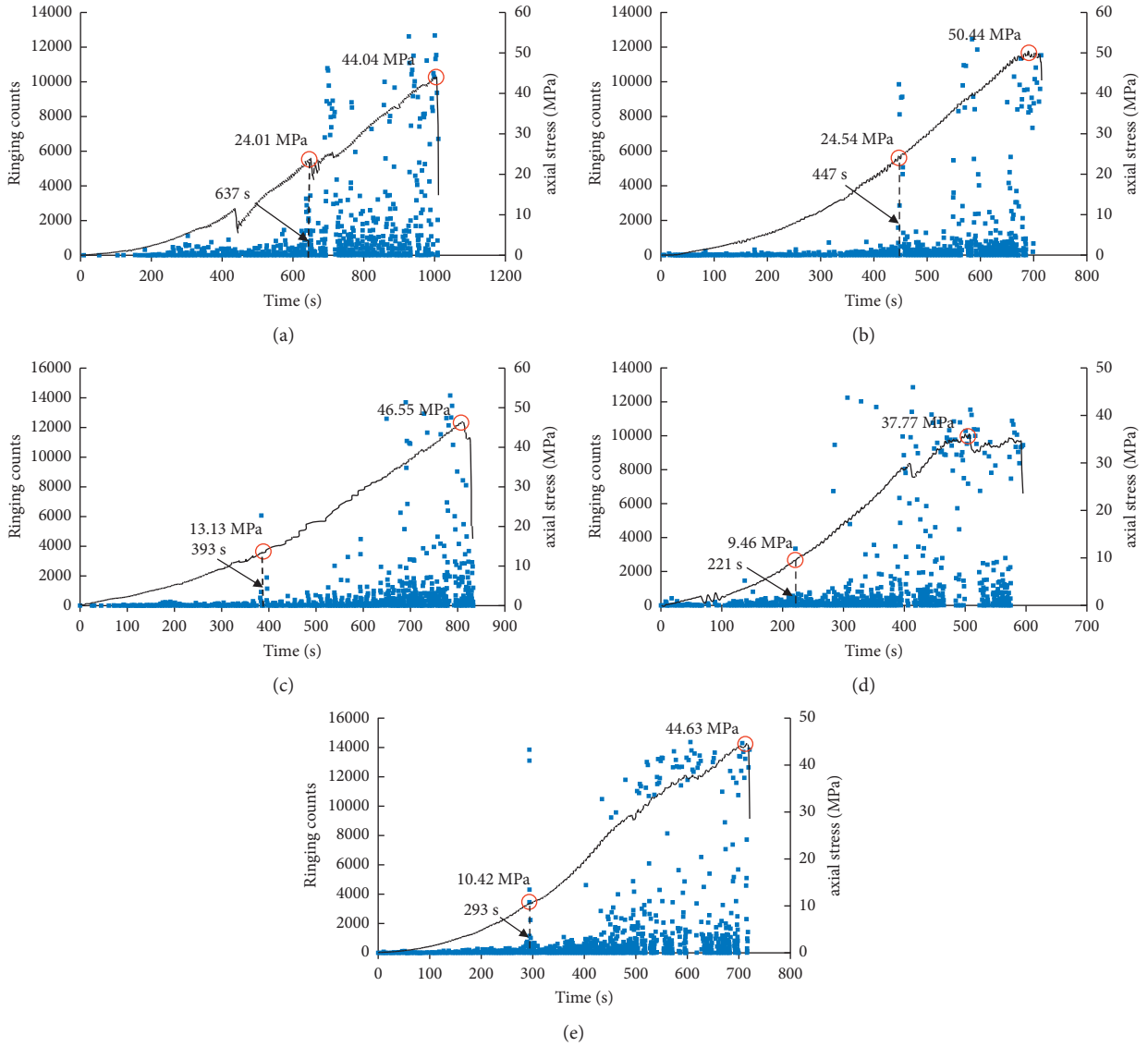

Figure 4: Acoustic emission ringing count-time-axial stress diagram: (a) $\alpha = 45^{\circ}$, $\beta = 0^{\circ}$; (b) $\alpha = 45^{\circ}$, $\beta = 30^{\circ}$; (c) $\alpha = 45^{\circ}$, $\beta = 45^{\circ}$; (d) $\alpha = 45^{\circ}$, $\beta = 60^{\circ}$; (e) $\alpha = 45^{\circ}$, $\beta = 90^{\circ}$.

When $\beta > 0^{\circ}$, the crack initiation stress varies less; however, according to the analysis of the overall variation law, the crack initiation stress of rock samples decreases first and then increases with the angle between cracks, and the crack initiation stress is generally minimum when α is 45° or 60°. Therefore, the smaller α, the higher the initiation stress of the rock. When the crack angle α is constant, the crack initiation stress of rock samples decreases first and then increases with the increase of the main crack angle β, as shown in Figure 5(b), the minimum initiation stress occurs when β is 45° or 60°, and the response of single crack to rock initiation stress is more significant.

The ratio of crack initiation stress to peak strength is defined as the crack initiation stress ratio η, $\eta = \sigma_i/\sigma_c$, where σ_i is the initiation stress of rock and σ_c is the peak strength of rock. According to the distribution range of η in Figure 6, the initiation stress of rock samples is 20% to 80% of the peak strength. The crack initiation stress ratio of rock samples with a single crack is generally larger than that of rock samples with cross cracks. When the angles of a single crack are 0° or 90°, η reaches 0.76 and 0.77, respectively. At this point, the sample exhibits a strong and rapid brittle failure, and the rapid development of cracks at the end of the crack leads to the overall failure of the sample. At the same time, the rock samples with higher initiation stress have more energy gathering before crack initiation and faster energy release rate after initiation.

When the crack angle α is constant, the crack initiation stress ratio η decreases firstly and then increases with the increase of β. When β is 45°, the rock sample is more prone to crack initiation, and the crack initiation stress is only 1/4 to 1/2 of the peak strength. Such rock samples are fractured under the action of lower load, and the energy gathered in the initial stage is released, the failure of rock samples is

Table 1: UCS and CIS of the samples with different crack angles.

Sample number	Uniaxial compression strength (i.e., UCS) (MPa)	Crack initiation stress (i.e., CIS) (MPa)	The stress ratio (between CIS and UCS)
00-00	115.65	88.27	0.76
00-30	97.85	46.98	0.48
00-45	52.43	33.49	0.64
00-60	57.61	23.07	0.40
00-90	47.91	19.28	0.40
30-00	80.76	29.38	0.36
30-30	64.44	29.60	0.46
30-45	59.35	24.49	0.41
30-60	62.91	25.94	0.41
30-90	62.12	26.31	0.42
45-00	44.04	24.01	0.55
45-30	50.44	24.54	0.49
45-45	46.55	13.13	0.28
45-60	37.77	9.46	0.25
45-90	44.63	10.42	0.23
60-00	38.26	17.22	0.45
60-30	40.55	16.20	0.40
60-45	43.74	21.35	0.49
60-60	25.23	9.08	0.36
60-90	41.64	24.32	0.58
90-00	43.14	33.33	0.77
90-30	40.94	18.03	0.44
90-45	42.45	14.99	0.35
90-60	46.33	23.88	0.52
90-90	36.94	23.20	0.63

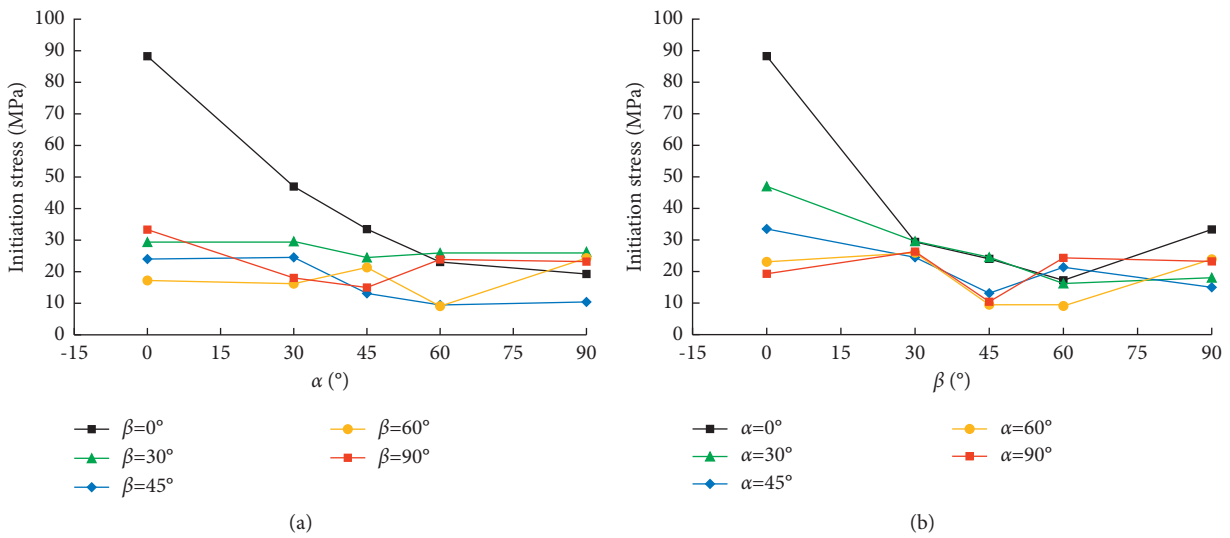

Figure 5: Variation law of crack initiation stress of rock with crossed cracks. (a) Relationship between crack initiation stress and α. (b) Relationship between crack initiation stress and β.

progressive, and the crack growth rate is relatively slow. On the contrary, when β is 0° or 90°, the crack stress ratio is higher. The failure process of two samples is relatively quick and shows a more obvious brittle failure characteristic. There is no obvious warning before rock failure, so it is difficult to prevent and predict such rock failure. According to the analysis of the initiation stress and the stress ratio η, when β is 45° or 60°, not only the initiation stress is low but also the fracture is easy to occur, and the crack has a great influence on the initiation characteristics of rock samples.

3.2. Surface Maximum Principal Strain Characteristics. There are usually two kinds of cracks at the preexisting crack end of rock material: wing cracks and secondary cracks. Most scholars believe that rock is dominated by wing

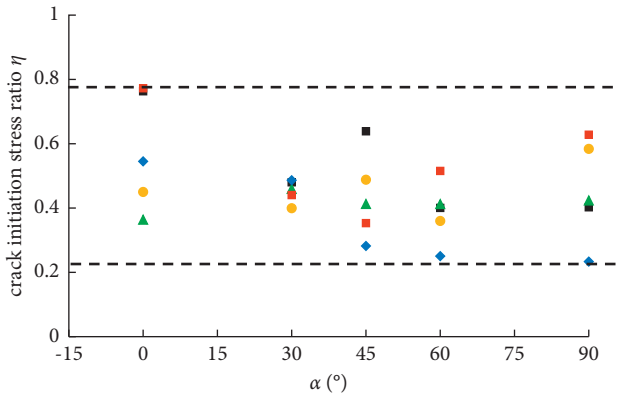

Figure 6: Distribution diagram of crack initiation stress ratio η.

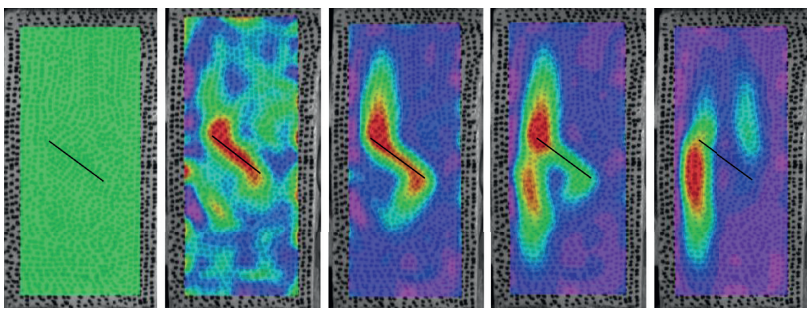

(a)

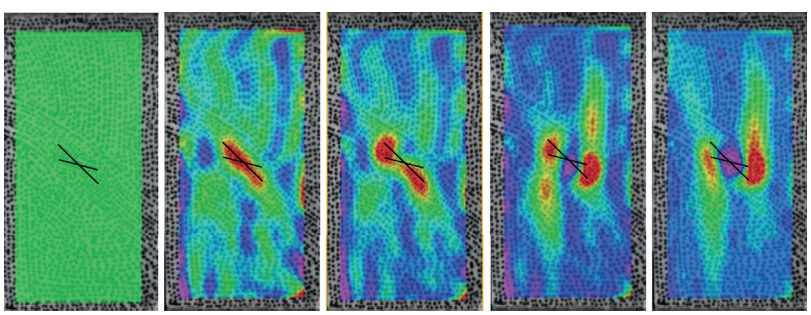

(b)

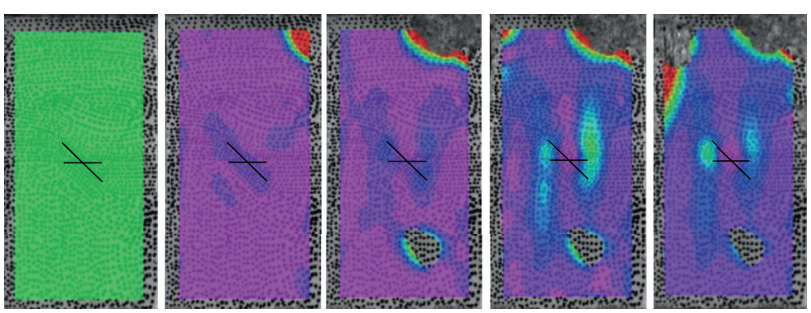

(c)

Figure 7: Continued.

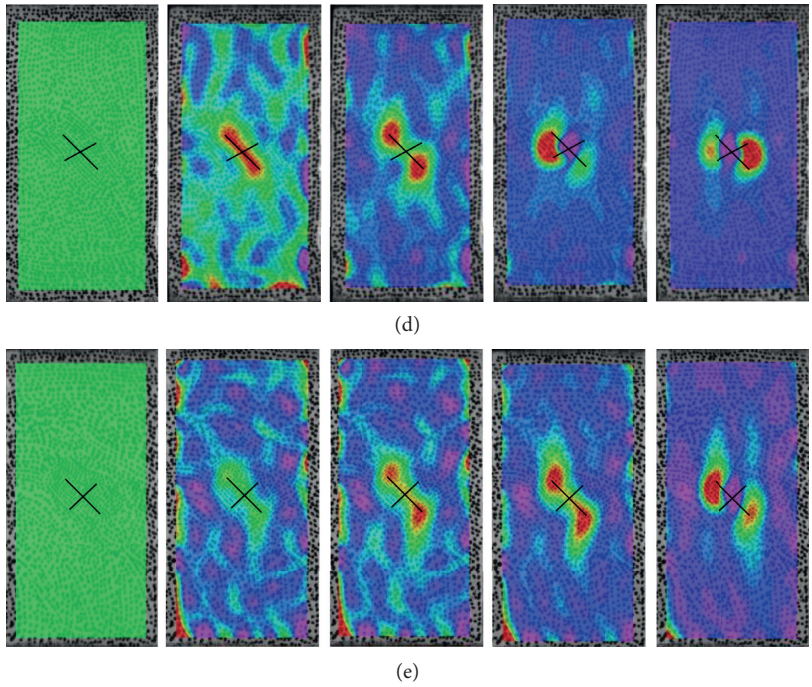

Figure 7: Surface maximum principal strain characteristics of the samples with different cross cracks: (a) $\alpha = 45^\circ$, $\beta = 0^\circ$; (b) $\alpha = 45^\circ$, $\beta = 30^\circ$; (c) $\alpha = 45^\circ$, $\beta = 45^\circ$; (d) $\alpha = 45^\circ$, $\beta = 60^\circ$; (e) $\alpha = 45^\circ$, $\beta = 90^\circ$.

initiation, and wing cracks under tensile stress start at the preexisting crack end and propagate along the direction of maximum load. However, the fracture of cracked rock is different from initiation, and a large number of tests show that the secondary crack caused by shear stress or compound stress is the main factor leading to the failure of samples. The final failure modes of rock with cross cracks are analyzed by using surface strain data, and the stress types and crack propagation characteristics leading to rock failure are discussed. The variation in surface deformation characteristics with crack propagation is shown in Figure 7.

Compared to the crack distribution characteristics of intact rock samples, the 00-00 sample presents a compression shear failure, forming a fracture zone with an angle of 27° with the loading direction. The failure of other rock samples with single cracks and cross cracks starts from the preexisting crack tip, generating wing or anti-wing cracks and expanding along the loading direction, resulting in the instability failure of the sample. Crack distribution patterns control and guide the initiation and failure of rocks. As the axial stress increases, the wing or anti-wing cracking occurs mainly at the crack end of rock under the action of tensile stress. According to the time of fracture and the analysis of the variation characteristics of the strain field on the rock surface shown in Figure 7, the fracture of the rock with cross cracks is mainly controlled by the primary crack and the secondary crack has a certain guiding effect on the propagation of the crack.

For the sample whose primary crack is perpendicular to the loading direction, an oval stress concentration zone appears in the middle of the crack at the initial loading stage. As shown in Figure 7, with the increase of axial stress, the stress concentration zone shifts from the vicinity of the secondary crack to the tip of the primary crack, and the crack initiation is approximately parallel to the loading direction. Therefore, when there is a crack orthogonal to the loading direction in the rock sample, this crack controls the new crack initiation and failure of the rock. The crack initiation is concentrated at the end of the preexisting crack and extends to both ends of the sample in a form approximately parallel to the loading direction. According to the initiation position, when the included angle between the secondary crack and the vertical direction of the specimen is small, the crack initiation is located at the upper or lower part of the preexisting crack and cracks in one side direction. When the included angle between the secondary crack and the vertical direction of the specimen is greater than 45°, the initiation crack is concentrated and symmetrically distributed at the midpoint of the primary crack.

4. Conclusions

An experimental approach on the crack initiation mechanism in granite samples under uniaxial compression was carried out. Some conclusions could be drawn as follows.

The uniaxial compression test of rock with cross cracks was carried out, and the variation law of peak strength and crack initiation stress of granite with cross cracks was obtained. It was found that the strength of rock with a single crack is generally larger than that of rock with cross cracks, and the strength of the sample changed with the angle of crack in a "V" shape. When the angle of preexisting crack is 60°, the rock strength reaches the lowest. The primary crack

has more obvious influence on rock strength and is the main controlling factor of rock fracture.

Acoustic emission monitoring tests were carried out to determine the crack initiation stress by acoustic emission ringing counting, and the variation law of crack initiation stress at crack end was obtained. When the crack angle is constant, the crack initiation stress decreases first and then increases with the increase of the primary crack angle. The crack initiation stress of rock samples with a single crack changes more significantly with angle. The ratio of crack initiation stress to peak strength is taken as an index to judge the degree of rock failure. When the inclination angle of the primary crack is 45°, the rock sample is most prone to crack initiation failure, and the crack initiation stress is only 1/4 to 1/2 of the peak strength.

By means of the non-contact surface strain field (DIC) device, the law of crack initiation and the distribution pattern of cracks in rock samples with intersecting fractures are studied. Cracks are found to be mainly wing or anti-wing, and the tensile cracks are the main ones. It is revealed that fracture of cracked rock has significant directional characteristics. For the samples with cross cracks, the primary crack is the main control factor for crack initiation, and the secondary crack has a certain guiding effect on the crack.

It is an important means to control the crack initiation in underground tunnel engineering to prevent side falling and roof-fall accidents. According to the crack initiation mechanism and the variation characteristics of the crack initiation stress and the maximum strength, the accurate support scheme for the fractured rock mass as well as the key construction part and the time node of the protection project can be established by combining the magnitude of the pressure and direction of the slope or the underground engineering.

Data Availability

The experimental data used to support the findings of this study are included within the article.

Conflicts of Interest

The authors declare that there are no conflicts of interest regarding the publication of this paper.

Acknowledgments

This research was funded by the Beijing Municipal Natural Science Foundation (grant no. 8214049).

References

[1] E. Z. Lajtai, "Brittle fracture in compression," *International Journal of Fracture*, vol. 10, no. 4, pp. 525–536, 1974.

[2] A. Bobet and H. H. Einstein, "Fracture coalescence in rock-type materials under uniaxial and biaxial compression," *International Journal of Rock Mechanics and Mining Sciences*, vol. 35, no. 7, pp. 863–888, 1998.

[3] M. Sagong and A. Bobet, "Coalescence of multiple flaws in a rock-model material in uniaxial compression," *International Journal of Rock Mechanics and Mining Sciences*, vol. 39, no. 2, pp. 229–241, 2002.

[4] X. Chen, J. Sun, P. Yang, and Z. Feng, "Influence of joint spacing and inclination angle on fragmentation characteristic of rock masses under uniaxial compression," *Journal of Mining & Safety Engineering*, vol. 34, no. 3, pp. 608–614, 2017, in Chinese.

[5] X. Chen, D. Li, and L. Wang, "Experimental study on effect of spacing and inclination angle of joints on strength and deformation properties of rock masses under uniaxial compression," *Chinese Journal of Geotechnical Engineering*, vol. 36, no. 12, pp. 2236–2245, 2014, in Chinese.

[6] X. Chen, Z. Liao, and D. Li, "Experimental study of effects of joint inclination angle and connectivity rate on strength and deformation properties of rock masses under uniaxial compression," *Chinese Journal of Rock Mechanics and Engineering*, vol. 30, no. 4, pp. 781–789, 2011, in Chinese.

[7] H. Liu, Y. Huang, and K. Li, "Test study of strength and failure mode of pre-existing jointed rock mass," *Rock and Soil Mechanics*, vol. 34, no. 5, pp. 1235–1241, 2013, in Chinese.

[8] P. Wang, P. Cao, and C. Pu, "Effect of the density and inclination of joints on the strength and deformation properties of rock-like specimens under uniaxial compression," *Chinese Journal of Engineering*, vol. 39, no. 4, pp. 494–501, 2017, in Chinese.

[9] Q. Guo, W. U. Xu, and M. Cai, "Experiment on the strength characteristics and failure modes of granite with pre-existing cracks," *Chinese Journal of Engineering*, vol. 41, no. 01, pp. 43–52, 2019, in Chinese.

[10] Q. Guo, W. U. Xu, and M. Cai, "Crack initiation mechanism of pre-existing cracked granite," *Journal of China Coal Society*, vol. 44, no. S2, pp. 476–483, 2019, in Chinese.

[11] B. Shen, O. Stephansson, H. H. Einstein, and B. Ghahreman, "Coalescence of fractures under shear stresses in experiments," *Journal of Geophysical Research: Solid Earth*, vol. 100, no. B4, pp. 5975–5990, 1995.

[12] X.-P. Zhou, J.-Z. Zhang, and L. N. Y Wong, "Experimental study on the growth, coalescence and wrapping behaviors of 3D cross-embedded flaws under uniaxial compression," *Rock Mechanics and Rock Engineering*, vol. 51, no. 5, pp. 1379–1400, 2018.

[13] Bo Zhang, S. Li, and X. Yang, "Uniaxial compression failure mechanism of jointed rock mass with cross-cracks," *Rock and Soil Mechanics*, vol. 35, no. 7, pp. 1863–1870, 2014, in Chinese.

[14] Bo Zhang, S. Li, and X. Yang, "Uniaxial compression tests on mechanical properties of rock mass similar material with cross-cracks," *Rock and Soil Mechanics*, vol. 33, no. 12, pp. 3674–3679, 2012, in Chinese.

[15] W. U. Xu, F. Wang, and X. I. Xun, "Experimental investigation on the strength characteristics and fracture mechanism of rock with orthogonally crossed cracks," *Journal of China Coal Society*, vol. 45, no. 7, pp. 2681–2690, 2020, in Chinese.

[16] Y. Chen, P. U. Cheng, and G. Li, "Experimental study on mechanical properties of rock mass samples with T-shaped cross crack subjected to uniaxial compression," *Journal of Experimental Mechanics*, vol. 34, no. 4, pp. 684–692, 2019, in Chinese.

[17] J. Pan, X. Wu, Q. Guo, and X. Xi, "Uniaxial experimental study of the deformation behavior and energy evolution of conjugate jointed rock based on AE and DIC methods," *Advances in Civil Engineering*, vol. 2020, Article ID 8850250, 16 pages, 2020.

[18] J. Pan, F. Ren, and M. Cai, "Effect of joint density on rockburst proneness of the elastic-brittle-plastic rock mass," *Shock and Vibration*, vol. 2021, Article ID 5574325, 9 pages, 2021.

[19] J. Sun, F. Wang, Z. Li, and D. Ren, "A new hybrid copula-based nonparametric Bayesian model for risk assessments of water inrush," *Quality and Reliability Engineering International*, p. 20, 2022.

[20] C. Zhu, M. C. He, X. H. Zhang, Z. G. Tao, Q. Yin, and L. F. Li, "Nonlinear mechanical model of constant resistance and large deformation bolt and influence parameters analysis of constant resistance behavior," *Rock and Soil Mechanics*, vol. 42, no. 7, pp. 1911–1924, 2021.

[21] C. Zhu, M. C. He, B. Jiang, X. Z. Qin, Q. Yin, and Y. Zhou, "Numerical investigation on the fatigue failure characteristics of water-bearing sandstone under cyclic loading," *Journal of Mountain Science*, vol. 18, no. 12, pp. 3348–3365, 2021.

[22] G. Li, Y. Hu, S. M. Tian, M. Weibin, and H. L. Huang, "Analysis of deformation control mechanism of prestressed anchor on jointed soft rock in large cross-section tunnel," *Bulletin of Engineering Geology and the Environment*, vol. 80, no. 12, pp. 9089–9103, 2021.

[23] M. Z. Gao, J. Xie, Y. N. Gao et al., "Mechanical behavior of coal under different mining rates: a case study from laboratory experiments to field testing," *International Journal of Mining Science and Technology*, vol. 31, no. 5, pp. 825–841, 2021.

[24] M. Z. Gao, H. C. Hao, S. N. Xue et al., "Discing behavior and mechanism of cores extracted from Songke-2 well at depths below 4,500 m," *International Journal of Rock Mechanics and Mining Sciences*, vol. 149, Article ID 104976, 2022.

[25] C. Cao, W. Zhang, J. P. Chen, B. Shan, S. Y. Song, and J. W. Zhan, "Quantitative estimation of debris flow source materials by integrating multi-source data: a case study," *Engineering Geology*, vol. 291, Article ID 106222, 2021.

[26] Z. Dou, S. X. Tang, X. Y. Zhang et al., "Influence of shear displacement on fluid flow and solute transport in a 3D rough fracture," *Lithosphere*, vol. 2021, Article ID 1569736, 2021.

Hindawi
Advances in Materials Science and Engineering
Volume 2022, Article ID 3365402, 12 pages
https://doi.org/10.1155/2022/3365402

Research Article

Analysis of Instability Mechanism and Induced Cause of Urban Pavement in Xining City, China

Gan Qi,[1] Zhenyu Wang,[1,2] Yu Chen,[3] Chun Zhu,[4,5] Dazhong Ren,[5] Tao Tian,[6] and Fu Yang[6]

[1]*China Institute of Geo-Environment Monitoring, Beijing 100081, China*
[2]*State Key Laboratory of Deep Rock Mechanics and Underground Engineering, Beijing 100083, China*
[3]*Research Institute of Geotechnical Engineering, Hohai University, Nanjing 210098, Jiangsu, China*
[4]*School of Earth Sciences and Engineering, Hohai University, Nanjing 210098, China*
[5]*Shanxi Key Laboratory of Advanced Stimulation Technolgy for Oil & Gas Reservoirs, College of Petroleum Engineering, Xi'an Shiyou University, Xian 710065, China*
[6]*Key Lab of Coal Resources Exploration and Comprehensive Utilization, MNR, Shanxi Coal Geology Group Co.,Ltd., Xi'an 710021, China*

Correspondence should be addressed to Yu Chen; yuchen0420@hhu.edu.cn

Received 26 November 2021; Revised 13 December 2021; Accepted 24 January 2022; Published 8 February 2022

Academic Editor: Abílio De Jesus

Copyright © 2022 Gan Qi et al. This is an open access article distributed under the Creative Commons Attribution License, which permits unrestricted use, distribution, and reproduction in any medium, provided the original work is properly cited.

As a large human gathering place, the city directly causes huge property losses and casualties due to the ground collapse accident every year. In order to explore the causes and damage characteristics of urban ground collapse, taking Xining City, Qinghai Province, as an example, this paper analyzes the accidental factors causing ground collapse through on-site geological exploration and then expounds the deformation characteristics of urban ground collapse by using the numerical simulation method of Fluent and PFC. Using the collapsible balance method, it is obtained that the insufficient thickness of the top plate of the Loess Soil Subgrade in the collapse pit area is the inevitable factor causing the final collapse. The results show the following: (1) The failure of water supply pipe is an accidental factor leading to the formation of underground cavity, and the ground collapse accident is hidden, sudden, and of high risk, and its deformation and failure development process is slow. (2) The critical thickness of the roof above the air raid shelter is about 22 m, and the actual thickness is about 11.6 m, which is prone to deformation and uneven settlement, which is also an inevitable factor causing ground collapse. (3) The numerical simulation study shows that the final formation deformation range is about 16 m. At this time, the height of the formed cavity is about 9 m. The plastic zone tends to develop around, and the maximum settlement position appears above the air raid shelter. (4) The collapse process includes four stages: water supply pipeline leakage, underground cavity formation, collapse critical state, and ground collapse. This research and analysis provides theoretical guidance and scientific basis for the investigation, measurement, detection, and monitoring of various underground pipe networks of urban roads.

1. Introduction

Ground collapse refers to a phenomenon or process caused by the downward collapse of surface rocks and soil under the influence of natural factors or human engineering activities, as well as the formation of collapse pits (holes) on the ground. Generally, there are four types: karst collapse [1–4], goaf collapse [5–7], loess collapse [8–11], and engineering collapse [12]. With the vigorous development of China's modernization, cities are mainly characterized by concentrated population and dense buildings. Different from the ground subsidence with large scope and small deformation, the pavement collapse has the characteristics of great destructiveness, high concealment, and sudden occurrence. In the process of urban road collapse, human activities play an important role, and, at the same time, its occurrence usually brings great influence on human society [13]. Once the road collapse occurs in urban areas, it will often cause road damage, which may cause traffic congestion at least or heavy property losses and casualties. For example,

on February 7, 2018, the tunnel segment was damaged and the ground collapsed at the construction site of the right line of the Lvdaohu-Huyong shield tunneling section of Foshan Metro Line 2 due to flooding. The collapse pit was about 30 m long, resulting in 10 deaths and 1 loss of contact. At the same time, the ground collapse in the urban area will increase the uneven settlement of the surrounding building foundations in the collapsed area and even lead to the collapse of the building [14]. The 2011–2020 National Land Subsidence Prevention and Control Plan, jointly compiled by the Ministry of Land and Resources, the Ministry of Water Resources, the Development and Reform Commission, the Ministry of Finance, and ten other ministries and commissions, points out that there are currently more than 50 cities in the country suffering from land subsidence disasters, distributed in Beijing, Tianjin, and Shanghai. In Jiangsu, Hebei, Shanxi, Inner Mongolia, and 20 other provinces, autonomous regions, and municipalities, the country's cumulative land subsidence of more than 200 millimeters reached 79,000 square kilometers, and there is a trend of further expansion, of which the Yangtze River Delta, the North China Plain, and the Fenwei Basin are the most prominent. According to the statistical data of the "China Statistical Yearbook," in the past five years, our country has experienced 966 ground collapse disasters, and an average of about 300 people die from the disaster every year. Strictly speaking, ground collapse and collapse, mudslides, landslides, and so forth are all typical geological disasters. There are many factors that induce pavement collapse in urban areas, and water is usually the main factor, including groundwater action and surface water infiltration. Secondly, loess, when it meets water, has collapsibility effect and forms collapse [15]. Water mainly causes collapsibility, erosion, differential pressure, and so forth [16, 17]. Under the action of infiltration, the soil is prone to two failure modes, namely, pipe gushing and soil flow [18]. Under the action of water seepage, the fine-grained soil in the soil is washed away by water, and the remaining large particles form a soil skeleton with poor stability and easy instability, forming the initial underground pores [19]. Yechieli et al. [15] studied over 4000 sinkholes in Israel and found that their formation is related to the shrinking underground system around the Dead Sea. Selleri et al. [20] studied the Karst landform of Salento Peninsula and found that groundwater and surface water were the main factors causing multiple sudden subsidence. Ouyang [21] believes that the ground collapse process is divided into four stages: groundwater level drop, cavern formation, cavern expansion, and ground collapse formation. Among them, the seepage force generated by underground underwater seepage is the power source of ground collapse. Cao, Peng et al., Gao, Hu, and others found through research that ground collapse is mainly related to groundwater and surface water activities [22–25]. Rock integrity also weakens under repeated wetting conditions over long periods of time [26]. At the same time, cyclic rainfall will also affect the physical and mechanical properties of rock mass deformation [27].

Urban underground construction activities have destroyed the original stable state of the soil, and a little carelessness will cause the ground to collapse. For example, during the construction of Kurtkulag irrigation tunnel, many ground collapse accidents occurred mainly at the exit and entrance of the tunnel and the location where the tunnel crosses the fault [28]; Hou et al. [29] pointed out that the existence of underground holes greatly reduced the strength of the ground and the ability of resisting subsidence and divided Beijing subway accidents into five categories. Ma et al. [30] analyzed the causes of three consecutive ground collapses in a subway tunnel within half a month after the start of the shield machine and found that the causes of ground collapses in the process of shield construction mainly include four aspects: engineering geological conditions, auxiliary engineering quality problems, excavation management, and shield machine failure.

Xining has a semiarid climate on a continental plateau with an average annual rainfall of 380 mm. Huangshui and its tributaries, Nanchuan River and Beichuan River, converge in the urban area from west, south, and north and flow through the city to the east. Xining City, as the political, economic, scientific, educational, cultural, transportation, and communication center of Qinghai Province, has seen at least 14 road collapse accidents since 2014, which seriously threatened the lives and properties of urban residents. Through detailed investigation and research on road collapse accidents in urban areas, not only can corresponding measures be taken against road collapse accidents, but also they have long-term significance in preventing such incidents from recurring throughout the country.

In this study, through the investigation of the geological and hydrological conditions and the collapse situation of the pavement collapse area in Xining City on January 13, the critical roof thickness of loess-like soil subgrade in the collapse pit area was calculated and analyzed by using the numerical simulation method of Fluent and PFC joint calculation. Finally, the cause of collapse and failure mechanism are analyzed in combination with the field situation. In addition, this paper also puts forward reasonable suggestions and measures to reduce the occurrence of such disasters again and do a good job of deformation monitoring between the collapse pit and surrounding buildings to prevent secondary damage [31]. The formation of collapse pit reduces the stability of the inner pit, so the inner wall of collapse pit should be monitored and strengthened in time [32].

2. Engineering Geological Conditions

2.1. Study Area. The road collapse accident that occurred on January 13, 2020, was at the Red Cross Bus Station at the entrance of the Great Wall Hospital, South Street, Chengzhong District, Xining City (Figure 1). The cavity formed after the collapse is nearly elliptical cone-shaped, with a diameter about 9–10 meters, a visible depth about 8–10 meters, and a ground area about 80 square meters (Figure 2). On its east side wall, there are buried water supply pipes, cables, gas, and other pipes network. The water supply pipe network, communication cables, and gas pipe network

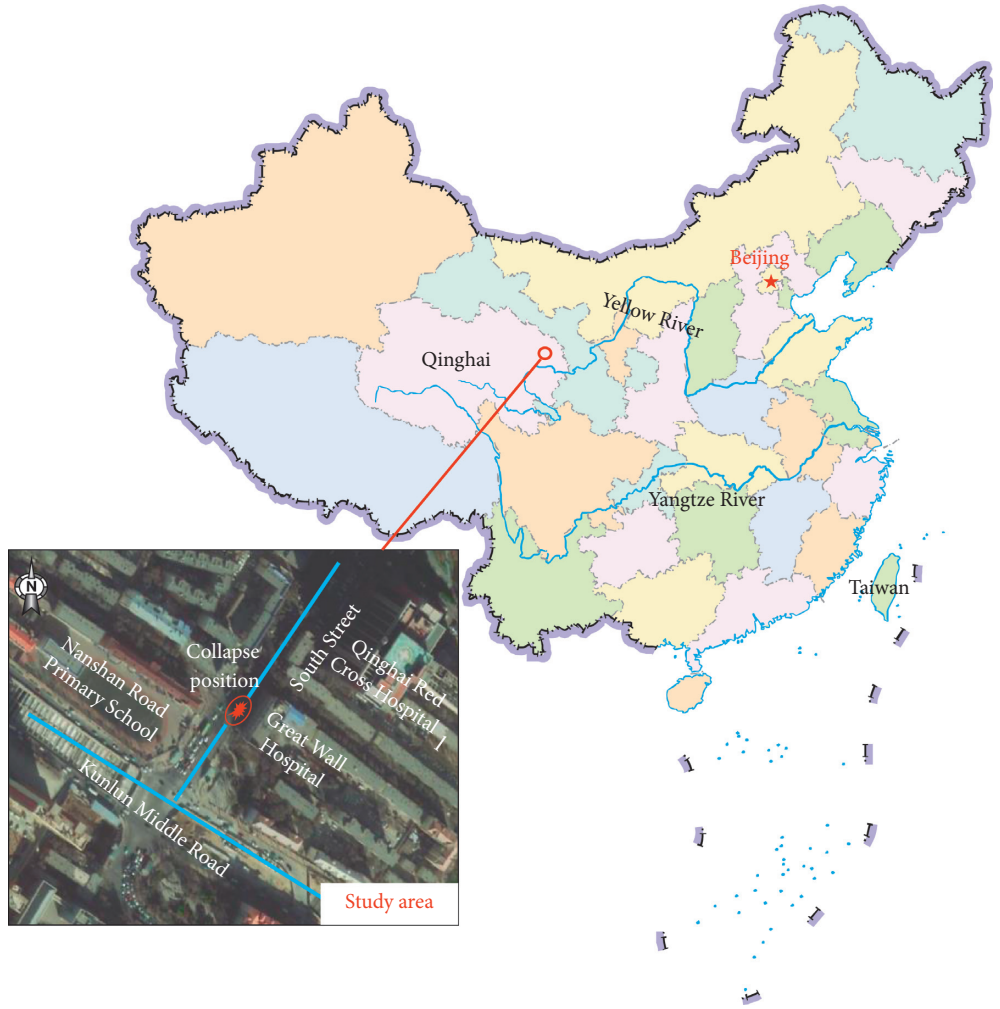

Figure 1: Location map of the collapsed area.

spread out in the north-south direction are buried 1.5–2 meters deep, and the power supply pipeline network spread out in the east-west direction is 2–4 meters deep. The accident resulted in the bus and train platform collapse into a pit, eventually killing 10 people and injuring 17.

2.2. Geomorphological Characteristics. The central area of Xining City is mainly composed of modern riverbeds and terraces of the main stream of Huangshui River, piedmont alluvial plains, and alluvial plains. The terrain is relatively flat and open, distributed in a belt along the river. The geomorphology is mainly caused by accumulation and erosion. The south bank of the Huangshui River is composed of I–III terraces and is the main concentrated construction area of the city. From the north of the Huangshui River to the south of the first-level terrace, the slope is from 1 to 2°, the second-level terrace is from 3 to 5°, and it gradually steepens to the third-level terrace to the south, with a slope of 4–6°, as well as low hills in the south. The front edge of the area has a slope of 25–30°.

The south side of the Huangshui River Valley is a hilly area with beams and ridges, which is strongly eroded by gullies and the terrain is very fragmented. Loess and clastic rocks constitute the main lithology of hilly areas. Loess is mainly covered on the top of the hilly area, and local sections are distributed along the slope of the hillside.

The landform unit in the collapsed area belongs to the third-level terrace on the south bank of the Huangshui River, about 150 m away from the front edge of the third-level terrace. Due to the construction of the South Street, the original steep ridge was transformed into a road, with a slope of 5-6° and a nearly east-west direction. The overall terrain is high in the west and low in the east, high in the south, and low in the north. The elevation of the site is 2271.72–2254.52 m, the surface elevation difference is 17.2 m, and the terrain is flat and open; no faults have been found passing through the site after investigation. The underground manned air raid shelter passes through.

2.3. Geological Characteristics. The Xining Basin is located in the Qilian stratigraphic zone. Due to the influence of the strong vertical movement of the crust and the strong transformation of the rivers and piedmont alluvium, the Quaternary system has created the current basin landscape.

Figure 2: Collapse area situation.

The main exposed strata in the basin are Paleoproterozoic, Triassic, Jurassic, Cretaceous, Paleogene, Neogene, and Quaternary. The Quaternary strata can be divided into alluvial deposits, alluvial proluvial deposits, slope proluvial deposits, and aeolian deposits according to their genetic types.

According to the on-site geological survey, a detailed study of the rock and soil in the collapsed area is carried out (Figure 3). The surface layer is the Quaternary artificial fill, which is mainly composed of earthy yellow and gray-black variegated silt, gravel, construction waste, and a small amount of construction waste. The range is 0.5–3.8 m. The lower layer is tertiary alluvial and alluvial loess-like soil, mainly composed of yellow silt, with needle-like pores, developed vertical joints and fissures, calcareous cementation, poor toughness, and easiness to soften and corrode in contact with water. Collapsibility is divided into collapsible loess (buried depth of about 1.5–10.3 m) and noncollapsible loess (buried depth of about 10.3–11.4 m). The roof of the underground air raid shelter was excavated at a buried depth of 11.6 meters. The third layer is mainly the pebble layer of tertiary lacustrine layer and alluvial layer, composed of blue-gray, gray-white sandstone, limestone, quartzite, and a small amount of light-colored metamorphic rock. The pebble layer is also mixed with silty clay layer.

2.4. Hydrogeological Characteristics. The collapse area is located at the front edge of the third terrace on the south bank of the Huangshui River. Quaternary pore water exists on the site. The stable groundwater level is 20.8–29.0 m and the groundwater elevation is 2233.72–2342.72 m. The groundwater is mainly affected by the complementation of Huangshui River and the south. The recharge of the underground runoff on the side is discharged in the downstream area in the form of torrents, and the groundwater flows from the southwest to the northeast and is finally discharged to the Huangshui River. The dynamic changes are seasonally obvious, and the annual water level change range is about 1.0–1.5 m.

3. Causes and Mechanism of Collapse

According to the public meteorological data, there is no obvious precipitation process from December 2019 to the afternoon of January 13, 2020. The surface pavement in the surface area is covered by asphalt concrete, and the permeability is poor. Therefore, the formation of collapse pit can exclude the influence of groundwater and surface water. According to the on-site infiltration and collapse inspection, the water supply pipe which was wrongly broken on the east side of the pit wall had a buried depth about 1.5 m, a diameter of 50 cm, and a wall thickness of 0.6 cm. The material is cast iron. A water drop hole with a diameter about 0.8 m and a depth about 7 meters is formed at the lower part.

3.1. Engineering Geological Structure Model. After the accident, through the detailed investigation of the spatial structure of the collapse location, it is determined that there is an air raid shelter with a width of 1.5 m and a height of 2.5 m at the depth of 11.6 m from the ground, which is a rubble precast arch structure, and the location is roughly coincident with the collapse area. Combined with the results of geological survey of hydraulic engineering environment, based on the geomorphic unit as the main division basis, considering the characteristics of geotechnical engineering

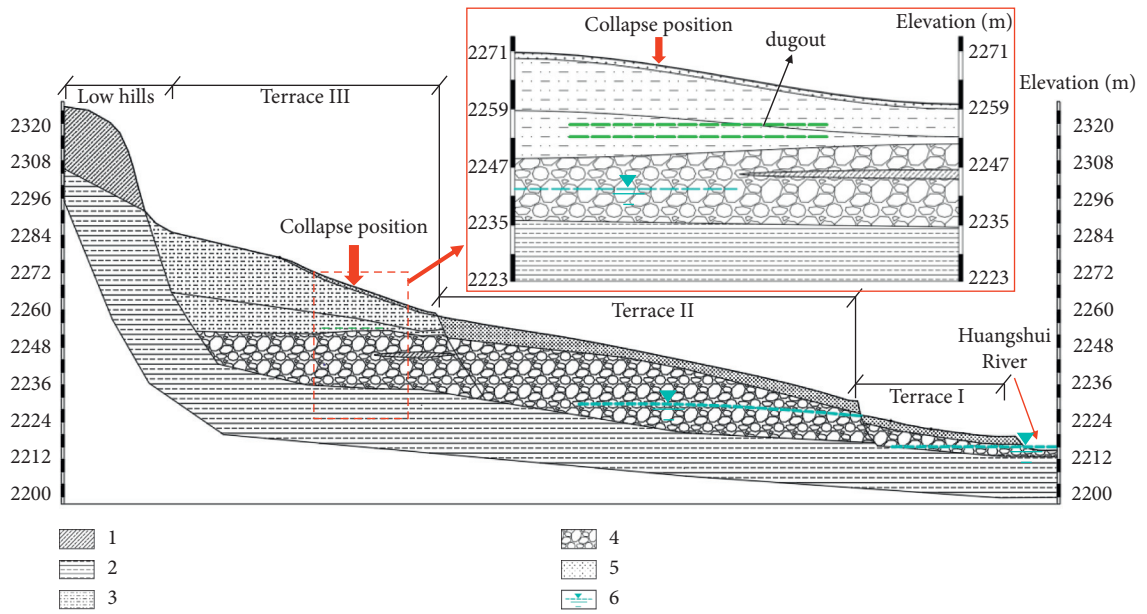

Figure 3: Engineering geological section. (1) Silty clay; (2) mudstone; (3) loess; (4) pebble; (5) miscellaneous fill; (6) groundwater level.

geomechanics, and based on the spatial analysis function of MAPGIS, a three-dimensional engineering geological structure model of the main urban area of Xining City is established, which stereoscopically shows the stratum situation and underground space distribution of the accident area in Figure 4.

3.2. Analysis of the Causes of Collapse

3.2.1. Analysis of Critical Roof Thickness of Loess Subgrade. The main stratum below the collapse area is collapsible loess soil and there are air raid shelters, so it is necessary to calculate the critical roof thickness of Loess Soil Subgrade in the collapse pit area.

The collapse equilibrium method not only considers the influence of the mechanical properties of the rock and soil but also considers the stress state of the surrounding rock of the collapse pit, especially the influence of the lateral stress. This method is suitable for the collapse pit whose shape is round or arched. According to the equilibrium condition of the collapse body, when the shear force of the rock and soil mass on the top of the collapse pit is equal to the self-weight of the upper rock and soil mass and the external additional load, the roof thickness of the collapse pit is considered as the critical thickness. The calculation model is shown in Figure 5.

According to the calculation model in Figure 5, a circular thin layer element with thickness dz is selected in loose rock and soil. The friction dF acts on the periphery of the element. The friction dF of the element can be determined according to Coulomb's law:

$$dF = 2\pi a\left(c + \sigma_H \tan\phi\right)dz = 2\pi a\left(c + \xi\gamma Z \tan\phi\right)\mathrm{d}z. \quad (1)$$

In the above equation, σH is normal stress around rock and soil mass; c and ϕ are cohesion and internal friction angle of rock and soil mass, respectively; ξ is lateral pressure coefficient, $\xi = \tan^2(45^\circ - \varphi/2)$.

By integrating the above formula on the interval [0, H], we obtain

$$F = 2\pi acH + \pi a\xi H^2 \tan\phi. \quad (2)$$

The overburden soil mass and additional load are as follows:

$$G = \pi a^2\left(\gamma H + p_0\right), \quad (3)$$

and when the rock and soil are in the limit equilibrium state, the critical thickness of the roof can be obtained:

$$H_{cr} = \frac{a\gamma - 2c + \sqrt{(a\gamma - 2c)^2 + 4ap_0\xi\gamma\tan\phi}}{2\xi\gamma\tan\phi}, \quad (4)$$

where a is collapse radius, m; γ is gravity of rock and soil mass, kN/m^3; p_0 is upper uniform load, kPa.

According to the test results of the geometric dimensions of the "1.13" pavement collapse pit and the physical and mechanical properties of loess soil in Xining City, Qinghai Province, $a = 4.5m$; $\gamma = 15.6kN/m^3$; $c = 15MPa$; $\phi = 19.5^\circ$; $p_0 = 100kPa$, and $H_{cr} = 22$m.

According to the calculation results, the critical thickness of the roof above the air raid shelter is about 22 m.

According to the data, the actual thickness of the roof above the air raid shelter is about 11.6 m, which is far less than the critical thickness of the roof, which will lead to the deformation and uneven settlement of the subgrade above the area under long-term repeated load. The thickness of the roof thinning is gradually made. Then, when the upper load

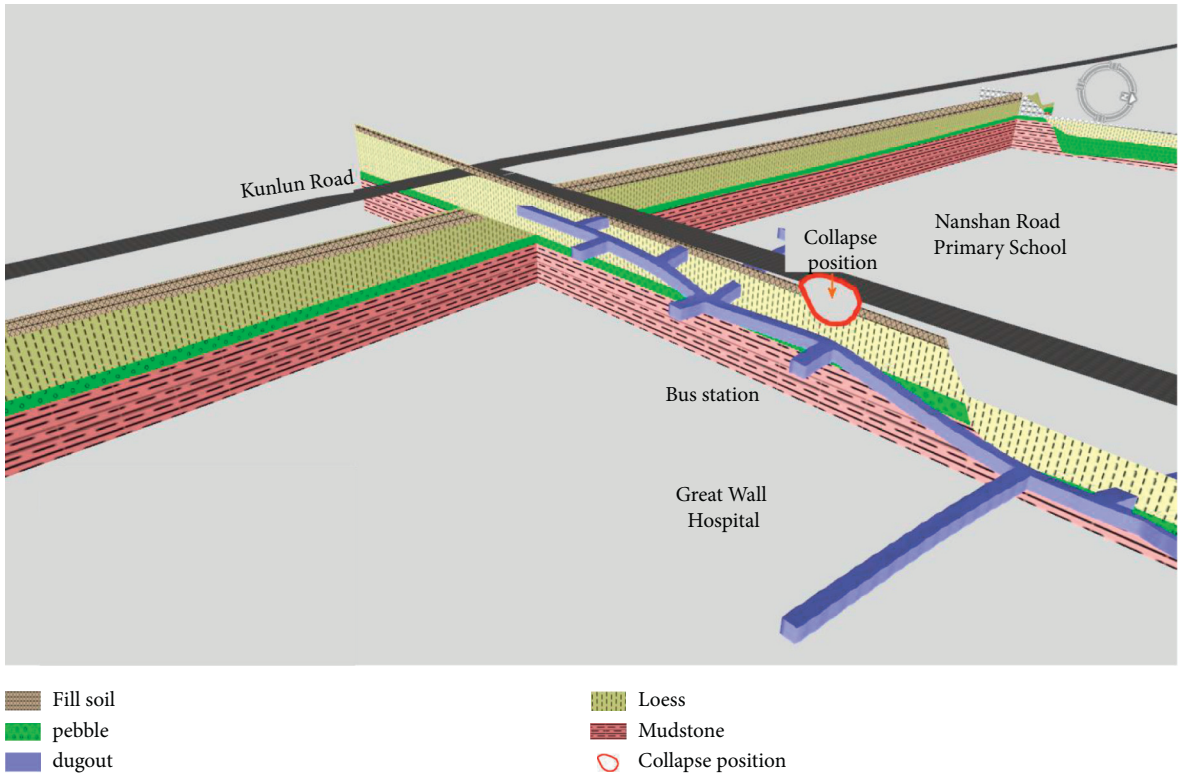

Figure 4: 3D geological structure model of collapse location.

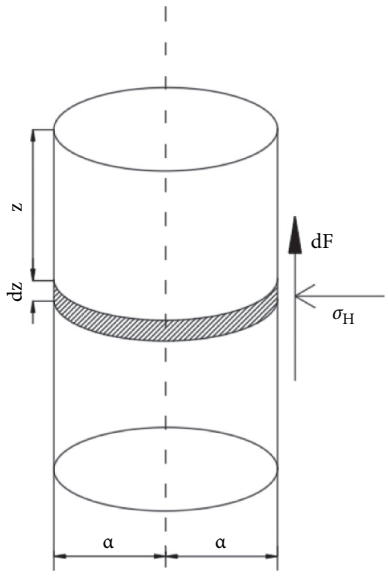

Figure 5: Calculation model of collapse balance method.

exceeds the ultimate bearing capacity of subgrade, the instantaneous collapse may occur.

3.2.2. Basic Geological Conditions. The geotechnical experiment is carried out on the soil samples obtained from the site, as shown in Figure 6. The physical and mechanical properties of collapsible loess-like soil and noncollapsible loess-like soil are mainly studied. The main physical and mechanical properties are shown in Tables 1 and 2.

Due to the different thickness and compaction degree of the fill under the asphalt concrete cover, there is a certain degree of uneven settlement. The collapsible loess soil is the main stratum in the collapse area, with loose structure, vertical joints, macropores, and strong water sensitivity. The loess soil is collapsible, with medium to strong collapsibility, and the collapsibility grade is grade II to grade III. It is easy to dissolve the soluble salt when it is wet with water, and the particulate matter is easy to lose and the strength is reduced. This kind of stratum is the basic geological condition of road collapse.

3.2.3. Space Condition. According to the field investigation, about 400 cubic meters of water poured into the collapse pit after the underground water supply pipeline was cut off and the valve was closed. In addition, according to the geometry and size of the collapse pit, it is estimated that the loss of loess-like soil is about

$$3.14 \times 4.52 \times 9 = 572m^3. \quad (5)$$

The total is 972 cubic meters. In addition, the total volume of water and soil mixture lost by previous leakage is more than 1000 cubic meters.

The cave body is filled with collapsing loess-like soil and gravel, and the bottom of the cave is silted. The underlying underground air raid shelter is a precast arch structure with rubble wall. Figure 7 shows the whole picture of the air raid

Figure 6: Selection of field soil samples.

Table 1: Statistics of physical and mechanical properties of collapsible loess (standard value).

Natural water content	14.44%	Compression coefficient	0.34 MPa^{-1}
Density	1.56 g/cm^3	Compression modulus	8.20 MPa
Specific gravity	2.71	Cohesion	15.098 MPa
Natural void ratio	1.017	Internal friction angle	19.5°
Saturation	39.18%	Collapsibility coefficient	0.069
Liquid limit	24.52%	Self-collapsibility coefficient	0.008
Plastic limit	16.11%	Standard penetration value	6.7
Plasticity index	8.44	Liquid index	−0.19

Table 2: Statistics of physical and mechanical properties of noncollapsible loess (standard value).

Natural water content	21.59%	Compression coefficient	0.39 MPa^{-1}
Density	1.82 g/cm^3	Compression modulus	11.75 MPa
Specific gravity	2.70	Cohesion	25.202 MPa
Natural void ratio	0.903	Internal friction angle	35.2°
Saturation	69.74%	Collapsibility coefficient	0.008
Liquid limit	24.78%	Self-collapsibility coefficient	0.008
Plastic limit	16.15%	Standard penetration value	6.8
Plasticity index	8.87	Liquid index	0.68

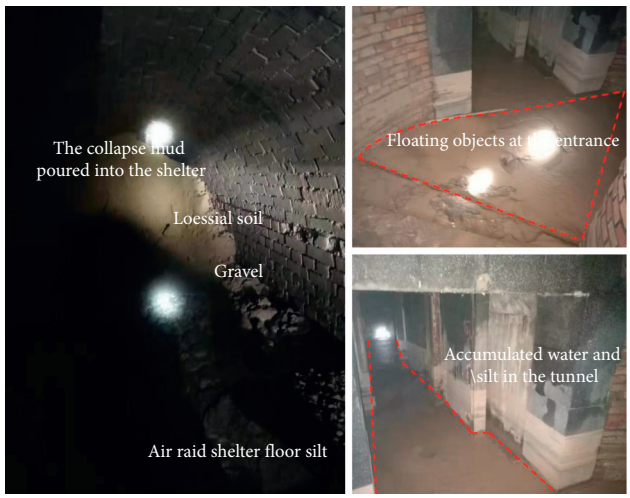

Figure 7: Full view of air raid shelter below after collapse.

shelter after collapse. The water depth is about 1.3 m and the silt thickness is about 0.5 m.

The seepage of the top plate of the air raid shelter reduces the bearing capacity of the subgrade and provides the migration channel and storage space for the water and soil loss of the pavement before and after the collapse. The air raid shelter provided space conditions for the road collapse.

3.2.4. Leading Factor. Due to the leakage of underground water supply pipe, the collapsible loess-like soil is eroded and dissolved, the underground soil structure is destroyed, and the soil particles are lost to the air raid shelter with water and gradually develop into underground cavity body and expand to the surface, resulting in the basic suspension of the pavement and the formation of "asphalt concrete bridge," resulting in the lack of subgrade bearing capacity. The pavement is gradually damaged under the long-term repeated action of the past vehicle load, especially the sudden failure under the impact load of the large vehicle brake, which eventually leads to the bus falling into the collapse pit. Water is the main factor to form voids and cause pavement collapse.

Combined with the analysis of the above factors, it can be seen that the cause of the ground collapse accident in Xining City is that the soil under the subgrade is eroded, dissolved, and washed by the leakage of underground water supply pipe, and the soil is lost into the underground air raid shelter

with water, resulting in the formation of large-scale cavity under the collapsed pavement, and the subgrade bearing capacity is insufficient when the bus stops, causing buses and people to fall into the collapse pit.

3.3. Formation Process and Mechanism Analysis of Collapse. Combined with the above data analysis, it can be seen that, before the collapse accident, the underground hidden cavity should have been formed. After the bus stops at the station, due to the insufficient bearing capacity of the surface asphalt concrete thin layer subgrade, the vehicles and personnel are trapped in the collapse pit. In order to explore the deformation and failure law of collapsible and noncollapsible loess under the effect of pipeline leakage, particle flow (PFC) was used to model the stratum. The Fluent module in ANASYS was used to calculate the groundwater flow field after pipeline leakage, and the flow field was imported into PFC for joint calculation.

3.3.1. The Establishment of the Model. According to the actual situation of the site, the mode of "subgrade and pavement + collapsible loess + noncollapsible loess + underground air raid shelter + pebble" is adopted, as shown in Figure 8. The model size is 30 m × 1 m × 20 m (length × width × height). According to the linear contact model from top to bottom, the subgrade and pavement with height of 1.5 m, collapsible loess layer with height of 8.8 m, noncollapsible loess layer with height of 3.6 m, and pebble layer with height of 4.8 m are generated, respectively. Combined with the statistical table of physical and mechanical properties, different mechanical parameters were given to all particles in the model to exert gravity and reach equilibrium state. If the model is generated according to the actual diameter of soil particles, the number of them is far more than 100 million. In this case, it is impossible to calculate by computer. Therefore, the diameter of soil particles is expanded to 0.1 m.

The diameter of the simulated water supply pipe is 0.5 m, and the upper edge of the pipe is 1.5 m below the ground. The air raid shelter and the pipe need to be simulated with Rhino 6.0 and imported into PFC as a wall unit. The vault of the air raid shelter is 11.6 m deep, 2.5 m high, and 1.5 m wide. The seepage crack on the air raid shelter is assumed to be a square hole, which is located on the vault of the air raid shelter.

Fluent was used to calculate the flow field and porous medium model was used to simulate the flow field. The viscous resistance coefficient of soil was set to 6.8 × 109. Because of the uncertainty of the leakage location of the water supply pipe, the surface of the water supply pipe is selected as the inlet of the flow field, the velocity is set at 4 m/s, the surface of the air raid shelter is set as the outlet boundary, and the other boundaries are set as impermeable boundaries. The obtained flow field is shown in Figure 9. The flow velocity between the water supply pipe and the air raid shelter is larger than that in other areas, which is in line with the hydrodynamic properties.

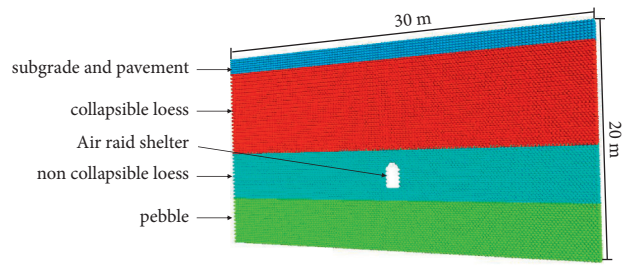

Figure 8: Soil model.

3.3.2. Analysis of Calculation Results. The flow field is introduced into the soil model, and PFC is used for joint calculation. The crack size on the air raid shelter model is 0.75 times of the particle size. Figure 10 shows the whole process of underground cavity formation. In the early stage of leakage, the mixture of soil and water mainly flows through the air raid shelter into the air raid shelter, so the larger disturbance area of soil is concentrated near the vault of the air raid shelter. With the progress of the calculation, the soil disturbance area continues to develop horizontally and vertically and finally extends to the ground below, forming "asphalt concrete bridge." In this case, if the pavement is repeatedly affected by external loads, and no timely discovery and remedial measures are taken, it will lead to the deformation of the pavement until sudden collapse, which poses a threat to the safety of human life and property.

In order to describe the ground settlement caused by leakage, the stratum deformation under different calculation steps is described, as shown in the figure. The calculation results show that the plastic zone tends to develop around with the progress of calculation (Figure 11). When the calculation steps are 100000, the deformation range of stratum is about 16 m, and the height of cavity is about 9 m. The maximum settlement occurred above the air raid shelter, and a more obvious underground cavity has been formed.

3.3.3. Void Formation Mechanism Analysis. Urban road collapse is sudden, but the formation of underground cavity has experienced the development process of water supply pipe leakage, underground soil penetration and cavity formation, critical state of collapse area, road collapse, and so on, as shown in Figure 12.

3.3.4. Leakage of Water Supply Pipe. Because the loess in this area has weak corrosivity to the concrete structure and steel structure, when the water supply pipe is buried underground for a long time and lacks effective maintenance for a long time, the corrosion leads to the leakage of the pipe wall, which makes the water flow into the lower soil layer, and the water leakage accelerates with time. Under the action of water, the soil below gradually reaches saturation state and deforms to a certain extent. At this stage, the hidden water is high, and the outflow of water in the pipe is small in a short time, which is not easy to attract the attention of the relevant departments.

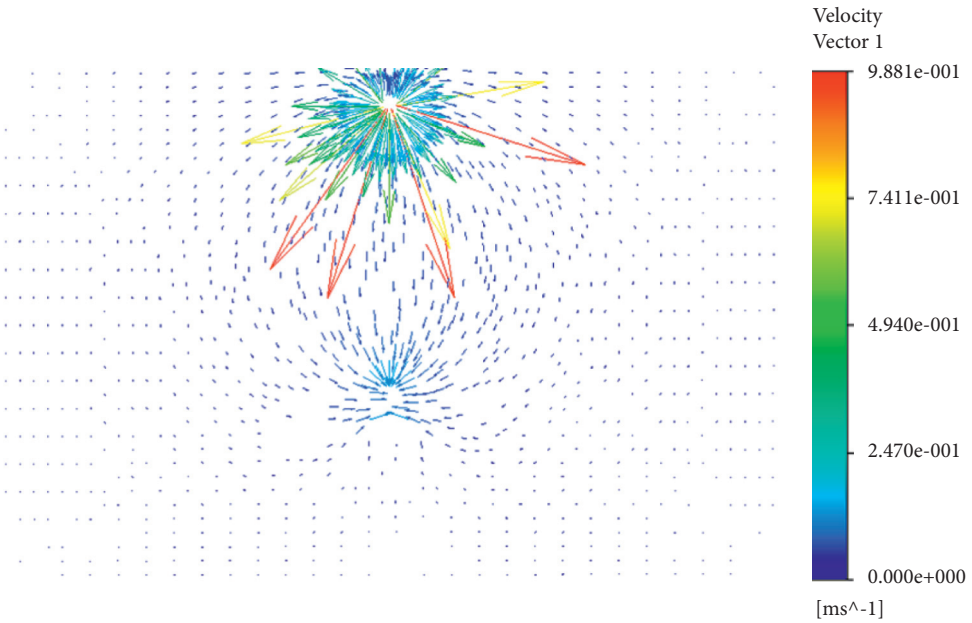

Figure 9: Flow field vector diagram.

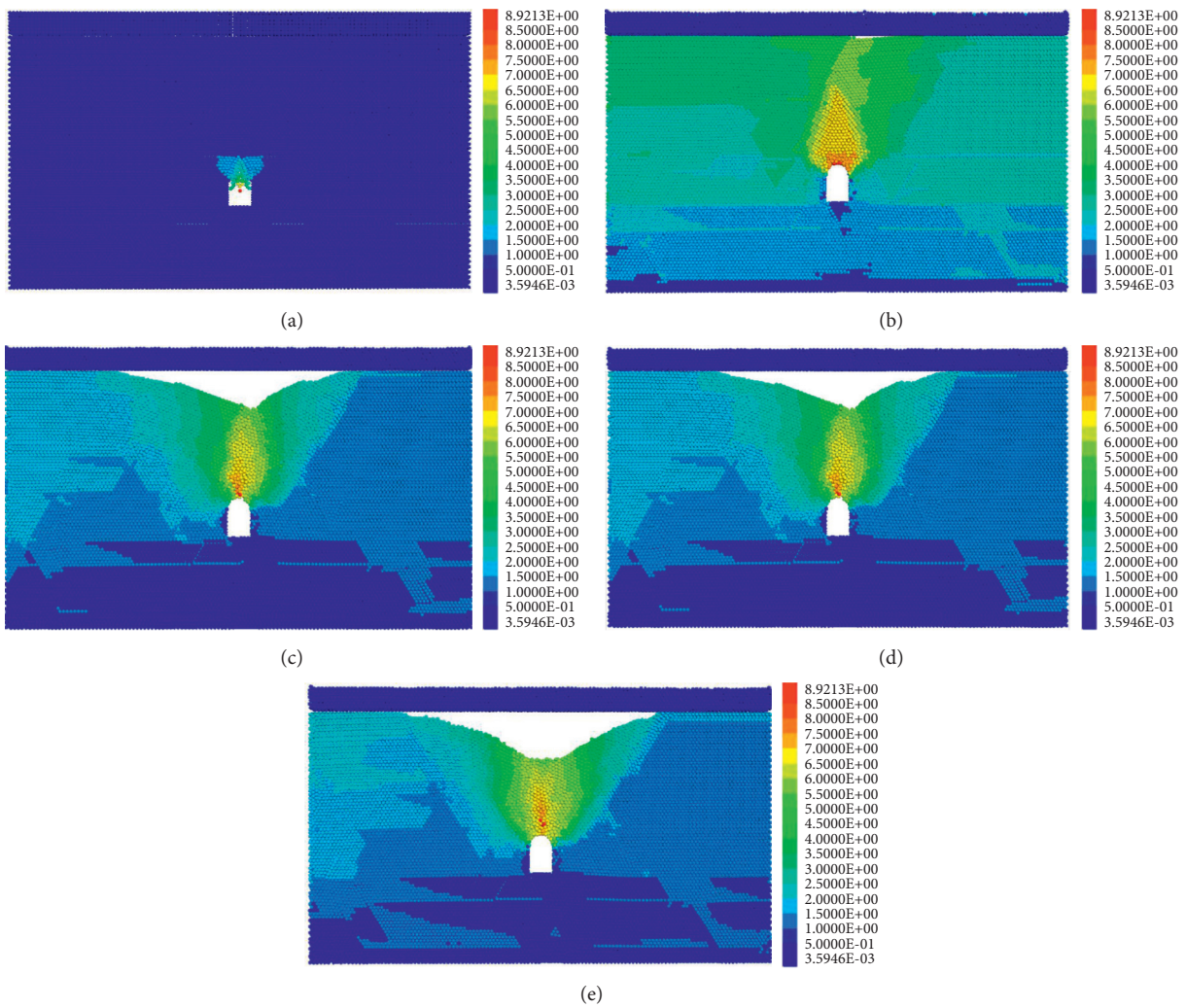

Figure 10: Displacement cloud map of each soil layer in the stratum. (a) Run 5000 steps. (b) Run 10000 steps. (c) Run 30000 steps. (d) Run 80000 steps. (e) Run 100000 steps.

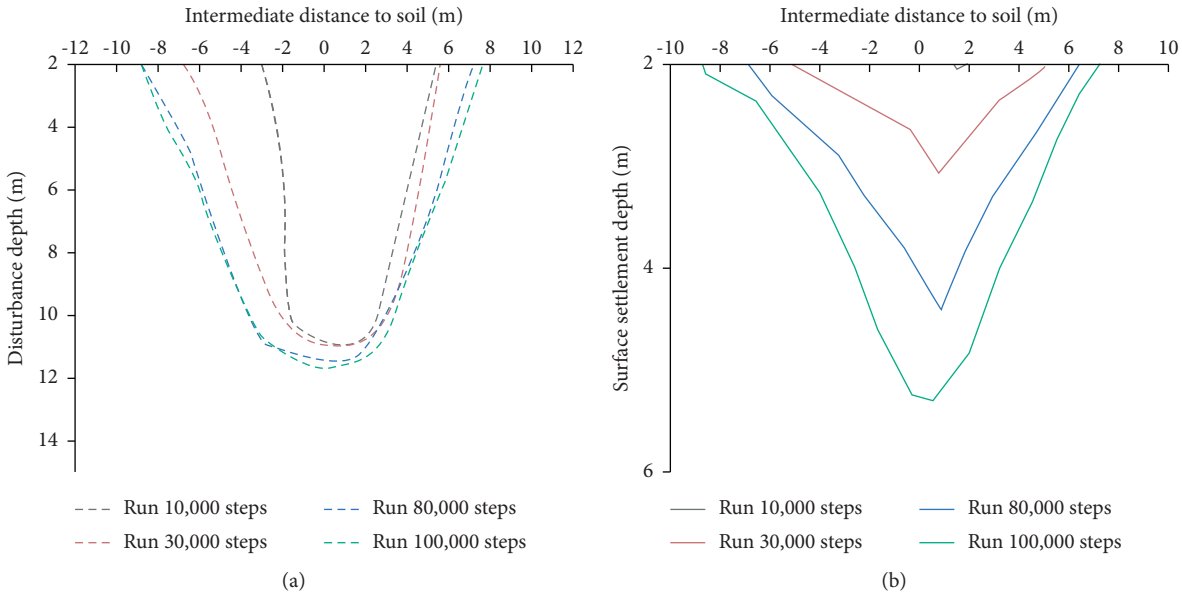

Figure 11: Envelope of disturbance zone and surface settlement curve. (a) Envelope of disturbed region. (b) Surface subsidence curve.

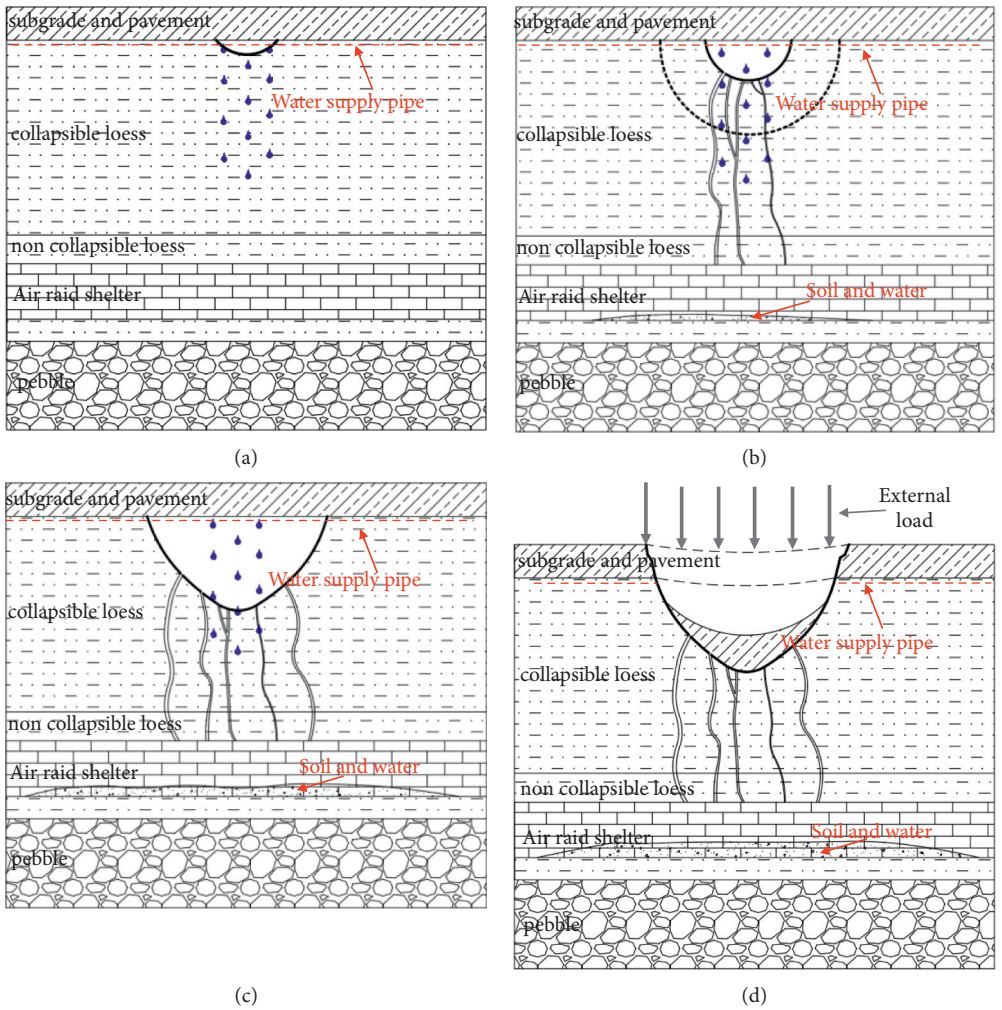

Figure 12: Formation and collapse process of underground cavity. (a) Leakage. (b) Development. (c) Through. (d) Collapse.

3.3.5. Penetration of Underground Soil and Formation of Cavities. On the one hand, the long-term water leakage will accelerate the corrosion of the water supply pipe, thus speeding up the water leakage in the water supply pipe. On the other hand, the fine particles in the soil are taken away and flow into the air raid shelter under the action of water, forming "underground passages" at the initial stage, which connect and expand with each other, eventually leading to the formation of underground cavities. At the same time, because of the collapsibility of the loess in this area, the collapsibility effect will occur when it meets with water, which will also cause the uneven settlement of the soil at the leakage and accelerate the formation of underground cavities.

3.3.6. Critical State of Collapse Zone. With the formation, transfixion, and expansion of underground cavity, coarse particles in soil exist in the form of skeleton, and soil structure also changes to some extent. However, soil can still maintain a critical stable state through its skeleton effect and stress adjustment. When this stable state is disturbed by external factors, it is easy to lose stability.

3.3.7. Road Collapse. The collapse area is in a critical state, forming "Asphalt Pavement Bridge." When the bus and other external loads act on the pavement, the external load reaches and exceeds the ultimate bearing capacity of the subgrade, and the pavement collapses suddenly.

4. Conclusions and Suggestions

(1) The accidental factor causing the ground collapse accident is the water from the water supply pipe and once again confirmed that the urban ground collapse disaster has the characteristics of high concealment and sudden and high risk.

(2) Numerical simulation analysis shows that the final stratum deformation range is about 16 m, and the height of the cavity formed at this time is about 9 m. The maximum settlement occurred above the air raid shelter, and a more obvious underground cavity has been formed.

(3) The process of ground collapse includes four stages: water supply pipe leakage, underground cavity formation, critical state of ground collapse, and ground collapse.

(4) It is suggested that Xining City should adopt various means as soon as possible to carry out exploration and safety risk assessment on various underground pipe networks and air raid shelters of urban roads and do a good job in the daily operation, maintenance, management, monitoring, and early warning of underground pipe networks to avoid similar incidents in Xining area. At the same time, it should also sound an alarm to the whole country and strengthen the planning, development, and utilization, comprehensive management, and underground disease prevention and control of urban underground space in the whole country.

Data Availability

The data are available and explained in this article; readers can access the data supporting the conclusions of this study.

Conflicts of Interest

The authors declare no conflicts of interest.

Acknowledgments

The authors gratefully acknowledge the funding provided by National Key R&D Program of China (2019YFC1509600).

References

[1] S. Yi, "Distribution characteristics of ground collapse and its countermeasures Guangdong Province[J]," *Chinese Journal of Geological Hazard and Control*, vol. 2007, no. 02, pp. 127–131, 2007.

[2] M. Yan, K. Yin, and M. Lei, "Probabilistic analysis ON karst collapse induced BY water ta fluctuation [j]," *Carsologica Sinica*, vol. 2006, no. 03, pp. 239–241+245, 2006.

[3] Y. Shengquan, "Formation causes of Karst collapse and its preventing measures in Guizhou Province [J]," *Science of Soil and Water Conservation*, vol. 2007, no. 06, pp. 38–42, 2007.

[4] G. Chen, Y. Wang, and W. Zhou, "The formation research of karst caves in Wushan copper mine JiangXi province [J]," *China Water Transport(Academic Version)*, vol. 2007, no. 10, pp. 95–97, 2007.

[5] Y. Zhao and Y. Xie, "Discussion on the cause and mechanism of Goaf collapse in xinzhou mine, guangxi [J]," *Chinese Journal of Geological Hazard and Control*, vol. 1997, no. S1, pp. 204–211, 1997.

[6] H. Huang, Y. Wu, G. Lv, and L. liang, "Cause analysis and prevention methods of Goaf collapse in datong coal mine [J]," *China Energy and Environmental Protection*, vol. 2009, no. 01, pp. 26-27+40, 2009.

[7] W. Ji and X. Yin, "Cause mechanism and prevention strategy of mining collapse disaster [J]," *Chinese Journal of Geological Hazard and Control*, vol. 1998, no. 03, pp. 60–65, 1998.

[8] J. Sun, "Collapsibility of loess and its relationship with humidity [J]," *Hydrogeology & Engineering Geology*, vol. 1957, no. 11, pp. 18–21, 1957.

[9] Z. Zhang, "Study on Microstructure of loess like soil in China [J]," *Acta Geologica Sinica*, vol. 1964, no. 03, pp. 357–369+375, 1964.

[10] G. Gao, "Discussion on microstructure and collapsibility mechanism of lanzhou loess [J]," *Journal of Lanzhou University*, vol. 1979, no. 02, pp. 123–134, 1979.

[11] G. Gao, "Relationship between microstructure, geography and geological environment of loess in China [J]," *Acta Geologica Sinica*, vol. 1984, no. 03, pp. 265–280, 1984, 272+279-.

[12] C. Hou, M. Dong, and H. Fu, "Research on genesis and mechanics of land collapse in incompact soil [J]," *Journal of Hefei University of Technology*, vol. 36, no. 01, pp. 63–67, 2013.

[13] C. Gu, C. Yuan, and R. Qing, "Subsidence causation and countermeasure analysis of urban roads in beijing [J]," *Urban*

roads and bridges and flood control, vol. 2011, no. 08, pp. 250–252+9, 2011.

[14] Y. Jiang, G. Yang, Z. Huang, Y. Qiao, and Y. Zhang, "Ground treatment of high-rise buildings in complex karst region,[J]," *Rock and Siol Mechanics*, vol. 36, no. S1, pp. 430–438, 2015.

[15] Y. Yechieli, M. Abelson, and G. Baer, "Sinkhole formation and subsidence along the Dead Sea coast, Israel," *Hydrogeology Journal*, vol. 24, no. 3, pp. 1–12, 2015.

[16] Z. Cheng, "Effects of irrigation on land subsidence and ecological environment in Loess Plateau area of central Gansu Province[J]," *Journal of Desert Reseaech*, vol. 2002, no. 02, pp. 76–80, 2002.

[17] C. xing and S. Peng, "Numerical simulation of collapse caused by groundwater level decline in Karst Area[J]," *Earth and Environment*, vol. 33, no. s1, pp. 119–123, 2005.

[18] Z. Wan, S. Qin, Z. Li, and H. Qian, "Formation mechanism and initial condition of soil cavity [J]," *Journal of rock mechanics and Engineering*, vol. 22, no. 8, pp. 1377–1382, 2003.

[19] A. N. Palmer and M. V. Palmer, "Hydraulic processes in the orgin of tiankengs[J]," *Carsologica Sinica*, vol. 25, no. s1, pp. 71–78, 2006.

[20] G. Selleri, P. Sanso, and N. Walsh, "The karst of Salento region (apulia, southern Italy): constraints for management[J]," *Acta Carsologica*, vol. 32, no. 1, 2016.

[21] Z.-h. Ouyang, "The role of potential soil cavity on ground subsidence and collapse in coal mining area," *Journal of Coal Science and Engineering*, vol. 16, no. 3, pp. 240–245, 2010.

[22] F. Cao, "Causes and prevention of karst ground collapse in Zaozhuang area [J]," *Carsologica Sinica*, vol. 1998, no. 2, pp. 104–110, 1998.

[23] T. Peng, S. Ge, and W. Wu, "Remeadiations of foundation collapse in the soil cavity area of karst [J]," *Hydrogeology & Engineering Geology*, vol. 28, no. 3, pp. 55–57, 2001.

[24] Z. Gao, "Study on the mechanism and cause mode of the karst collapse——taking tai'an-laiwu for example [J]," *Strategic Study of CAE*, vol. 2008, no. 04, pp. 38–43, 2008.

[25] Z. Hu, "Formation mechanism and prevention of surface subsidence in East mining area of Tangshan City [J]," *Hydrogeology & Engineering Geology*, vol. 1991, no. 4, pp. 34–36, 1991.

[26] X. Li, K. Peng, J. Peng, and D. Hou, "Experimental investigation of cyclic wetting-drying effect on mechanical behavior of a medium-grained sandstone," *Engineering Geology*, vol. 293, Article ID 106335, 2021.

[27] X. Li, K. Peng, J. Peng, and H. Xu, "Effect of cyclic wetting-drying treatment on strength and failure behavior of two quartz-rich sandstones under direct shear," *Rock Mechanics and Rock Engineering*, vol. 54, no. 11, pp. 5953–5960, 2021.

[28] S. TÜRkmen and N. ÖZgÜZel, "Grouting a tunnel cave-in from the surface: a case study on Kurtkulağı irrigation tunnel, Turkey," *Tunnelling & Underground Space Technology Incorporating Trenchless Technology Research*, vol. 18, no. 4, pp. 365–375, 2003.

[29] Y. Hou, D. Zhang, and P. Li, "Analysis and control measures of safety accidents in beijing subway construction [J]," *Journal of Beijing Jiaotong University*, vol. 2009, no. 3, pp. 52–59, 2009.

[30] H. Ma, X. Wang, W. You, and P. Che, "Cause analysis on the ground collapses during the launching period of a Metro shield [J]," *Modern Tunnelling Technology*, vol. 47, no. 03, pp. 76–80, 2010.

[31] C. Zhu, Z. Yan, Y. Lin, F. Xiong, and Z. Tao, "Design and application of a monitoring system for a deep railway foundation pit project," *IEEE Access*, vol. 7, pp. 107591–107601, 2019.

[32] C. Zhu, K. Zhang, H. Cai et al., "Combined application of optical fibers and CRLD bolts to monitor deformation of a pit-in-pit foundation," *Advances in Civil Engineering*, vol. 2019, no. 1, pp. 1–16, 2019.

Hindawi
Advances in Materials Science and Engineering
Volume 2022, Article ID 6077187, 15 pages
https://doi.org/10.1155/2022/6077187

Research Article

Fractal Study on the Failure Evolution of Concrete Material with Single Flaw Based on DIP Technique

Lulin Zheng,[1,3] **Hao Liu**,[1,2] **Yujun Zuo**,[1,2] **Quanping Zhang**,[4] **Wei Lin**,[5] **Qing Qiu**,[1] **Xiaorong Liu**,[1] **and Ziqi Liu**[1]

[1]*College of Mining, Guizhou University, Guiyang, Guizhou 550025, China*
[2]*College of Resource and Environmental Engineering, Guizhou University, Guiyang, Guizhou 550025, China*
[3]*School of Architecture and Civil Engineering, Xiamen University, Xiamen, Fujian 361005, China*
[4]*School of Earth Sciences and Resources, China University of Geosciences (Beijing), Beijing 100083, China*
[5]*Faculty of Engineering, China University of Geosciences, Wuhan, Hubei 430074, China*

Correspondence should be addressed to Hao Liu; 907529196@qq.com

Received 22 December 2021; Accepted 17 January 2022; Published 4 February 2022

Academic Editor: Ren Fuqiang

Copyright © 2022 Lulin Zheng et al. This is an open access article distributed under the Creative Commons Attribution License, which permits unrestricted use, distribution, and reproduction in any medium, provided the original work is properly cited.

Crack inclination and material heterogeneity have important effects on the meso-mechanical mechanism and macroscopic mechanical behavior of rock-like materials. In order to study the failure characteristics of shotcrete body during the process of using shotcrete bolt mesh support in the deep fractured rock mass of Lannigou Gold Mine, this paper combined the Digital Image Processing Technique (DIP) and RFPA2D (Rock Failure Process Analysis System) to establish a real meso-structure numerical model of concrete with different inclination angle cracks, simulating its crack propagation law and failure process, and studied the influence of crack geometry distribution and meso-heterogeneity on the effect of concrete structure. The findings reveal that the crack inclination angle has a substantial impact on concrete materials' compressive strength and elastic modulus, and both of them all show a nonlinear increase with the increase of crack angle; Because of the inhomogeneity of the materials, the inclination and propagation pathways of wing cracks are random, and the aggregate inhibits crack initiation and propagation. The wing crack's initiation position moves closer to the tip as the crack inclination angle increases, and the length gets shorter; Acoustic emission(AE) evolution characteristics are similar in samples with varying dip angles. In the early stages of loading, the AE energy is minimal, and increases rapidly when approaching the peak stress. The fractal dimension was used to describe the damage evolution process inside the material, and a damage variable index (ω) based on the fractal theory was proposed. The more the ω, the greater the material's degree of degradation. The proposed index provided a new method for quantitative study of the damage evolution characteristics of rock-like materials. It has guiding significance for the research on the stability of wet shotcrete in the deep fractured rock mass of Lannigou Gold Mine.

1. Introduction

The Lannigou Gold Mine is located in Zhenfeng county, the Southwest of Guizhou province. The underground mining utilizes ramp development and layered upward cemented fill mining. In order to ensure the safety of mining operations, shotcrete anchor nets are used to reinforce the surrounding rock in almost all roadways in the mine. In particular, wet shotcrete is the most important process to reinforce the roadways, which is particularly effective in the weathered rock mass of the mine. As the mining depth increases, the deep ground stress increases. Meanwhile the surrounding rock is fragmented and the stability is poor due to the combined influence of high ground stress and geological structure. As a result, investigating the fracture characteristics and damage development process of wet shotcrete can provide some theoretical support for the concrete support of the Lannigou gold mine and other comparable mines.

As an artificial rock-like material, concrete contains different types and structures of media. They have different

physical and mechanical properties, containing a large number of defects, and their responses to external forces are also very different[1–3]. The initiation and propagation behavior of cracks in rock-like materials is closely related to their internal structures[4–6], single crack angle and material heterogeneity jointly determine the macroscopic fracture characteristics and damage evolution characteristics of material. As a result, studying the fracture process and damage evolution characteristics of rock-like materials while taking into account the crack inclination angle and material non-uniformity, as well as revealing the mesoscopic damage evolution mechanism and macroscopic nonlinear mechanical behavior, is of great theoretical importance.

Scholars in the China and around the world have never stopped studying the initiation and propagation behavior of rock cracks and rock-like materials cracks around the crack inclination angle. Nolen-Hoeksema et al. conducted compression tests on marble and discovered that when the prefabricated crack is oblique, the initiation and propagation of the tip secondary cracks are asymmetrical[7]. Yang et al. study the influence of crack angle on the initiation behavior and compressive strength of sandstone through rock mechanics experiments[8]. Park et al. conducted rock mechanics experiments on rocks with cracks, and the study found that as the crack inclination angle increased, so did the initiation stress of the wing crack[9]. Manouchehrian et al. investigated the role of crack inclination in the initiation and propagation of rock cracks using numerical simulation methods[10]. Through numerical simulation, Zhang et al. investigated the impact of fracture angle on the initiation process of rock-like materials, finding that the crack inclination angle has a significant impact on crack initiation and propagation[11]. Liu et al. used a combination of physical tests and numerical simulations to investigate how crack inclination affects crack propagation and stress field evolution in rock-like materials[12]. Xu et al. used physical experiments to investigate the effect of fracture angle on the crack initiation behavior of rock-like materials under uniaxial compression, finding that the uniaxial compressive strength increased as the crack angle rose[13]. However, because the macroscopic damage of materials is closely related to the development and aggregation of internal micro-cracks, the evolution of material damage has aroused widespread concern of many scholars. Taylor et al. used the self-consistent approach to create a link between crack density and rock damage, and evaluated the completeness of fractures in the rock to reflect the damage degree[14]. Ahrens et al. linked the development of cracks in the medium with the change of the p-wave velocity, and used p-wave velocity to characterize the distribution characteristics of micro-cracks inside the rock mass, so as to evaluate the damage of surrounding rock according to the change of p-wave velocity[15]. Xie developed fractal-damage mechanics by applying fractal geometry theory to the analysis of rock fractures, opening up a new technique to examine rock damage quantitatively[16]. Gao has studied the mechanical behavior of coal and rock under various mining circumstances, from laboratory experiments to field testing[17]. Based on the fractal theory, Liu et al. compiled an algorithm pf rock mesoscale fracture box dimension based on digital images, proposed a calculation method of rock mesoscale fracture dimension, and carried out quantitative characterization of the failure mode and damage degree of jointed sandstone [4, 18].

The above research results are of great significance for revealing the crack propagation mechanism and damage evolution characteristics of materials with flaw at macroscale, but the macroscopic mechanical behavior of materials is determined by the heterogeneity and mesoscale behavior of materials. Therefore, the study on the fracture process and damage evolution characteristics of the material on the basis of considering the material inhomogeneity and flaw inclination will help reveal its crack propagation mechanism and macroscopic nonlinear mechanical behavior.

The true mesoscopic structure of varied angle cracks in concrete numerical model is established in this research using the Rock Failure Process Analysis System (RFPA2D) and Digital Image Processing technology, the influence of crack geometric distribution and meso-uniformity on the concrete structure effect is studied, and the fractal theory is applied to describe the damage evolution process of material inside. The damage variable index, based on fractal theory, is offered as a new tool for studying the damage evolution of rock-like materials quantitatively.

2. Finite element method for rock-like material failure process

2.1. Digital image representation of meso-structure. The main components of concrete are aggregate, cement mortar, and accompanied by a small amount of primary holes (Figure 1(a)). The three components have different colors, among which gray is mostly mortar, white is aggregate, and the rest are holes. Figure 1(c) is a CT slice obtained by scanning with high-resolution industrial CT (Figure 1(b)) at Tianjin Sanying Company, and the image pixels are 200x200 pixels, the actual size is 100mmx100mm. It is difficult to build a relationship between the unified algorithm and the finite element approach because the medium in the original image (Figure 1(c)) is dark or bright in color. Therefore, image processing is required to identify the mesoscopic medium inside the concrete.

Through the differences of grayscale and color, digital image processing technology distinguishes the geometric shape and spatial distribution of the material's meso-component. The technology is utilized to establish the segmentation threshold for distinct media in the rock based on color and brightness differences. The value divides the distribution of each medium, and the non-uniformity characterization image of the material can be obtained [5, 19].The Figure 1(c) is a 24-bit BMP bitmap, whose color change is not visible. As a result, multi-threshold segmentation is performed by examining the variation rule of the brightness I value in HIS (Hue refers to chromaticity, S refers to Saturation, and I refers to brightness) image processing color space[4, 18]. The changing curve of the value of I on the AA' scan line in Figure 1(c) is shown in Figure 1(d). The material medium passed by the scan line is compared with

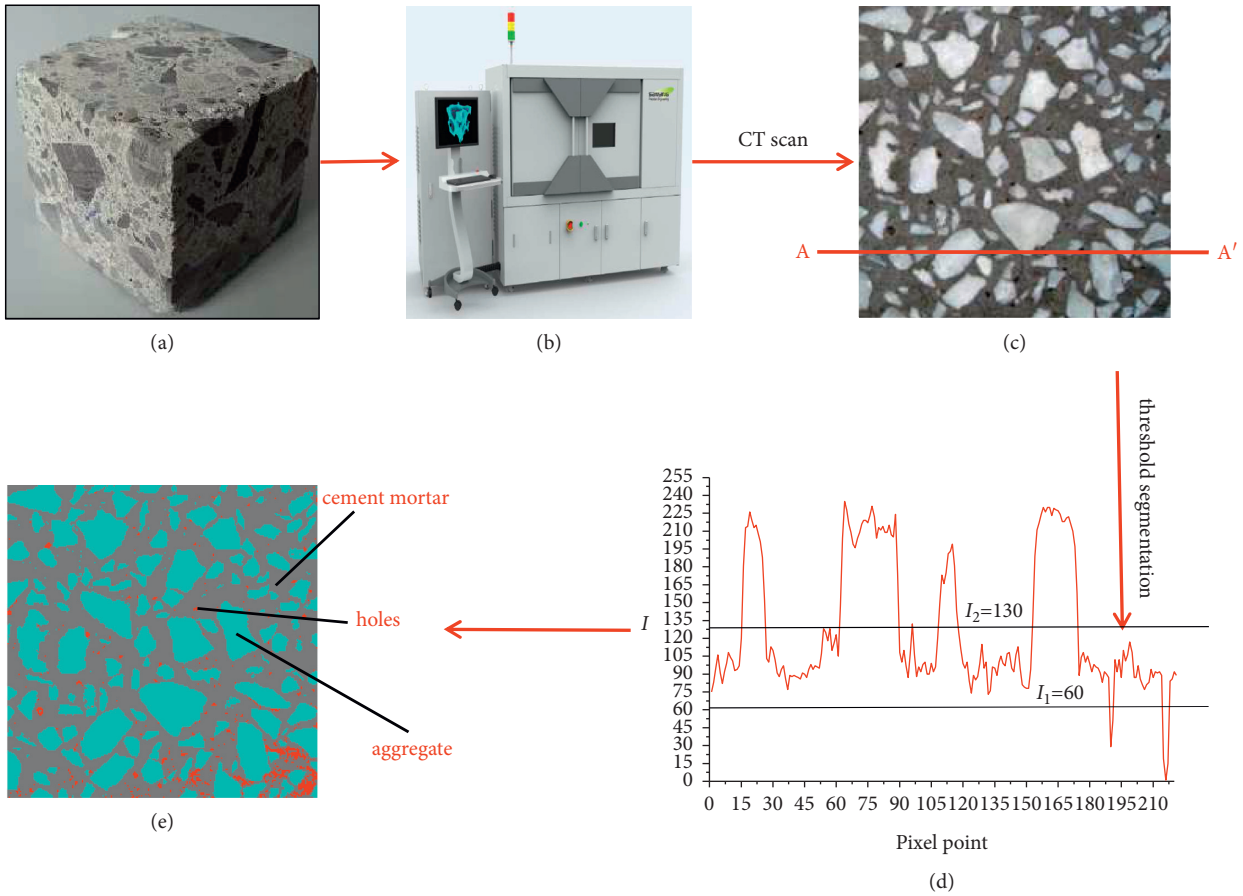

Figure 1: The process of concrete digital image characterization.

the change of the curve. Through repeated tests and adjustments in DIPS software, the ideal segmentation threshold is finally obtained, which is 60 and 130 respectively, and the characterization image can accurately reflect each mesoscopic component in Figure 1(c). Since the two-dimensional CT slices are grayscale images, the value range of the matrix elements of the grayscale image is usually [0,255], and 0~255 represents the range of color transition from pure black to pure white. Therefore, the I value is divided into three intervals: 0-60, 61-130, and 131-255. Each interval represents holes, mortar, and aggregates. That is, the internal mesoscopic medium of concrete is divided into 3 categories. Figure 1(e) is the meso-structure characterization image obtained after CT slice processing with DIPS software. Compared with Figure 1(c), the processed results basically reflect the real structure of concrete.

2.2. Meso-structure transformation and numerical modeling. The non-uniformity characterization of digital image processing technology must be constructed with a finite element mesh and then incorporated into the numerical model so that the influence of the material meso-structure may be considered in mechanical calculations and analyses. A digital image is a matrix of rectangular pixels, each of which is a small square with a certain width and height. As a result, each pixel in the finite element grid (Figure 2) can be considered a element, and the coordinates of its four corner points can be transformed into the appropriate actual position in vector space. The whole image can be converted into square finite element grid data and imported into RFPA2D to generate concrete numerical specimens. Detailed description of the conversion process and RFPA2D principle can be found in the literature[20, 21]. The material properties of each material component are then allocated to the represented colors, and the non-uniformity coefficients of different components are input into the numerical model to create a numerical model that considers the material's genuine mesoscopic structure.

Given the non-uniformity of the material, we assume that the mechanical characteristics (elastic modulus, strength, etc.) of matrix elements obey the Weibull distribution function in the numerical calculation[22]:

$$f(u) = \frac{m}{u_0}\left(\frac{u}{u_0}\right)^{m-1} \exp -\left(\frac{u}{u_0}\right)^{m}, \quad (1)$$

where, u is the physical property parameter (elastic modulus, strength, etc.) of the material medium element; the average of the basic physical property characteristics is u_0; m is the distribution function's property parameter that reflects the uniformity of the material medium; the smaller m, the more uneven the rock property. The statistical density of the physical attributes of the material constituents is denoted by

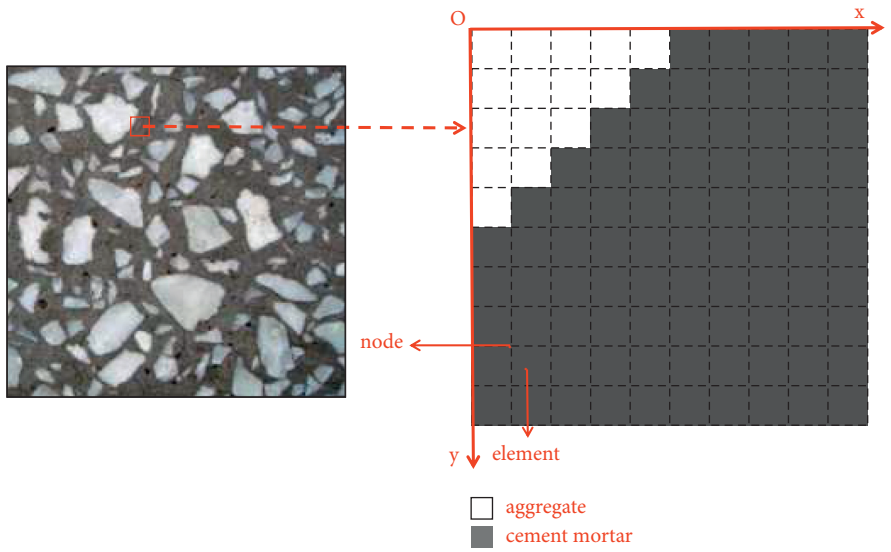

Figure 2: Concrete CT slice and finite element mesh transformation.

f(u). The non-uniformity of aggregate, mortar, and primary cavity was taken into account in the model, and the mechanical characteristics of the meso-element were assigned using the Monte-Carlo approach[23, 24].

Table 1 shows the material properties of the meso-medium within the concrete, and the specimens are mechanically loaded by uniaxial compression. Figure 3 is a schematic diagram of the force on the numerical model, the entire process is controlled by a continuous displacement loading method, with plane stress analysis used to simulate the test. The starting uniaxial compression displacement value is 0.001 mm, with a single step load increment of 0.002 mm, a pressure ratio of 10, and the specimen is loaded until it is destroyed. Considering the characteristics of concrete materials that are compressive and not tensile, this paper chooses the Mohr-Coulomb strength theory with tensile criterion[25] as the criterion for element failure. The numerical test was carried out in RFPA2D software[4, 5].

To investigate the impact of different inclination cracks on the mechanical properties of concrete materials, as well as the effect of microscopic non-uniformity caused by different crack geometrical distributions on the macroscopic failure of concrete, we prefabricated cracks with a length of 60mm and a width of 5mm in the middle of the sample, and anticlockwise every 15°to obtain a digital image, a total of 5 digital image were acquired at last (as shown in Figure 4). The prefabricated crack dip angles α are 15°, 30°, 45°, 60° and 75° respectively, where α is the prefabricated crack's included angle with respect to the horizontal direction. Furthermore, it is vital to ensure the same meso-structure of concrete specimens in order to analyze the fracture process and damage features of concrete with varying dip angles.

3. Results and discussion

3.1. Analysis of the influence of a single flaw on the mechanical properties of concrete. Figure 5 depicts the elastic modulus and internal primary stress distribution of concrete specimens when α=45°. The greater the brightness in the figure, the greater the stress value. Because of the variation in internal microstructure, the internal stress distribution of the specimen is uneven when compared to Figure 5(a). The stress concentration distribution at the tip of the prefabricated crack and the critical surface (weak surface) where the aggregate contacts the mortar is more significant. This demonstrates that the presence of cracks in concrete and material non-uniformity have a significant impact on stress distribution.

The compressive strength and elastic modulus of cracked concrete specimens with various inclination angles can be shown in Table 2. The elastic modulus and peak strength of various specimens are clearly anisotropic, as shown in Fig. 6, which increases non-linearly with the increase of the precrack inclination angle. The specimens' greatest strength is reached at α=75°, and the value is 143.84MPa; while the minimum value is 93.71MPa when α=15°. This is due to the prefabricated cracks with different inclination angles in the specimen and the different mechanical properties of different components in the material, which lead to different mechanical responses under the same level of loading conditions, resulting in uneven stress distribution. This conclusion is in line with the findings of Li et al. [26] (Figure 6), indicating that the numerical simulation results are trustworthy. As shown in Figures 6 and 7, different stress concentrations are caused by the difference in the internal microstructure of the cracked concrete at different inclination angles when the specimen is loaded, which induces damage and gradually breaks. The elastic modulus and compressive strength show a great difference, which caused by the different inclination angles of the cracks.

3.2. Analysis of crack propagation characteristics and meso-fracture evolution of specimens. Many researchers have looked at the start and propagation of the original fracture point and discovered that it may be split into three types:

Table 1: Concrete mesoscopic medium material parameters

Material	Elastic modulus/GPa	Poisson ratio	Compressive strength/MPa	Internal friction angle/(C°)
Aggregate	49.7	0.25	298.8	35
Cement mortar	24.8	0.18	149.6	30

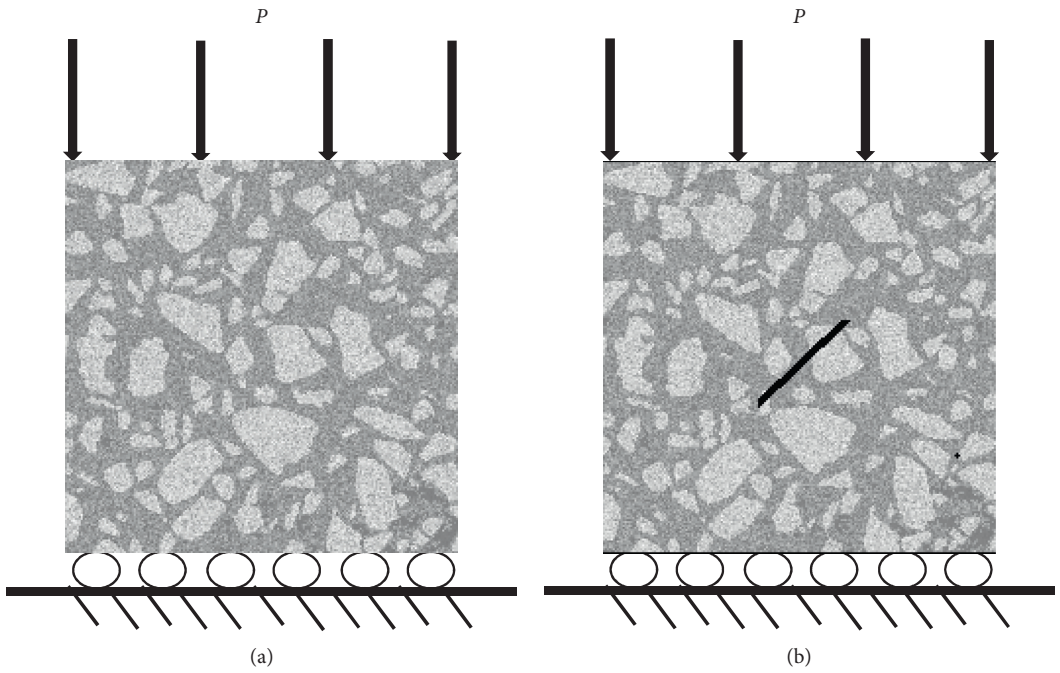

Figure 3: Schematic diagram of numerical model loading.

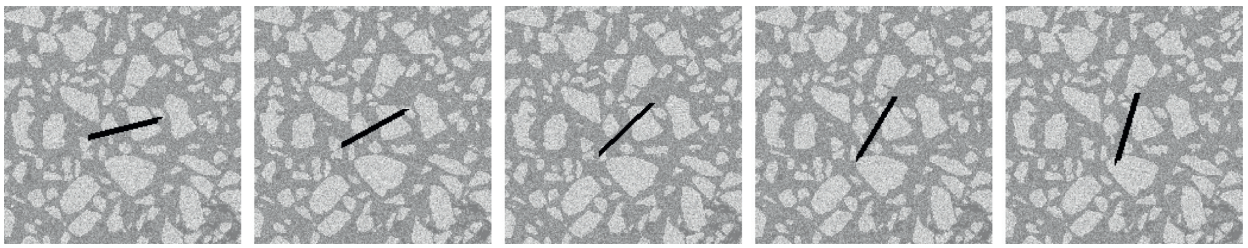

Figure 4: Digital images of concrete materials with different inclination angles flaw.

Wing Crack (WC), Secondary Coplanar Crack (SCC) and Secondary Inclined Crack (SIC)[27, 28]. Figure 7 shows the evolution of acoustic emission and elastic modulus during the failure process of concrete with different inclination angles. In the acoustic emission evolution diagram, yellow indicates tensile failure, red indicates compression-shear failure, and black indicates damaged elements.

As can be seen from the Figure 7, When α=15°, the wing crack initiates and propagates along a specific distance from the tip of the prepared fracture, and the wing crack at the lower end propagates along the weak surface. The tensile stress determines the initiation and progression of the wing crack, and a secondary oblique crack is generated on the weak side of the lower right corner of the specimen due to the dominant tensile stress. With the increase of stress, the wing crack near the prefabricated crack's tip continued to spread until it penetrated, resulting in the specimen's tensile split failure; When α=30°, the wing crack is perpendicular to the prepared crack's tip and expands slowly; when axial stress increases, the upper wing crack penetrates the aggregate, resulting in transgranular cracks, while the lower wing crack continued to expand along the weak surface. As a result of the large accumulation of tensile failure, on the weak surface of the lower right corner of the specimen, a macroscopic secondary oblique crack developed, eventually leading to the splitting failure of the specimen; When α=45°,

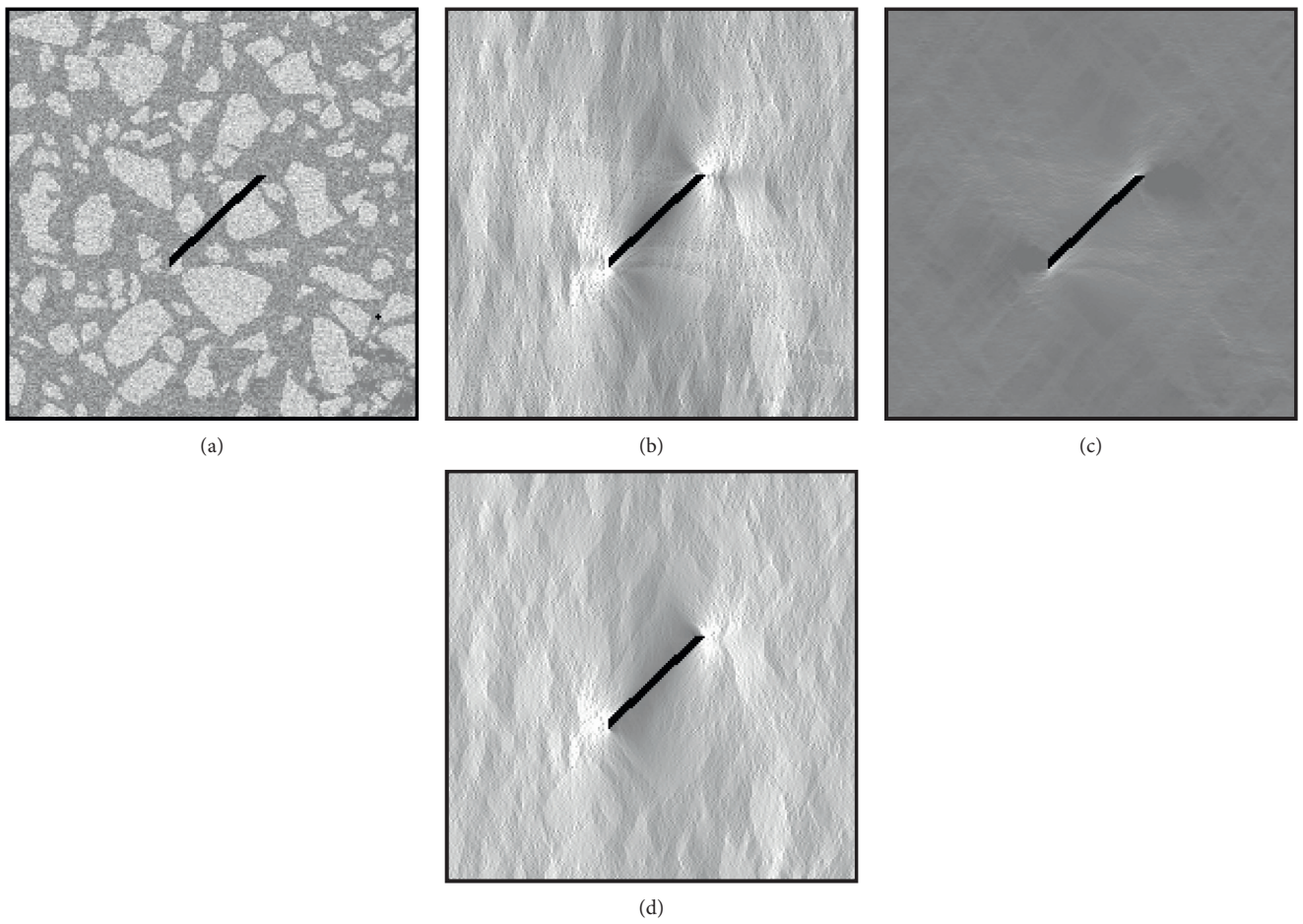

Figure 5: The specimen's elastic modulus and primary stress distribution diagram at the initial loading stage.

Table 2: Concrete compressive strength and elastic modulus simulation results

Inclination/(°)	Compressive strength(MPa)	Elastic modulus(GPa)
α=15°	93.71	22.31
α=30°	94.35	23.01
α=45°	103.86	23.88
α=60°	112.38	25.47
α=75°	143.84	25.68

the initiation and propagation of wing cracks are almost the same as when α=30°, but the failure process is relatively complicated, when the peak strength is approaching, a sudden initiation in the lower right part of the sample is caused by the large accumulation of tensile damage, the secondary coplanar cracks expanded rapidly, a secondary coplanar crack and a secondary oblique crack appeared in the upper left part of the sample. Eventually, all the cracks penetrated and the specimen was destroyed; All of the wing cracks initiated and expanded along the tip of the prefabricated crack when α=60°. As the continuous accumulation of axial stress, a large number of tensile failures occurred near the peak strength, resulting in the rapid initiation of a secondary oblique crack in the lower right part of the specimen, and a rapid initiation of the weak surface in the upper left part, coplanar cracks are generated, and the final grain penetration leads to macroscopic failure of the specimen; The tips of the prefabricated crack are located in the high-strength aggregate when α=75°, resulting in wing cracks at the tip of the prefabricated crack during the entire loading process, the expansion is slow, and when the peak strength is approaching, a large amount of tensile failure occurs on the weak surface of the lower right part and the upper end of the sample due to the accumulation of stress, the crack finally penetrates and the sample is unstable and damaged.

The components of tensile failure (yellow) dominate the acoustic emission development diagram, and the macroscopic shear bands generated by the specimen's failure are primarily related by the elements of tensile failure. In the process of concrete failure, the initiation and propagation of wing cracks have a certain randomness, with the increase of the inclination of the prefabricated cracks, the length of the wing cracks becomes shorter and the initiation position of the cracks keeps approaching the tip. When α=45° and α=60°, the rupture process of the specimen is more complicated; When 15°≤α≤45°, it is easier to initiate and propagate wing cracks, when α=60° and α=75°, the initiation and propagation of wing cracks is problematic, and when the

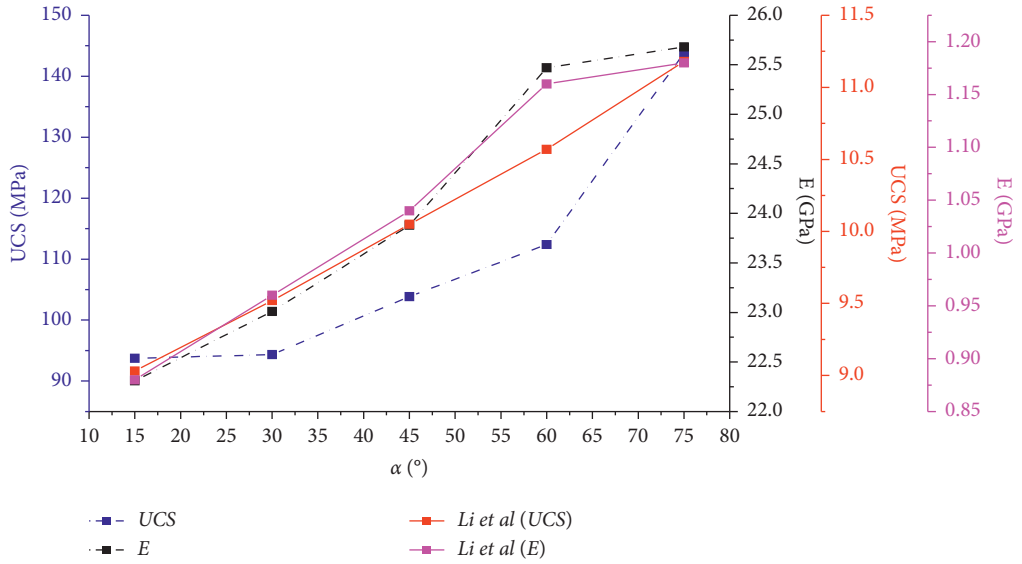

Figure 6: Cracked concrete peak strength and elastic modulus at various inclination degrees.

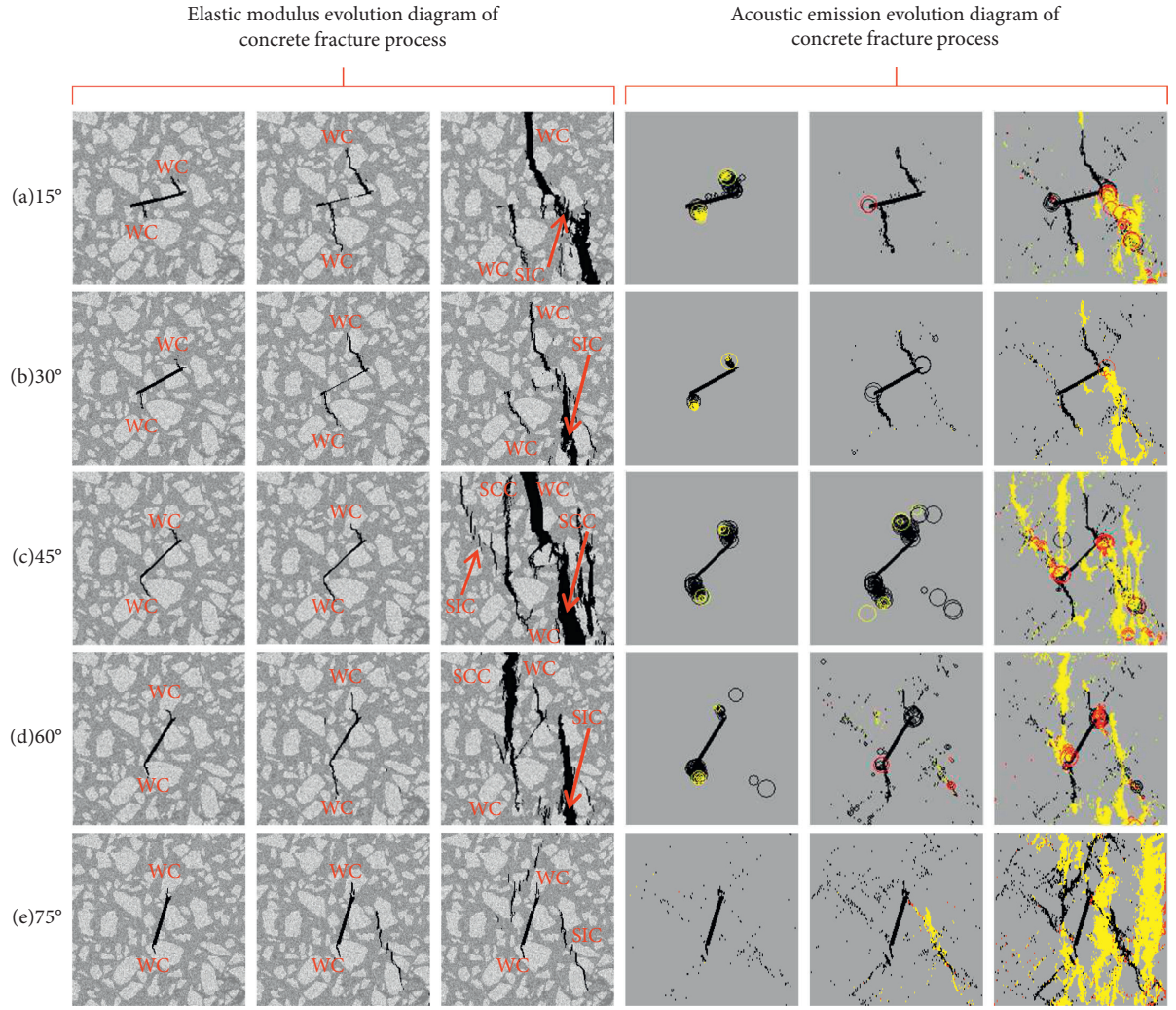

Figure 7: Failure process and acoustic emission evolution diagram of cracked concrete at different inclination angles.

tension is near the peak stress, cracks begin to form and spread quickly, which will eventually lead to split failure. From the evolution diagram of elastic modulus, it can be seen that the initiation and propagation of cracks first spread along the weak plane due to the microscopic inhomogeneity. When the stress increases, the crack penetrates the aggregate to form transgranular cracks, which causes the crack to grow along the weak plane, with a regular expansion path, the specimen will eventually produce a tensile stress concentration area at the crack tip, which leads to crack penetration and tensile split failure. The shape of the inherent crack defects in concrete has an important influence on its failure mode. Furthermore, the aggregate acts as a barrier to the initiation and development of cracks.

3.3. The law of energy change in the process of damage evolution. Acoustic emission is an efficient instrument for studying the evolution process of internal rock damage since it relates to the elastic wave released by the quick release of local energy under load. In the RFPA2D numerical model, the method of stiffness degradation is used to deal with the failure elements, each failure element can be regarded as a micro-failure, and a element micro-failure is an acoustic emission event. The position of the acoustic emission is the center of the element and the magnitude of the acoustic emission energy, it is the energy released by the micro-failure of the element, and the total number of damaged elements in each step can be used as the acoustic emission count at the current moment, and the cumulative number of damaged elements is the cumulative number of acoustic emissions. The accumulation of continuously damaged elements causes gradual damage to the entire material[20, 21]. The AE counts, cumulative AE counts, and stress changes of different inclination flaw samples with the loading step are shown in Figure 8.

Figure 8 shows that as the loading step is increased, the stress grows linearly until the peak strength is reached, at which point the stress drops significantly, while there is still some residual strength. The entire process can be divided into three stages: elastic, yield, and failure. There are less damage elements in the material at the start of the loading process, resulting the AE count and cumulative AE count are also less (paragraph 0-I in Figure 8). As the continuous action of stress, there are more and more damage elements inside the material, a large number of damaged elements gather to form micro-cracks, the AE count reaches the maximum when the stress reaches the peak value, and the stored elastic energy is suddenly released, causing the crack to penetrate and the sample to be unstable and failure. During the loading process, as the stress continues to release more and more dissipated energy, the release of the dissipated energy of each sample has similar change characteristics. In the early stage, the AE energy is small, and it increases rapidly when it is close to the peak stress. The cracks grow slowly at the initial stage, and the cracks mainly grow and penetrate rapidly when they are close to the peak strength. The cumulative AE energy grows almost exponentially with the increase of the loading step before reaching the peak stress. Flat phase (0-I section), acceleration period (I-II section), and inflation period (II-III section) are the three stages of the growth process. The accumulated AE energy in the flat period mainly comes from the dissipated energy, after the acceleration period, the accelerated growth of the cracks in the material leads to the release of part of the elastic energy, and the accumulated AE energy increases rapidly. When the peak strength is reached, the internal cracks in the material penetrate and cause the sample macroscopic damage and the accumulated AE energy reaches its peak instantaneously.

3.4. Fractal characteristics of damage evolution of concrete materials with flaw

3.4.1. Fractal analysis of images using the box-counting method. Fractal theory can effectively describe the internal regularity of many irregular appearances in nature, and has shown its unique application prospects in many fields such as geotechnical engineering, biology, physics, and computer graphics [4, 16, 18, 28]. Fractal dimension is one of the core contents of fractal theory, fractal dimension is used to replace the integer dimension of traditional European space, which can quantitatively characterize things with non-integer value dimension. While there are many ways to define the fractal dimension, the box-counting dimension can directly reflect the pixels occupied by the damaged element in the picture and the calculation is simpler than other methods. This paper chooses the box-counting dimension to test the concrete with flaw, such damage evolution characteristics are studied. The principle is that a square grid $(\delta\times\delta)$ is used to cover the damaged element in the image and the grid size is variable. Given the size of the box δ, the number of boxes N which required to cover the failure element can be calculated. Assuming that the number of boxes required to cover the destruction element with a square box of size δ_i in step i is $N_i(\delta_i)$, the size of the box in step i+1 is δ_i+1, and the number of boxes required is N_i+1(δ_i+ 1). In the covering process, a set of (δ, N) data will be obtained, and the data will be fitted into a straight line in the logarithmic graph, and the slope of the straight line is equal to the box-counting dimension D of the set, which can be expressed as formula (2).

$$D = -\lim_{\delta \longrightarrow 0} \frac{\lg N(\delta)}{\lg \delta}. \tag{2}$$

Based on the above understanding and the principle of digital image storage, combined with the digital image analysis technology and Matlab calculation function, the image recognition processing and data analysis system of brittle materials was developed independently[4]. The main flow of the algorithm is as follows: (1) Use different scales to mesh the image. First, process the image into a 500×500 pixel size picture, then the processed image is read in and binarization is processed to store relevant date (Figure 9(a)); (2) Cover the binary image with a square box with a side length of δ, calculate and count the number of square boxes $N(\delta)$ in the damaged area and save the relevant data, a set of

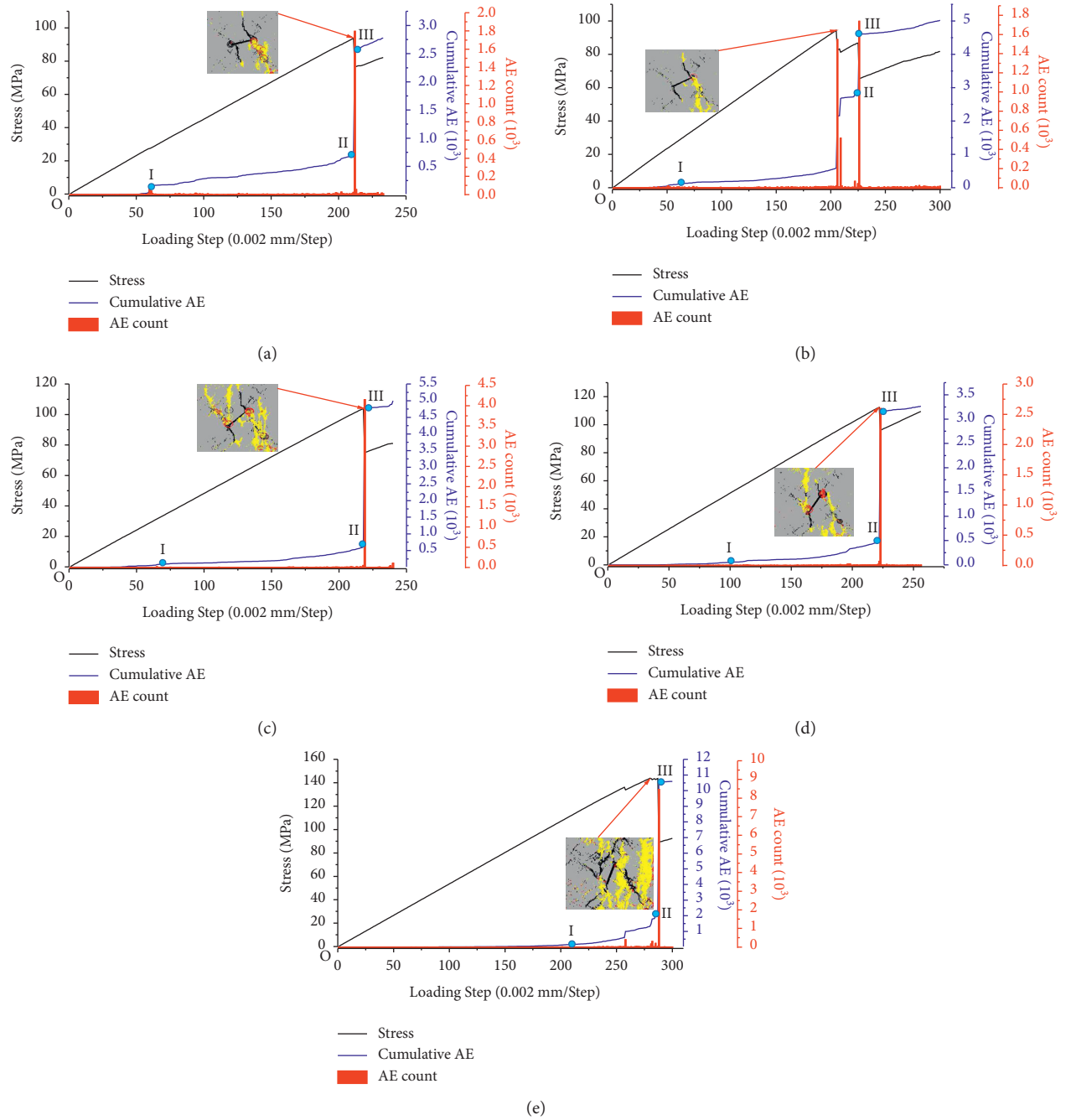

Figure 8: AE counts, cumulative AE counts, and stress changes with loading steps for samples with different inclination angles. (a)-(e) represents specimens 15°, 30°, 45°, 60°, 75°, respectively.

$N(\delta)$ and δ data could be obtained by covering the same damage area with different scales of δ, and the $\delta=2^n$ (n=1,2,3, . . .9) as shown in Figure 9(b); (3) Take double logarithmic coordinates of $N(\delta)$ and δ for regression analysis and use the fitted line, the value of D can be obtained by the slope of the fitted line.

Figure 10 depicts the process of calculating the box dimension of the acoustic emission binary image during the concrete failure process using the self-developed brittle material hole crack image recognition processing and data analysis system. When α=45° and the stress level is 70 % , Figure 11 shows that the fractal fitting relationship diagram of the failure of the concrete sample. Table 3 shows the acoustic emission energy values and fractal dimensions of numerical samples at various stress levels.

Under various stress settings, Figure 12 depicts the link between the sample and acoustic emission energy. Figure 12 demonstrates that as the stress level rises, the acoustic emission energy rises as well. The damage development under different stress conditions is a gradual acceleration process (increasing slope). The axial stress is near to the peak intensity when the stress level is greater than 90%, which

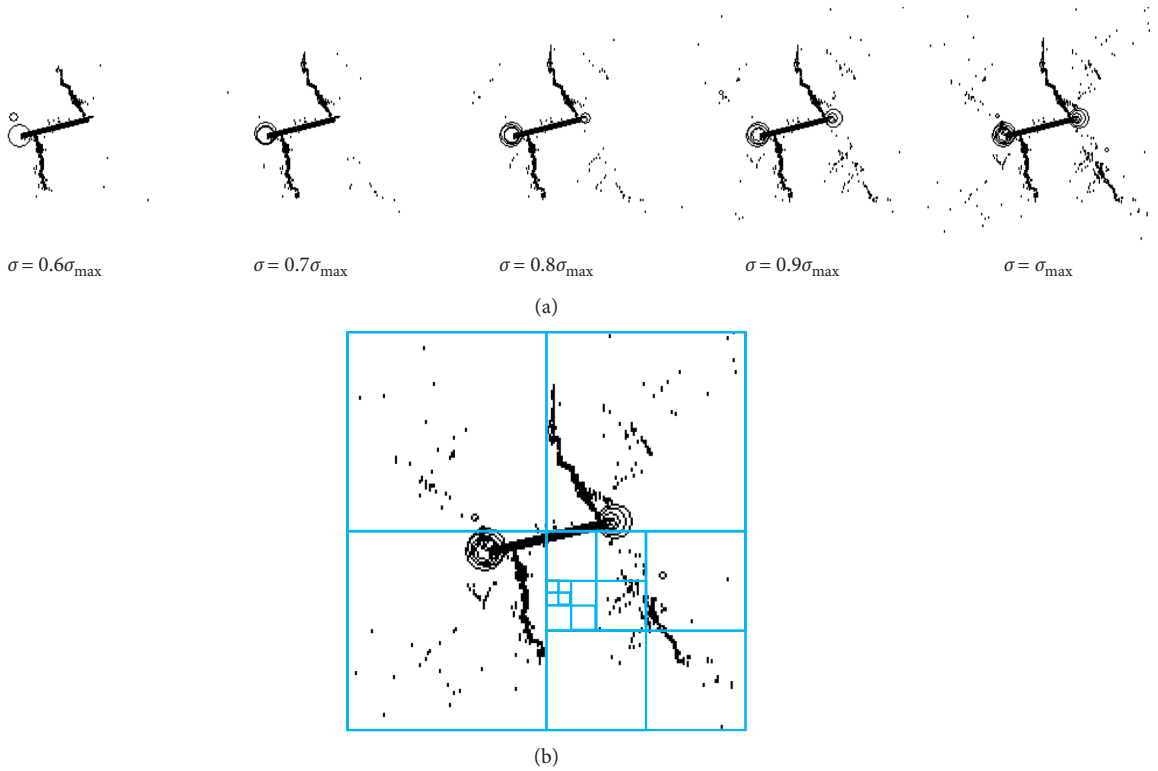

Figure 9: Schematic diagram of calculation of fractal dimension of concrete material fracture evolution.

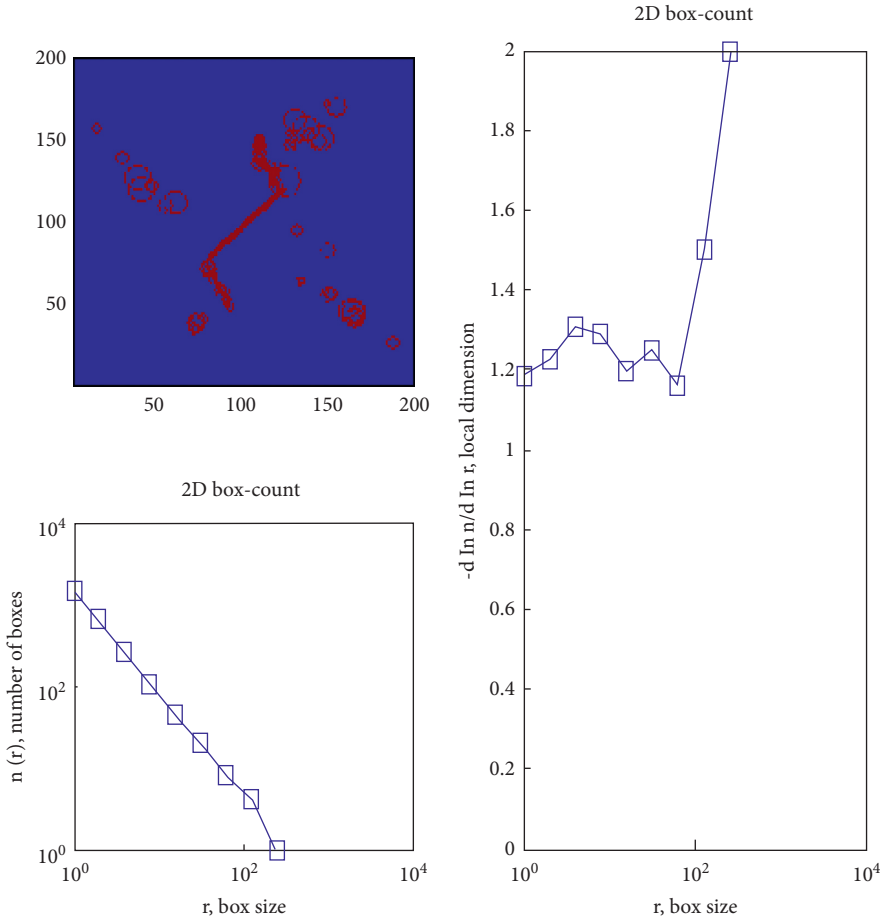

Figure 10: when α=45°, the fractal dimension is calculated (the stress level is 70%)

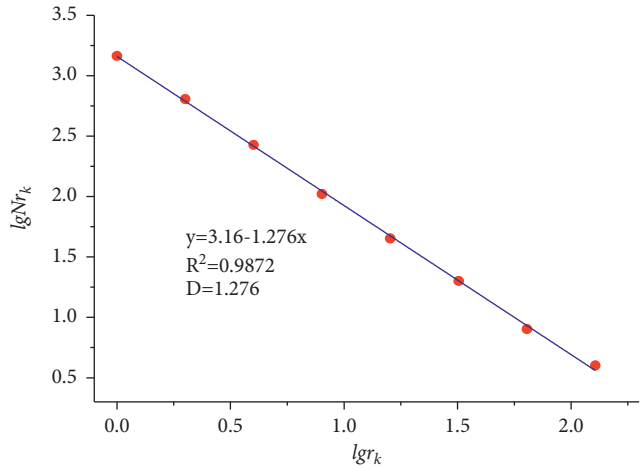

Figure 11: Fractal dimension of damage area calculation results when α=45° (stress level of 70%).

Table 3: AE energy and fractal dimension values for numerical samples at various stress levels

		Stress level									
Inclination		10%	20%	30%	40%	50%	60%	70%	80%	90%	100%
α = 15°	AE	54	73	159	206	295	314	382	434	519	717
	D	0.840	0.915	1.073	1.163	1.198	1.219	1.242	1.275	1.34	1.419
	ω	0.420	0.459	0.537	0.582	0.599	0.610	0.621	0.638	0.67	0.710
α = 30°	AE	62	88	112	167	185	203	256	320	402	594
	D	0.982	0.987	1.131	1.167	1.187	1.20	1.22	1.285	1.328	1.423
	ω	0.491	0.494	0.567	0.584	0.594	0.60	0.61	0.643	0.664	0.712
α = 45°	AE	64	71	78	120	131	168	195	294	400	633
	D	0.899	0.962	1.042	1.101	1.18	1.251	1.276	1.303	1.352	1.44
	ω	0.449	0.481	0.521	0.551	0.59	0.626	0.638	0.652	0.676	0.72
α = 60°	AE	47	69	76	81	92	108	116	174	334	542
	D	0.807	0.938	1.01	1.176	1.196	1.214	1.273	1.298	1.326	1.401
	ω	0.404	0.469	0.505	0.588	0.598	0.607	0.637	0.649	0.663	0.701
α = 75°	AE	44	83	96	119	141	144	172	180	421	1319
	D	0.815	0.982	0.995	0.998	1.071	1.122	1.129	1.259	1.396	1.544
	ω	0.408	0.491	0.498	0.499	0.536	0.561	0.565	0.630	0.698	0.772

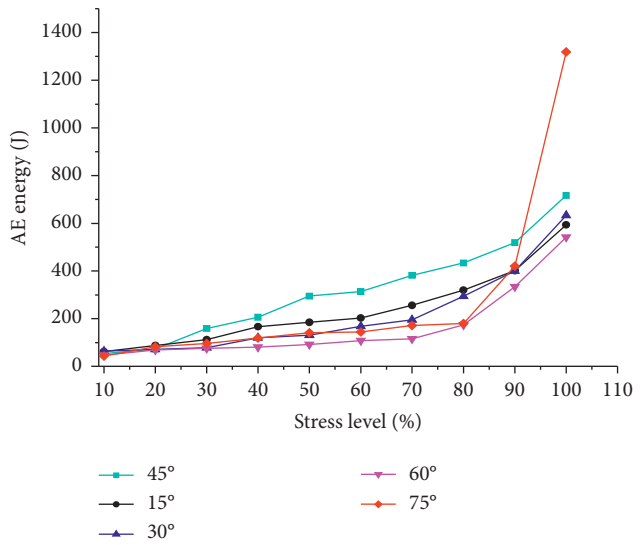

Figure 12: The connection between AE energy and various levels of stress.

causing the crack to penetrate and release a large amount of energy, resulting in a large number of elements damaged, the number of acoustic energy increased sharply and the location was highly concentrated. A macroscopic failure zone (Figure 7) is formed. The acoustic emission energy value released by the sample with α=75° is the greatest when the stress reaches its peak intensity. Combined with the acoustic emission evolution in Figure 7, it can be seen that the internal damage is the most serious and the macroscopic failure is the most severe.

The fractal dimension of each selected binary picture is extracted after performing fractal analysis on the corresponding damage evolution binary picture under different stress levels, and the change in dimension is shown in Figure 13. The degree of damage to the microstructure of each sample's material increases as the stress level increases, there are more and more failure elements on the corresponding damage evolution binary diagram (Figure 9(a)) and the fractal dimension increases accordingly. Meanwhile, the corresponding damage evolution binary diagram has

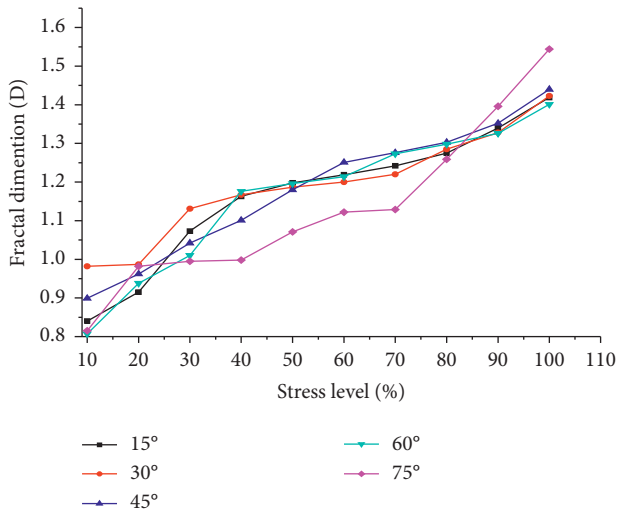

Figure 13: Relationship between fractal dimension and different stress levels.

more and more rupture elements (Figure 9(a)) and the fractal dimension increases. When the stress reaches the critical value, the stress suddenly drops at the same time accompanied by abrupt behaviors such as the rapid increase of failure elements and the increase of damage fractal dimension. The failure probability and fractal dimension change little when the stress level is less than 30%. Material failure is actually a self-organizing process from disordered distribution to concentrated order, the failure elements develop from overall random distribution to local concentration, macroscopically it is the initiation and expansion of microcracks, the size of the fractal dimension reflects the damage. This means that there are more and more fine defects, which tend to diffuse into the entire sample. As the stress level increases, the development of damage inside the material is a gradual acceleration process, reflecting the accelerated deterioration of the mechanical properties of the material under the action of stress until it is destroyed. When Figures 11 and 12 are compared, it is clear that the evolution process of the material's internal fracture shows a general trend of increasing dimensionality. When the stress level is 100%, there is a good corresponding relationship between the change of fractal dimension and the energy release, which is expressed as acoustic emission energy, the greater the release, the greater the fractal dimension, and the more serious the internal damage of the material.

3.4.2. Damage variable based on fractal theory. Although there are many methods to determine rock damage variables, most of them are still describing the quantitative relationship of micro-fracture evolution, the spatial distribution characteristics of micro-fractures have not been reflected, and the damage characteristics of rock materials cannot be truly reflected. Therefore, exploring a method that can truly reflect the process of mechanics and can be easily obtained and objectively measured is an important issue that needs to be solved urgently in the geotechnical engineering community. However, the damage and failure process of materials is actually the development, inoculation and evolution process of internal micro-fractures. Since the method of stiffness degradation is used to deal with the failure elements in the numerical model, each failure element can be regarded as a micro-fracture. Larger-scale cracks are formed by the failure elements connections. Therefore, the number and location distribution characteristics of the failure elements reflect the damage degree of the concrete specimens.

Based on the research foundation of section 3.4.1, this article attempts to establish the relative relationship between the damage variable and the damage degree represented by the box dimension, and use a more convenient quantitative method to express complex objects that are difficult to quantify. The definition of the damage variable expressed by the box dimension is as follows:

$$\omega = \frac{D_i - D_0}{D_{\max} - D_0}, \tag{3}$$

where ω represents the damage variable, D_i represents the fractal dimension of the internal fracture area of the material when the stress level is i%; when the material is not loaded, D_o denotes the fractal dimension of the internal fracture region of the material; $D_{\max}$ represents the fractal dimension of the fracture area when the material is completely failure. Since this research is a two-dimensional problem, $D_{\max} = 2$. According to formula (3), the damage variable ω of the sample under different stress levels can be calculated, as shown in Table 3.

When comparing Figures. 13 and 14, it's clear that the damage variable ω and the fractal dimension D have a synchronized changing trend, and both increase continuously with the increase of stress. This is due to the continuous development of a large number of micro-defects in the material in the process of deformation, and the occurrence of macroscopic failure is caused by the continuous accumulation of internal damage of the material. As the increase of the stress level, the increase of the internal failure elements of the material leads to the fuller the development and expansion of the micro-defects, the larger the damage variable (ω) and the fractal dimension. The generation and evolution of the internal fracture of the material can be described by the change. Thence, based on the damage variable (ω) of fractal theory, the damage of rock-like materials is characterized. Different crack propagation paths result from the distribution form of a single crack in concrete. Due to microscopic non-uniformity, cracks begin to form and propagate over the weak surface, which leads to the expansion of the crack along the weak surface to form an irregular propagation path, which is expressed as the fractal dimension D and the damage variable ω have a certain difference in the damage evolution process of the material, that is, $\omega_{75°} > \omega_{45°} > \omega_{30°} > \omega_{15°} > \omega_{60°}$.

3.5. Application prospect analysis of damage variable based on fractal theory in damage evolution of roadway in Lannigou Gold Mine. The Lannigou Gold Mine is the largest fault-

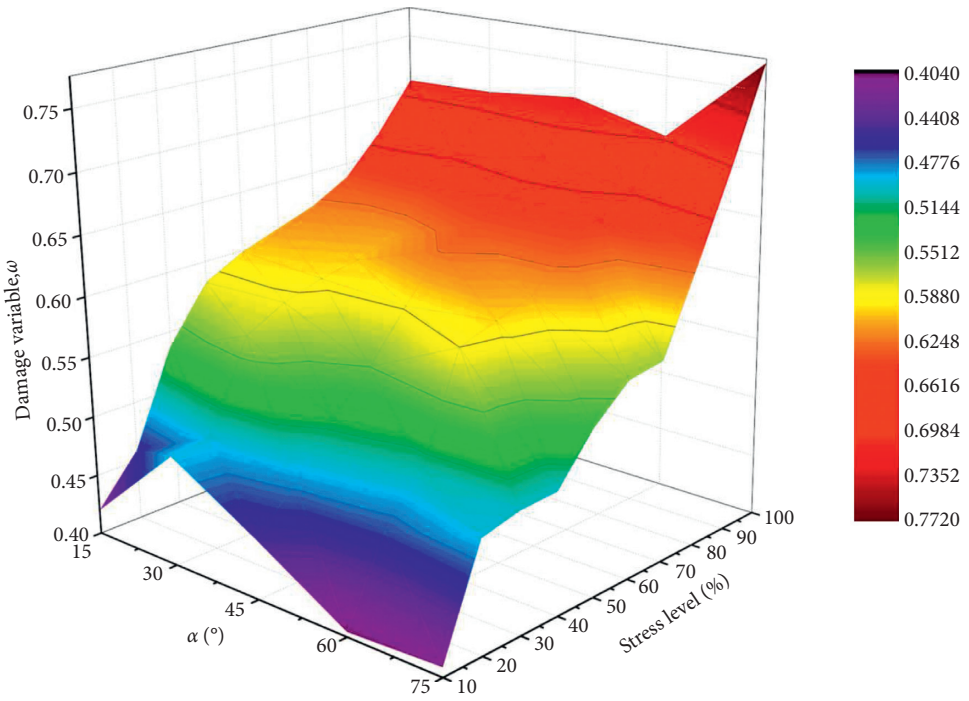

Figure 14: Relationship between damage variable, stress levels, and inclination.

controlled Carlin-type gold deposit in southwestern Guizhou. From 1987 to the end of 2005, the identified resources amounted to 126.25 tons, reaching an extremely large scale [29]. Multiple periods of tectonic movement have occurred in the mine, resulting in complex geological circumstances for the ore body's occurrence. During the deep mining process, the surrounding rock of the deep roadway has encountered challenges such as large deformation and support difficulties [30, 31]. The practice of deep mining engineering has been ahead of the systematic exploration of related basic theories, and there lindness, inefficiency and uncertainty in engineering practice to a certain extent. Therefore, this research can provide certain theoretical support for the optimization of deep wet shotcrete support strength and parameters of Lannigou Gold Mine.

At present, domestic and foreign researchers have obtained many research results on the damage evolution of surrounding rock in deep mining tunnels. Zhu et al. used RFPA software and assumed that the elastic modulus and strength indexes of the rock obey the Weibull distribution, and numerically simulated the initiation, expansion and penetration process of the underground surrounding rock fractures [32]. Zhang et al. aimed at the difficulty of controlling the stability of the surrounding rock in deep broken soft rock roadways, analyzed the deformation and failure characteristics and failure mechanism of the surrounding rock [33]. Dou et al. investigated the effect of shear displacement in the roadway's surrounding rock on fluid flow and solute transport in rough fractures [34]. Gao et al. studied the drilling behavior and mechanism of cores below 4500 m in Well Songke 2 in order to learn more about the damage mechanisms of the surrounding rocks [35].The above research has important reference value for the understanding of roadway failure mechanism, but there are few reports on how to quantify the degree of roadway failure. However, the essence of roadway failure is the macro-mechanical response generated by the accumulation of internal damage to a certain extent. If the whole process of roadway from damage to final failure can be quantitatively characterized, it will help to reveal the damage of the surrounding rock of deep roadway and provide a reference for the stability control of the surrounding rock of the roadway.

This study describes the damage evolution process inside the material based on fractal theory, and proposes a damage variable index (ω) based on fractal theory. Using ω as a parameter to characterize the degree of material damage, the macroscopic failure characteristics of the material and its internal fracture evolution are unified and the inconvenience of too many mechanical parameters involved in the damage definition is overcome, and provides a new method for quantitatively studying the damage evolution characteristics of rock-like materials. Based on the study in this article, we independently developed a system for image recognition and processing of pores and cracks in brittle materials and data analysis. In view of the control problems of the surrounding rock of the Lannigou gold mine and the study ideas in this article, this system can calculate the fractal dimension to analyze the damage evolution of the roadway's surrounding rock. In order to better understand the damage evolution process of the surrounding rock of the roadway, a damage variable index based on the fractal dimension is presented to measure the degree of growth of cracks in the surrounding rock, so as to provide certain guidance for the safe production of the mine.

4. Conclusion

(1) The box dimension is used to describe the internal damage evolution binary diagram of the material, and it is found that the damage fractal dimension has a linear relationship with the stress at different stages. A damage variable index (ω) based on the fractal theory is proposed, and ω is used as a parameter to characterize the degree of material damage. The macroscopic failure characteristics of the material and its internal fracture evolution are unified and the inconvenience of too many mechanical parameters involved in the damage definition is overcome. The larger the ω, the higher the degree of damage to the material. The proposed index introduces a new way for studying the damage evolution characteristics of rock-like materials in a quantitative manner.

(2) The crack inclination angle has a substantial impact on the elastic modulus and compressive strength of concrete materials, and exhibits non-linear properties as the angle increases. The material's interior microscopic non-uniformity causes an uneven internal stress distribution, and wing crack initiation and propagation paths are somewhat random. As the prefabricated crack inclination angle increases, the wing crack length shortens, and the wing crack initiation point moves closer to the prefabricated crack tip.

(3) Due to the influence of the internal non-uniformity of the material, when $15^\circ \leq \alpha \leq 45^\circ$, the wing crack initiation and expansion is easier. When $\alpha=60^\circ$ and $\alpha=75^\circ$, it is difficult for the wing crack to initiate and expand. When approaching the peak stress, the crack initiation and spread suddenly. Finally, the splitting failure is formed.

(4) The crack specimens with different inclination angles have similar evolution characteristics of acoustic emission. The AE energy is small in the early stage of loading, and it increases rapidly when the stress is close to the peak. The cumulative AE energy reflects the entire destruction process of the material under compression. It expands exponentially as the loading step is increased, the growth process can be separated into three phases: flat, acceleration, and inflation.

Data Availability

Some or all data, models, or code generated or used during the study are available from the corresponding author by request.

Conflicts of Interest

The authors declares that there is no conflict of interest regarding the publication of this paper.

Acknowledgments

The study was funded by the Guizhou Province Science and Technology Support Program Project (No: QIANKEHE Support [2021] General 516); National Natural Science Foundation of China (No: 51964007, 41962008, 51774101).

References

[1] C. Zhu, M.-c. He, B. Jiang, X.-z. Qin, Q. Yin, and Y. Zhou, "Numerical investigation on the fatigue failure characteristics of water-bearing sandstone under cyclic loading," *Journal of Mountain Science*, vol. 18, no. 12, pp. 3348–3365, 2021.

[2] G. C. Shi, X. J. Yang, H. C. Yu, and C. Zhu, "Acoustic emission characteristics of creep fracture evolution in double-fracture fine sandstone under uniaxial compression," *Engineering Fracture Mechanics*, vol. 210, pp. 13–28, 2018.

[3] C. Zhu, M. C. He, X. H. Zhang, Z.-g Tao, Q. Yin, and L.-f Li, "Nonlinear mechanical model of constant resistance and large deformation bolt and influence parameters analysis of constant resistance behavior," *Rock and Soil Mechanics*, vol. 42, no. 7, pp. 1911–1924, 2021.

[4] H. Liu, Y. Zuo, Z. Wu et al., "Fractal analysis of mesoscale failure evolution and microstructure characterization for sandstone using DIP, SEM-EDS, and micro-CT," *International Journal of Geomechanics*, vol. 21, no. 9, Article ID 04021153, 2021.

[5] Z. Li, L. Li, B. Huang et al., "Numerical investigation on the propagation behavior of hydraulic fractures in shale reservoir based on the DIP technique," *Journal of Petroleum Science and Engineering*, vol. 154, pp. 302–314, 2017.

[6] C. Cao, W. Zhang, J. Chen, B. Shan, S. Song, and J. Zhan, "Quantitative estimation of debris flow source materials by integrating multi-source data: a case study," *Engineering Geology*, vol. 291, Article ID 106222, 2021.

[7] R. C. Nolen-Hoeksema and R. B. Gordon, "Optical detection of crack patterns in the opening-mode fracture of marble," *International Journal of Rock Mechanics and Mining Sciences*, vol. 24, no. 4, pp. 135–144, 1987.

[8] S.-Q. Yang and H.-W. Jing, "Strength failure and crack coalescence behavior of brittle sandstone samples containing a single fissure under uniaxial compression," *International Journal of Fracture*, vol. 168, no. 2, pp. 227–250, 2011.

[9] C. H. Park and A. Bobet, "Crack coalescence in specimens with open and closed flaws: a comparison," *International Journal of Rock Mechanics and Mining Sciences*, vol. 46, no. 5, pp. 819–829, 2009.

[10] A. Manouchehrian, M. Sharifzadeh, M. F. Marji, and J. Gholamnejad, "A bonded particle model for analysis of the flaw orientation effect on crack propagation mechanism in brittle materials under compression," *Archives of civil and mechanical engineering*, vol. 14, no. 1, pp. 40–52, 2014.

[11] X. P. Zhang and L. N. Y. Wong, "Cracking processes in rock-like material containing a single flaw under uniaxial compression: a numerical study based on parallel bonded-particle model approach," *Rock Mechanics and Rock Engineering*, vol. 45, no. 5, pp. 711–737, 2012.

[12] T. Liu, B. Lin, W. Yang, Q. Zou, J. Kong, and F. Yan, "Cracking process and stress field evolution in specimen containing combined flaw under uniaxial compression," *Rock Mechanics and Rock Engineering*, vol. 49, no. 8, pp. 3095–3113, 2016.

[13] R. C. Xu, "Influence of flaw inclination angle on cracking behavior of rock-like materials under uniaxial compression," *Advances in Materials Science and Engineering*, vol. 2019, no. 1, 10 pages, Article ID 6942586, 2019.

[14] L. M. Taylor, E.-P. Chen, and J. S. Kuszmaul, "Microcrack-induced damage accumulation in brittle rock under dynamic

loading," *Computer Methods in Applied Mechanics and Engineering*, vol. 55, no. 3, pp. 301–320, 1986.

[15] T. J. Ahrens and A. M. Rubin, "Impact-induced tensional failure in rock," *Journal of Geophysical Research: Planets*, vol. 98, no. E1, pp. 1185–1203, 1993.

[16] H. Xie, *Fractals in Rock Mechanics*, A A Balkema, Rotterdam, Netherlands, 1993.

[17] M. Gao, J. Xie, Y. Gao et al., "Mechanical behavior of coal under different mining rates: a case study from laboratory experiments to field testing," *International Journal of Mining Science and Technology*, vol. 31, no. 5, pp. 825–841, 2021.

[18] H. Liu, L. Zheng, Y. Zuo et al., "Study on mesoscopic damage evolution characteristics of single joint sandstone based on micro-CT image and fractal theory," *Shock and Vibration*, vol. 2021, Article ID 6547028, 18 pages, 2021.

[19] Q. Yu, W. Zhu, C. a. Tang, and T. Yang, "Impact of rock microstructures on failure processes - numerical study based on DIP technique," *Geomechanics and Engineering*, vol. 7, no. 4, pp. 375–401, 2014.

[20] C. Tang, "Numerical simulation of progressive rock failure and associated seismicity," *International Journal of Rock Mechanics and Mining Sciences*, vol. 34, no. 2, pp. 249–261, 1997.

[21] Q. L. Yu, *Digital Image Processing-Based Numerical Methods for Failure Process Analysis of Rock-like materials*, Northeastern University, Shenyang, China, 2008.

[22] W. Weibull, "A statistical distribution function of wide applicability," *Journal of Applied Mechanics*, vol. 18, no. 3, pp. 293–297, 1951.

[23] F. Rossi, A. Di Carlo, and P. Lugli, "Microscopic theory of quantum-transport phenomena in mesoscopic systems: a Monte Carlo approach," *Physical Review Letters*, vol. 80, no. 15, pp. 3348–3351, 1998.

[24] R. Y. Rubinstein and D. P. Kroese, *Simulation and the Monte Carlo Method. 707*, John Wiley & Sons, Hoboken, NJ, USA, 2011.

[25] B. H. G. Brady and E. T. Brown, *Rock Mechanics for Underground mining*, pp. 106–108, Chapama and Hall, London, UK, 1993.

[26] D. Li, E. Wang, X. Kong, M. Ali, and D. Wang, "Mechanical behaviors and acoustic emission fractal characteristics of coal specimens with a pre-existing flaw of various inclinations under uniaxial compression," *International Journal of Rock Mechanics and Mining Sciences*, vol. 116, pp. 38–51, 2019.

[27] A. Bobet, "The initiation of secondary cracks in compression," *Engineering Fracture Mechanics*, vol. 66, no. 2, pp. 187–219, 2000.

[28] J. Jin, P. Cao, and C. Z. Pu, "Effect of preformed fracture geometry parameters on failure mode and strength of rock-like materials," *Journal of Central South University*, vol. 45, no. 2, pp. 529–535, 2014, in Chinese.

[29] C. Maohong, M. Jingwen, F. P. Bierlein, T. Norman, and P. J. Uttley, "Structural features and metallogenesis of the carlin-type Jinfeng (Lannigou) gold deposit, Guizhou Province, China," *Ore Geology Reviews*, vol. 43, no. 1, pp. 217–234, 2011.

[30] L. Zheng, Y. Zuo, and Y. Hu, "Deformation mechanism and support technology of deep and high-stress soft rock roadway," *Advances in Civil Engineering*, vol. 2021, Article ID 6634299, 14 pages, 2021.

[31] D. Chen, H. Chen, and W. Zhang, "An analytical solution of equivalent elastic modulus considering confining stress and its variables sensitivity analysis for fractured rock masses," *Journal of Rock Mechanics and Geotechnical Engineering*, 2021.

[32] W. C. Zhu, J. Liu, C. A. Tang, X. D. Zhao, and B. H. Brady, "Simulation of progressive fracturing processes around underground excavations under biaxial compression," *Tunnelling and Underground Space Technology*, vol. 20, no. 3, pp. 231–247, 2005.

[33] G. C. Zhang and F. L. He, "Deformation failure mechanism of high stress deep soft roadway and its control," *Journal of Mining & Safety Engineering*, vol. 32, no. 4, pp. 571–577, 2015.

[34] Z. Dou, S. X. Tang, and X. Y. Zhang, "Influence of shear displacement on fluid flow and solute transport in a 3D rough fracture," *Lithosphere*, vol. 2021, Article ID 1569736, 2021.

[35] M. Z. Gao, H. C. Hao, and S. N. Xue, "Discing behavior and mechanism of cores extracted from Songke-2 well at depths below 4500 m," *International Journal of Rock Mechanics and Mining Sciences*, vol. 149, Article ID 104976, 2022.

Hindawi
Advances in Materials Science and Engineering
Volume 2022, Article ID 7692772, 11 pages
https://doi.org/10.1155/2022/7692772

Research Article

Monitoring and Analysis of a High-Performance Concrete Shaft Lining: A Case Study

Daolu Quan,[1,2] Hongguang Ji,[1,2] Xiaobo Su,[1,2] Hui Cao,[1] and Juanhong Liu[1,2]

[1]*College of Civil and Resource Engineering, University of Science and Technology Beijing, Beijing 100083, China*
[2]*Key Laboratory of Urban Underground Space Engineering, University of Science and Technology Beijing, Beijing 100083, China*

Correspondence should be addressed to Hongguang Ji; 1274242908@qq.com

Received 13 December 2021; Revised 5 January 2022; Accepted 8 January 2022; Published 31 January 2022

Academic Editor: Ren Fuqiang

Copyright © 2022 Daolu Quan et al. This is an open access article distributed under the Creative Commons Attribution License, which permits unrestricted use, distribution, and reproduction in any medium, provided the original work is properly cited.

Shaft lining in ultradeep mines on the coast of eastern China under the complex external environments of "high in situ stress and high osmotic pressure" has the disadvantages of failure; to solve this problem, the field test of high-performance concrete shaft lining structure was carried out in Sha-ling gold mine. The field test study of the high-performance concrete shaft lining was carried out in a −1120 m ingate and a −1114 m to −1124 m shaft. Its stress and deformation were monitored and analyzed. The maximum compressive stress of the HPC shaft lining structure at the level of −1117.7 m of the air intake shaft is 1.91 MPa. Based on the Von-Mises yield theory and the analytical solution of thick-walled cylinder theory, the ultimate limit of the high-performance concrete shaft lining in the Sha-ling gold mine was obtained. The high-performance concrete shaft lining strain changes smoothly, and concrete strain can be divided into three stages: the rapid growth period, the slow growth period, and the stable period. The monitoring results show that the high-performance concrete shaft lining has excellent mechanical properties in the external environment of high in situ stress, which can be used as a reference for the support design of similar projects.

1. Introduction

Under the complex external environments of "high in situ stress, high ground temperature, high water pressure, and strong excavation disturbance" [1], the physical and mechanical properties of deep rock masses are generally different from those of shallow rock masses [2, 3]; thus, the rock masses change from an elastic state to a plastic state. The pressure distribution of the surrounding rock and the excavation disturbance stress path will affect the stability of the surrounding rock. To study the fatigue failure characteristics of sandstone, Zhu et al. carried out cyclic loading and unloading numerical simulation tests of sandstone with different loading parameters and different water content [4]. Gao et al. studied the mechanical properties of coal at various mining rates on the laboratory scale and the field scale [5]. Chen et al. adopted an analytical approach to calculate the equivalent elastic modulus of fractured rock masses with a random discrete fracture or regular fracture considering the confining stress [6]. In the process of shaft excavation, water inrush, rock-burst, lamping, and other engineering support problems are frequent occurrences. Some high-grade shaft lining concrete may even suffer brittle failure in the deep external environment of high in situ stress and high osmotic pressure. Simultaneously, the deep strata and deep-water quality in the coastal area are rich in Cl^- and SO_4^{2-} ions, putting the shaft lining concrete at risk of chemical corrosion [7–9], which seriously affects the strength and durability of the concrete [10–13] and dramatically shortens the life of the shaft lining.

Stress-strain monitoring technology has been widely used in geotechnical and underground engineering. Zhu et al. monitored and analyzed the deformation of deep foundation pit, ground subsidence, and adjacent buildings [14]. Dou et al. studied the influence of shear displacement on fluid flow and solute transport in three-dimensional rough fractures of fractured rock mass [15]. Cao et al. used the interferometric synthetic aperture radar (InSAR) technology to obtain the ground surface deformation [16]. Dou et al. investigated the influence of the layer transition

zone on the multilayered slope [17]. The shaft lining structures' stress, deformation, and strength characteristics have been studied using model tests [18–24]. Ding et al. analyzed the failure characteristics and mechanical mechanism of the slope by the physical model test [25]. Zhao et al. analyzed the plastic limit load of shaft lining based on the unified strength theory and discussed the relationship between the plastic limit load of shaft lining and the strength difference of structural materials [26]. Lyu and Wang monitored and analyzed the shaft lining deformation of the weakly cemented stratum in west China and obtained the limit deformation value of the shaft lining [27]. To study the mechanical behavior of surrounding rock under prestressed bolt support, Li et al. established the mechanical model of bolt support, and the deformation of the surrounding rock of the inclined shaft was monitored [28]. However, previous studies on the shaft lining support form usually focus on the topsoil layer; however, few reports focus on the shaft lining stress and deformation characteristics under the occurrence of the complex external environments of "high in situ stress and high osmotic pressure" in the deep stratum.

As for the deep shaft support method of metal mine, there is no mature theory so far. In the environment of high in situ stress in the deep stratum, drilling in rock mass or supporting by high-grade concrete is usually adopted to resist the large deformation of surrounding rock. However, Liu et al. presented that high-grade concrete (C50 and above) has an impact tendency and brittle failure will occur [29]. It is of engineering significance to study and use the high-performance concrete shaft lining with low impact tendency to control the deformation of surrounding rock under the environment of high in situ stress of deep metal mine.

Hence, based on the −1114 m to −1124 m section of the air intake shaft and the −1120 m ingate high-performance concrete (HPC) shaft lining structure field application research in this paper, we analyze the characteristics of stress and deformation of high-performance concrete shaft lining. Combined with the Von-Mises yield theory and thick-walled cylinder theory, the ultimate stress of the high-performance concrete shaft lining is established. The strain variation law of the HPC shaft lining is obtained. The advantages and disadvantages of the applications of HPC are summarized. It is hopeful that our work can provide a reference for a deep metal shaft lining structure design.

2. Engineering Geological

2.1. Engineering Background. As shown in Figure 1, the Sha-ling gold mine is located in Lai-Zhou City, Shandong Province. The linear distance between the northwest end of the mining area and the coast of the Bohai Sea is about 5.3 km, which belongs to the coastal area of Shandong Province. The distance between the main shaft, the auxiliary shaft, and the air intake shaft in the Sha-ling gold mine is relatively close, which is approximately triangular in space, and the linear distance between the auxiliary shaft and the air intake shaft is about 60 m.

The design depth of the air intake shaft within the Sha-ling gold mine is 1449 m, the net diameter of the shaft lining is 6.5 m, and the thickness of the support is 400 mm, which was excavated using a common method. The original support design parameters of the shaft from −1114 m to −1124 m and the ingate at −1120 m of air intake shaft are exhibited in Table 1.

2.2. Geological Background. The regional geological structure of the Sha-ling gold mine construction project is complex, and the fault structure is developed within the area. The main fault is the Jiao-Jia fault, the branch fault is the Wang-Er-Shan fault, and the north section fault is the Ling-Shan fault. The rock fissures are developed on both sides of the Jiao-Jia fault zone. The upper part of the Jiao-Jia fault is metamorphic gabbro and the lower part of the Jiao-Jia fault is dominated by granite. The rock mass from −1114 m to −1124 m is sericeous granite, and the quality grade of rock mass is grade II. The uniaxial compressive strength of sericite granite in this section is about 90 MPa. RQD value approaches 48%, and the rock mass is comparatively broken.

3. Distribution of In Situ Stress in Sha-Ling Gold Mine

Understanding the law of in situ distribution is the basis for investigating deep rock mechanics [30] in order to obtain the in situ stress distribution law of the deep strata in the shaft construction area of the Sha-ling gold mine and guide the shaft excavation. Before the shaft excavation, our research group used the hydraulic fracturing method to measure the in situ stress in the Sha-ling gold mine. In the in situ measurement of the air intake shaft in the Sha-ling gold mine, the drill pipe cannot be lowered because of the serious hole collapse. The linear distance between the auxiliary shaft and the air intake shaft is about 60 m, so the in situ measurement is carried out in the auxiliary shaft. The hydraulic fracturing in situ stress measurement equipment adopted the SY- 2007 single-loop in situ stress measurement system developed by the Institute of Geomechanics, Chinese Academy of Geological Sciences [31]. The law of in situ stress distribution in the auxiliary shaft of the Sha-ling gold mine is shown in Figure 2.

It can be seen from Figure 2 that the maximum horizontal principal stress in the shaft construction engineering area is 24.14 MPa~45.56 MPa (−775.4 m~−1532.5 m), and the minimum horizontal principal stress is 18.85 MPa~37.51 MPa (−775.4 m~−1532.5 m). The maximum and minimum horizontal principal stress near −1120 m is 35.9 MPa and 27.2 MPa, respectively.

4. Field Test Method

4.1. Raw Materials and Mixture Proportions. The HPC of the deep shaft is composed of silicate 42.5R cement, a special compound comprised of river sand, copper-plated microwire steel fiber, and a polycarboxylic acid water reducer. The mixtures' proportions of the HPC in the deep shaft are

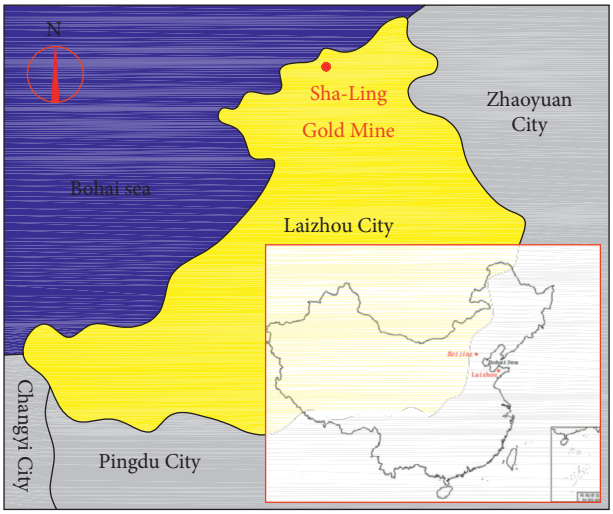

Figure 1: Location of Sha-ling gold mine.

Table 1: The original support parameters of −1114 m to −1124 m shaft lining and the −1120 m ingate of the air intake shaft.

Deep	Support parameter	
	Primary support	Second-time support
−1120 m ingate	Bolt type: MSGLW-335/20 × 2000; bolt density: 1 m × 1 m; butterfly tray: 150 × 150 × 10; density of steel mesh: 120 × 120 Rebar diameter: 6 mm	C30 reinforced concrete, support thickness: 400 mm; outer reinforced: HΦ22@250VΦ18@250 Inner reinforced: HΦ22@250VΦ18@250; stirrup: Φ10@500 ∗ 500
−1114 m to −1124 m	No	Ditto

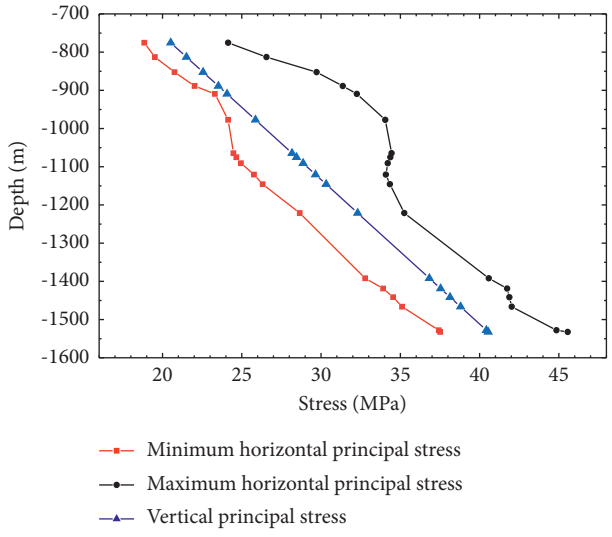

Figure 2: In situ stress distribution of auxiliary shaft in Sha-ling gold mine.

present in Table 2. The compound is composed of finely ground slag powder, fly ash, and silica fume proportions. Its performance meets the requirements of the concrete cementing materials and the compressive strength of the HPC reaches 80 MPa. Zhou et al. studied the splitting tensile strength, flexural strength, brittleness coefficient, impact energy index, dynamic failure time, and other parameters of the HPC through rigorous laboratory tests [32]. The brittleness coefficient, impact energy index, dynamic failure time, and other parameters of the HPC belong to the category of nonimpact liability, which will not be elaborated in detail in this paper.

In order to complete the field test research on the −1120 m ingate of the air intake shaft (the ingate support is

Table 2: Mixing proportions of HPC.

Composition	Cement ($kg \cdot m^{-3}$)	Special admixtures ($kg \cdot m^{-3}$)	Sand ($kg \cdot m^{-3}$)	Steel fiber ($kg \cdot m^{-3}$)	Water ($kg \cdot m^{-3}$)	Admixture ($kg \cdot m^{-3}$)	Water-binder ratio
Proportion	240	630	1205	50	200	10	0.23

5 m) and the −1114 m to −1124 m HPC shaft lining, approximately 120 m^3 of HPC was prepared on-site. The HPC was mixed evenly with a mixer and transported to the casting layer using a bucket. When the concrete was mixed, steel fiber was added in batches in order to evenly disperse the material and ensure the workability of the concrete. The HPC after mixing is shown in Figure 3, and the HPC shaft lining after the mold removal is shown in Figure 4.

4.2. Field Monitoring Instruments

4.2.1. Force-Measuring Bolt. The environment of the deep shaft in coastal areas is harsh. The complex external environments, such as high ground temperature and water drenching from the large shaft lining, put forth higher requirements for monitoring the instruments' reliability and durability. To cope with the complex external environments of the deep shaft and ensure the authenticity and reliability of the monitoring results, an improved stress monitoring sensor force-measuring bolt was used to monitor shaft lining stress. As shown in Figure 5, the force-measuring bolt is composed of three parts: the steel bar meter, the steel bar, and a steel plate within the PVC pipe. The steel bar meter is connected to both ends of the steel bar; one end of the steel bar is welded to a steel plate. The steel plate length × width is 150 × 150 mm, and the thickness is 6 mm. The force measurement bolt is 900 mm long.

Before the concrete shaft lining is poured, one end of the unconnected steel plate is fixed to the surrounding rock. The steel bar placed deep into the surrounding rock is then fixed into the surrounding rock via epoxy resin. Both ends of the PVC pipe are sealed to avoid the reinforcement meter being interfered with by the vibrations caused by the pouring of concrete into the shaft lining; thus reducing the probability of the reinforcement meter being corroded by groundwater. This instrument has been used, and its reliability has been proven in the stress monitoring of the new main shaft at -1300 m and -1418 m levels within the Xin-Cheng gold mine [33].

4.2.2. Vibrating String Concrete Strain Gauge. The concrete strain monitoring sensor uses an embedded vibrating string concrete strain gauge. The standard measuring range of the embedded vibrating string concrete strain gauge is ±3000 $\mu\varepsilon$, and the working environment temperature is −25~80°C, confirmed with a temperature measuring function.

When the strain gauge is buried in concrete, the vibration frequency of the vibrating string in the strain gauge changes with the deformation of the concrete. The strain size of the strain gauge can be obtained by using the vibration frequency change of the vibrating string; thus, the strain change of the concrete can be measured. The strain calculation formula of the vibrating string strain gauge can be expressed as

$$\varepsilon = k\left(f_i^2 - f_0^2\right) + T_K\left(T_i - T_0\right), \quad (1)$$

where ε is the strain relative to the initial time, $\mu\varepsilon$; k is the conversion coefficient, $k = 2.48 \times 10^{-3}$; f_i is the output frequency, $\mu\varepsilon$; f_0 is the original frequency, $\mu\varepsilon$; T_K is the coefficient for temperature correction, $T_K = 2.2$; T_i is the temperature value at the time of measurement, °C; T_0 is tne initial temperature, °C.

4.3. Test Point Arrangement. Figure 6 illustrates the layout of the stress and strain monitoring points on the shaft lining from −1114 m to −1124 m of the air intake shaft and the ingate from −1120 m. Three measuring points were arranged at the arch and the left and right shoulders of the ingate at 1120 m. Three measuring points were arranged on the shaft lining connected with the ingate. The three measuring points on the shaft lining were all at the same level with the waistline of the ingate (−1117.7 m). One load bolt, one circumferential concrete strain gauge, and one axial concrete strain gauge were installed at each measuring point. Data collection was carried out after concrete pouring, and 3~4 groups of data were collected at each measuring point for a total of 30 days.

5. Results and Analysis

5.1. Stress Characteristics and Analysis of the HPC Shaft Lining at −1117.7 m Level. The shaft lining stress variation of the HPC at the −1117.7 m level is shown in Figure 7. The tensile stress of the shaft lining is positive, and the compressive stress is negative. It can be seen from Figure 7 that the interaction stresses between the high-performance concrete shaft lining and the surrounding rock are compressive stress at measurement points No. 1, 2, and 3 at −1117.7 m level. The shaft lining restricts the movement of the surrounding rock to the surface of the wellbore so that the interaction stress between the shaft lining and the surrounding rock is compressive. The stress of the surrounding rock is adjusted continuously, and the interaction stress between the shaft lining and surrounding rock is in a fluctuating state. During the monitoring period, the interaction stress at measuring point No. 1 is 0.029~0.056 MPa, the interaction stress at measuring point No. 2 is 0.016~0.038 MPa, and the interaction stress at measuring point No. 3 is 0.33~1.91 MPa.

The interaction stress between shaft lining and surrounding rock at −1117.7 m level of measuring point No. 3 increases slowly at first. After 18 days of high-performance concrete pouring, the interaction stress between shaft lining and surrounding rock at measuring point No. 3 increases rapidly and finally stabilizes at 1.8 MPa. The compressive

Figure 3: HPC after mixing.

Figure 4: HPC shaft lining after form stripping.

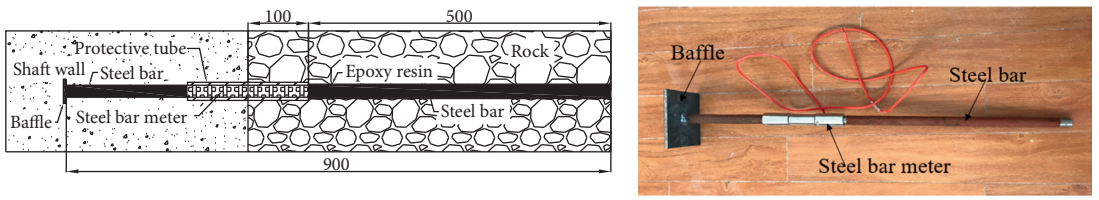

(a) (b)

Figure 5: The force-measuring anchor. (a) Monitoring diagram of the force-measuring anchor. (b) Image of the force-measuring anchor.

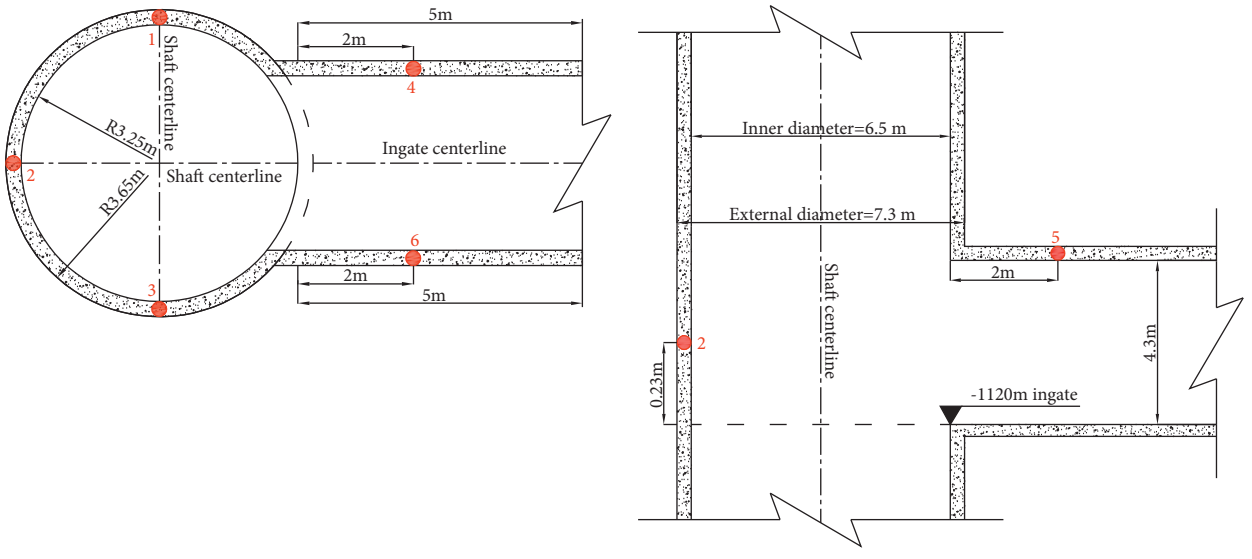

(a) (b)

Figure 6: Layout of measuring points.

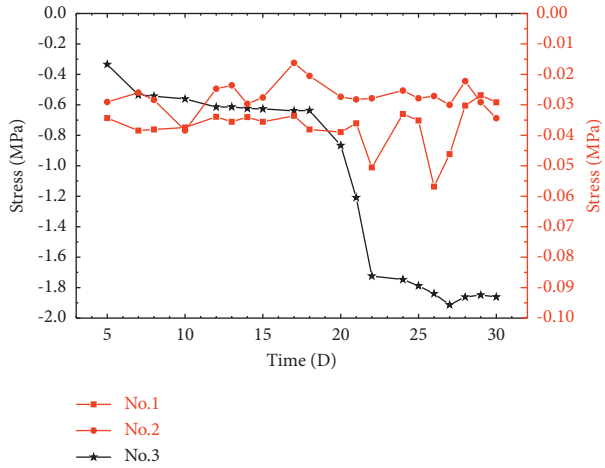

Figure 7: Variations of interaction stress between the horizontal shaft lining and the surrounding rock at the −1117.7 m shaft lining.

stresses between shaft lining and surrounding rock at measuring points No. 1 and 2 are small, and the maximum value is only 0.055 MPa. As can be seen from Figure 8, the circumferential strains of concrete at measuring points No. 1 and 2 are finally maintained at 500 $\mu\varepsilon$ and 600 $\mu\varepsilon$, respectively, which indicates that the surrounding rock at No. 1 and No. 2 has large deformation under the action of high in situ stress. Thus, the interaction stresses between shaft lining and surrounding rock at measuring points No. 1 and 2 should be larger because the surrounding rock produces higher circumferential stress to the shaft lining. However, the value of interaction stresses between shaft lining and surrounding rock at measuring points No. 1 and 2 is small, and the change law of interaction stress is not consistent with the strain evolution of concrete. The analysis shows that the hole diameter is too large when the force-measuring anchors were buried at measuring points No. 1 and 2. The lack of occlusion between the steel bar of the force anchor and the surrounding rock leads to the nonsynchronous movement which results in a small interaction stress between the surrounding rock and the shaft lining+.

5.1.1. Ultimate Stress of the High-Performance Concrete Shaft Lining at −1117.7 m Level. The calculation diagram of stress distribution of surrounding rock during circular shaft excavation is shown in Figure 9.

When $r = r_0$, the stress distribution of surrounding rock can be expressed as

$$\begin{aligned} \sigma_{rr} &= 0, \\ \sigma_{r\theta} &= P[(1+\lambda) - 2(1-\lambda)\cos 2\theta], \\ \tau_{r\theta} &= 0, \end{aligned} \tag{2}$$

where σ_{rr} is the rock radial stress, $\sigma_{r\theta}$ is the rock tangential stress, $\tau_{r\theta}$ is the rock shearing stress, P is the initial stress, and λ is the nonuniform coefficient.

Yu et al. according to the calculation diagram of stress distribution of surrounding rock during circular shaft excavation provided, the criterion for judging whether surrounding rock enters a plastic state is introduced [34]:

$$\sigma_{r\theta} = P[(1+\lambda) - 2(1-\lambda)\cos 2\theta] \geq R_c, \tag{3}$$

where R_c is the uniaxial compressive strength of rock.

According to equation (3), if the tangential stress of the surrounding rock is higher than the compressive strength of the rock, the surrounding rock enters the plastic state. Otherwise, the surrounding rock is in an elastic state. The measured maximum horizontal principal stress and minimum principal stress of Sha-ling gold mine at −1120 m are 35.9 MPa and 27.2 MPa, respectively, and the compressive strength of surrounding rock is about 90 MPa. Thus, the surrounding rock is in an elastic state after the vertical shaft −1120 m is excavated in the Sha-ling gold mine.

At present, there is no reasonable formula for determining the bearing capacity of the high-performance concrete shaft lining. The Von-Mises yield theory is adopted in the design code of the mine chamber in China. Therefore, based on the Von-Mises yield theory and thick-walled cylinder theory, the formula for calculating the ultimate bearing capacity of the high-performance concrete shaft lining is obtained. The Von-Mises strength criteria are as follows:

$$\sqrt{(\sigma_1 - \sigma_2)^2 + (\sigma_1 - \sigma_3)^2 + (\sigma_2 - \sigma_3)^2} \leq \sqrt{2} f_c, \tag{4}$$

where σ_1 is the first principal stress, σ_2 is the second principal stress, σ_3 is the third principal stress, and f_c is the axial compressive strength of concrete prism, MPa.

Assuming that the shaft lining is the homogeneous and continuous isotropic material, the stress solution of the shaft lining under the action of lateral pressure can be known from the stress law of the thick-walled cylinder [35]:

$$\begin{aligned} \sigma_{sr} &= -\frac{b^2 p_0}{b^2 - a^2}\left(1 - \frac{a^2}{r^2}\right), \\ \sigma_{s\theta} &= -\frac{b^2 p_0}{b^2 - a^2}\left(1 + \frac{a^2}{r^2}\right), \\ \sigma_{sz} &= \nu(\sigma_r + \sigma_\theta). \end{aligned} \tag{5}$$

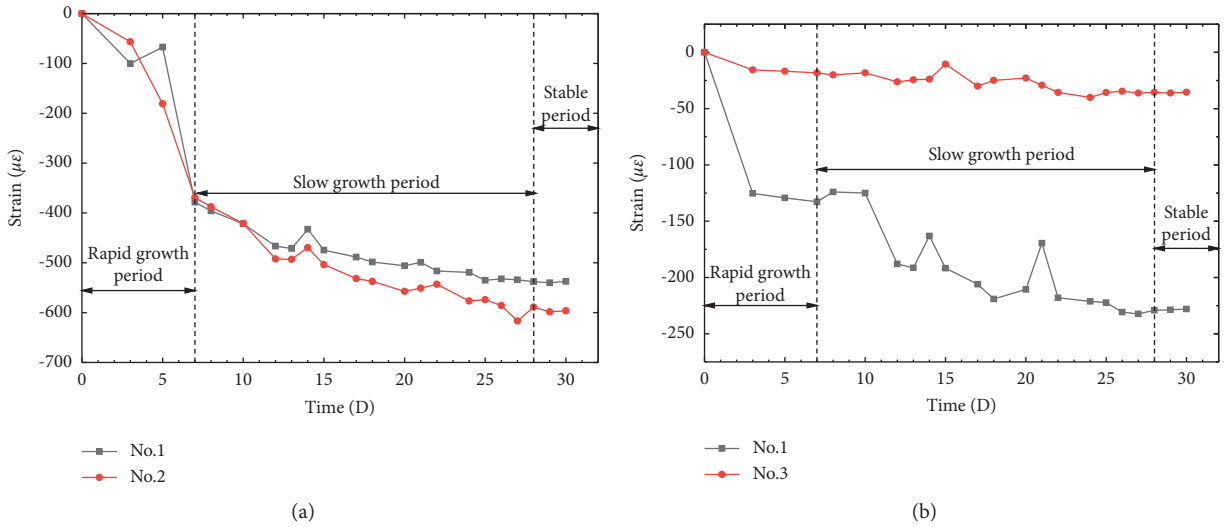

Figure 8: Strain variation of HPC at a depth of −1117.7 m. (a) Circumferential strain of HPC. (b) Axial strain of HPC.

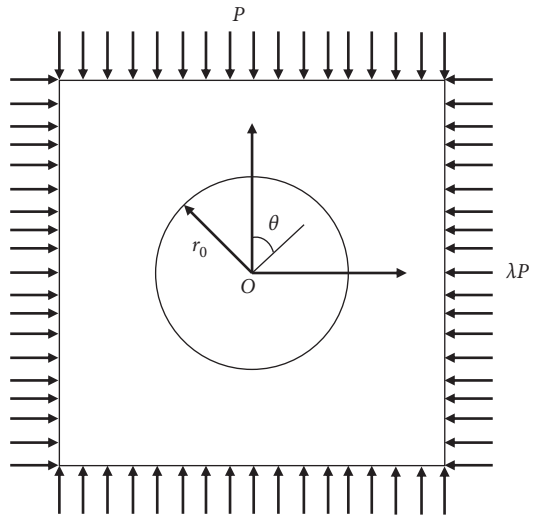

Figure 9: Stress calculation model of surrounding rock of circular shaft.

where a is the radius of inner shaft lining, b is the radius of external shaft lining, p_0 is the uniform external pressure on the shaft lining, σ_{sr} is the normal stress of shaft lining, $\sigma_{s\theta}$ is the circumferential stress shaft lining, σ_{sz} is the vertical stress shaft lining, ν is Poisson's ratio of concrete, and $\sigma_{sr} > \sigma_{sz} > \sigma_{s\theta}$.

Substituting equation (5) into the Von-Mises strength criterion equation (4), the stress of the concrete shaft lining can be decomposed as follows:

$$p_0 = \frac{f_c\left(b^2 - a^2\right)}{b^2\sqrt{3a^4/r^4 + 4\nu^2 - 4\nu + 1}}. \tag{6}$$

Neglecting the stress concentration of high-performance concrete, the shaft lining enters a plastic state at $r = a$. Therefore, the ultimate stress of the concrete shaft lining can be expressed as

$$p_0 = \frac{f_c\left(b^2 - a^2\right)}{b^2\sqrt{4\nu^2 - 4\nu + 4}}. \tag{7}$$

Poisson's ratio of high-performance concrete is 0.14~0.23 [36]. Poisson's ratio of high-performance concrete in this study is 0.2, and its uniaxial compressive strength is about 80 MPa. The radius of the inner shaft lining is $a = 3.25$ m, the radius of the external shaft lining is$b = 3.65$ m. Taking the above parameters into equation (7), the ultimate stress of the HPC shaft lining in the Sha-ling gold mine is 9.04 MPa.

During the monitoring period, the maximum stress at the measuring point No. 3 of the shaft lining at −1117.7 m level is 1.91 MPa. Obviously, the compressive stress of high-performance concrete shaft lining will not reach its limit stress, and the high-performance concrete shaft lining can

meet the support needs of metal mines in the complex environment of high in situ stress.

5.2. Stress Characteristics and Analysis of the HPC Shaft Lining at −1120 m Ingate. The interaction stresses between shaft lining and surrounding rock of the three measuring points at a depth of −1120 m of the ingate vault as well as the left and right arch shoulders are shown in Figure 10. The interaction stresses between the shaft lining and the surrounding rock at the three measuring points are tension stress which indicates that the shaft lining and the surrounding rock at the three measuring points of the ingate show the trend of tension or shear movement. The interaction stress between the shaft lining and surrounding rock of measuring point No. 4 is 0.61~1.73 MPa, the stress of measuring point No. 5 is 1.03~2.06 MPa, and the stress of measuring point No. 6 is 1.41~2.4 MPa.

The interaction stresses between the surrounding rock and the shaft lining of the three measuring points of the ingate's high-performance concrete shaft lining are tension. The analysis shows that it may be related to the distribution of stress fields in the Sha-ling gold mine. The maximum horizontal principal stress at −1120 m in the Sha-ling gold mine is 34.09 MPa, and the vertical principal stress is 29.65 MPa, which is 1.15 times that of the vertical principal stress. The maximum principal stress direction is near the NW direction. Influenced by the distribution of the in situ stress field in the Sha-ling gold mine construction area, the three measuring points of the ingate vault and the left and right shoulders were all subjected to tensile stress. The opening of the ingate air intake shaft within the Sha-ling gold mine is due south, and the angle with the direction of the maximum principal stress is approximately 45°. The vertical principal stresses at the arch and left and right shoulders of the ingate are less than the maximum horizontal principal stress. Therefore, the surrounding rock stress of the ingate under the maximum horizontal principal stress is higher than the surrounding rock stress under the vertical principal stress. With the excavation of the shaft, the surrounding rock at the vault and shoulder of the ingate is broken. With the stress adjustment, the surrounding rock at the vault and shoulder slips to both sides, and the acting stress of the surrounding rock on the shaft lining is mainly shear stress, causing the interaction stress between the shaft lining and the surrounding rock to be the pulling stress.

5.3. Strain Variation and Analysis of the HPC Shaft Lining at −1117.7 m Level. Figures 8(a) and 8(b) are the strain variation of the HPC shaft lining at −1117.7 m level. The axial concrete strain gauge at measuring point No. 2 and the circumferential concrete strain gauge at measuring point No. 3 are damaged, and no data was collected. Overall, the concrete strains at the three measuring points of the HPC shaft lining show a trend of first increasing and then stabilizing. The strain change can be divided into three periods: the rapid growth period, the slow growth period, and the stable period.

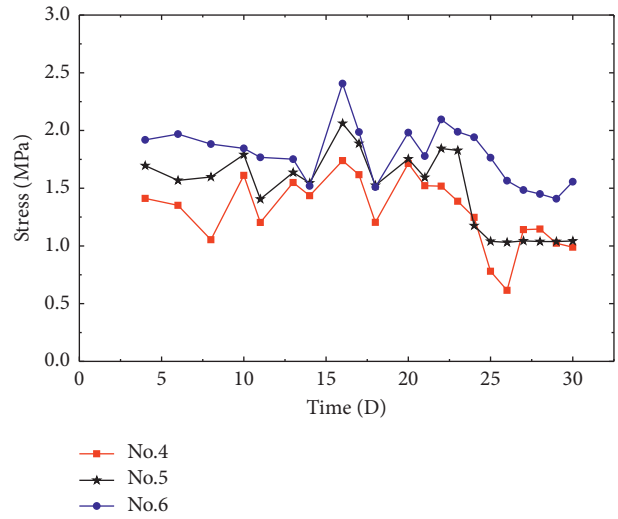

Figure 10: Variations of the interaction stress between the horizontal shaft lining and the surrounding rock at an ingate depth of −1120 m.

In the first seven days after HPC pouring, the circumferential strain at measuring point No. 1 reaches −378 $\mu\varepsilon$, which is 70% of the maximum strain during the monitoring period, and the circumferential strain at point No. 2 reaches −369 $\mu\varepsilon$, which is 60% of the maximum strain during the monitoring period. The axial strain of measuring point No. 1 reaches 132 $\mu\varepsilon$, which is 56% of its maximum strain during the monitoring period. The axial strain of measuring point No. 3 is −18 $\mu\varepsilon$, which is 45% of its maximum strain during the monitoring period. In the first seven days after high-performance concrete pouring, the strain growth rates of the three measuring points are more than 45%, and the strain of high-performance concrete is in the stage of a rapid period. After the casting of the HPC, under the constraint of the surrounding rock, the cementing material is hydrated. As the strength of concrete increases, the constraints of the surrounding rock increase leading to the fact that the strain of the concrete increases rapidly.

From the 8th day to the 28th day after high-performance concrete pouring, the strain growth rate of high-performance concrete decreases obviously. The circumferential strain of measuring point No. 1 increases from −378 $\mu\varepsilon$ to −537 $\mu\varepsilon$, increasing by 159 $\mu\varepsilon$; the circumferential strain of measuring point No. 2 increases from −369 $\mu\varepsilon$ to −588 $\mu\varepsilon$, increasing by 219 $\mu\varepsilon$; the axial strain of measuring point No. 1 increases from −132 $\mu\varepsilon$ to −229 $\mu\varepsilon$, increasing by 97 $\mu\varepsilon$; and the axial strain of measuring point No. 3 increases from −18 $\mu\varepsilon$ to −35 $\mu\varepsilon$, increasing by 17 $\mu\varepsilon$. From the 8th day to the 28th day after HPC pouring, the strain growth rate of HPC slows down obviously. The analysis shows that the hydration of high-performance concrete is basically completed in the first 7 days after pouring, the stiffness and strength of concrete are improved, and the deformation pressure of surrounding rock on shaft lining decreases which leads to the fact that the increasing trend of concrete strain slows down.

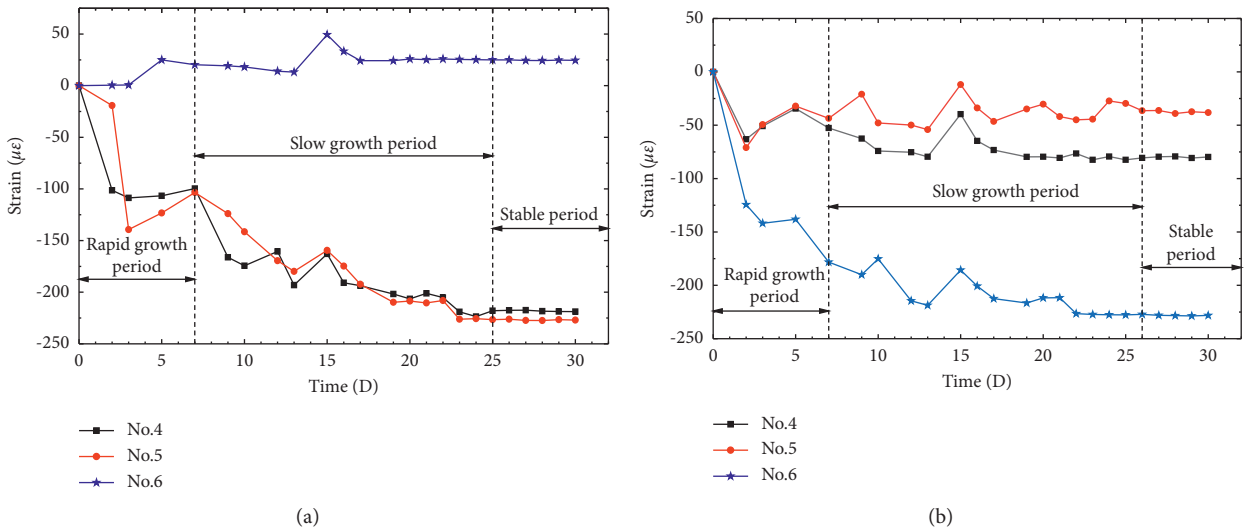

Figure 11: Strain variation of HPC for −1120 m ingate. (a) Circumferential strain of HPC for ingate. (b) Axial strain of HPC for ingate.

5.4. Strain Variation and Analysis of the HPC Shaft Lining at −1120 m Level. Figures 11(a) and 11(b) show the changes of the circumferential and axial strain of HPC at an ingate depth of −1120 m. As seen from Figure 11, the circumferential strains of HPC at measuring points No. 4 and No. 5 of the ingate are compressive, while the circumferential strain of the concrete at measuring point 6 is tensile. The axial strains of the HPC measuring points No. 4, 5, and 6 are all compressive strains. The strain variation law at −1120 m the HPC of the ingate is consistent with that of the −1117.7 m HPC shaft lining: the concrete strain increases rapidly from the completion of casting to the 7th day after the casting. The concrete strain increases slowly from the 8th day to the 28th day after the casting. After 28 days, the concrete strain is stable, and the strain does not change. Compared with the strain change of the shaft linings concrete at −1117.7 m, the strain growth rate at a depth of −1120 m ingate in the first 7 days is lower.

6. Discussion on the Application of the High-Performance Concrete Shaft Lining

The low impact liability of HPC is reflected in the uniform stress of the HPC shaft lining structure and the stable strain change of the HPC. Under the influence of high in situ stress and strong excavation disturbance, the stress of the HPC shaft lining is uniform, which reduces the stress concentration effect and cuts off the path of sudden energy release at a certain point in the concrete under the action of a concentrated stress. The strain change of the HPC shaft lining is stable, and there are no sharp strain increases or continuous fluctuations, indicating that the ability to accumulate elastic strain energy in HPC is poor.

The low impact liability of HPC shaft linings is related to three factors: (1) there are no coarse aggregates in the HPC, the concrete has good fluidity, and the scale of the internal fabric interface decreases, increasing the compactness of the concrete. (2) Steel fibers have a toughening effect on concrete. When steel fiber is added to the HPC, the concrete's ultimate stress and strain will increase. Simultaneously, the steel fibers are interwoven and bonded within the shaft lining, which effectively prevents the expansion of the cracks and slows down the development of microcracks in the concrete [37]. The friction effect of the interface between the fiber, the concrete, and the tension effect of the fiber itself weakens the deformation energy storage of the concrete. (3) The mixture of high-performance concrete contains fly ash and mineral powder. The addition of fly ash and mineral powder enhances the ability of concrete to resist creep and the strain change of concrete is stable.

High-performance concrete has the advantages of high strength, good durability, and small deformation. However, high-performance concrete also has the disadvantages of easy to appear surface cracks in the construction process and high cost compared with ordinary concrete. At the same time, with the increase of external temperature, the porosity and pore diameter of HPC continues to increase, the internal mesostructure deteriorates, and the compressive strength decreases [38]. The high ground temperature environment in deep strata also limits the wide application of the high-performance concrete shaft lining.

7. Conclusions

In this study, the in situ stress of the Sha-ling gold mine is measured and analyzed, the field application test of high-performance concrete shaft lining is carried out, and the strain variation law of high-performance concrete shaft lining is analyzed. Combined with the distribution of in situ stress and the change law of surrounding rock, the stress change characteristics of the shaft lining are analyzed. The conclusions are drawn:

(1) The maximum compressive stress of the HPC shaft lining structure at the level of −1117.7 m of the air intake shaft in the Sha-ling gold mine is 1.91 MPa, and the compressive stress of the high-performance

concrete shaft lining will not reach its limit stress. The HPC shaft lining can meet the complex supporting of the metal mine depth shaft in a coastal area.

(2) The maximum tensile stress of the HPC shaft lining at a depth of −1120 m of the ingate vault as well as the left and right arch shoulders is 2.4 MPa, which is influenced by the in situ stress distribution in the Sha-ling gold mine. The surrounding rock of −1120 m ingate is separated from the shaft lining which results in tensile stress in the ingate vault as well as the left and right arch shoulders.

(3) According to the measured strain data of the high-performance concrete shaft lining at −1117.7 m level and −1120 m ingate in Sha-ling gold mine, it can be seen that the strain change can be divided into three stages: the rapid growth period, the slow growth period, and the stable period. The circumferential strain growth rate of the HPC shaft lining is higher than the axial strain growth rate.

Data Availability

The monitoring data (Excel and origin) used to support the findings of this study are included within the article.

Conflicts of Interest

The authors declare that they have no conflicts of interest.

Acknowledgments

This work was supported by the State Key Research Development Program of China (Grant no. 2016YFC0600801) and Fundamental Research Funds for the Central Universities (06500229); The authors thank AiMi Academic Services (https://www.aimieditor.com) for English language editing and review services.

References

[1] M. C. He, H. P. Xie, P. Peng, and Y.-D. Jiang, "Study on rock mechanics in deep mining engineering," *Chinese Journal of Rock Mechanics and Engineering*, vol. 24, no. 16, pp. 2803–2813, 2005.

[2] L. Zhang, S. Z. Wang, and L. Q. Shi, "Strength characteristics of six kinds of rocks in China under high confining pressure," *Chinese Journal of Rock Mechanics and Engineering*, vol. 4, no. 1, pp. 10–19, 1985.

[3] H. W. Zhou, H. P. Xie, and J. P. Zuo, "Research progress of rock mechanical behavior under deep high ground stress," *Advance in Mechanics*, vol. 35, no. 1, pp. 91–99, 2005.

[4] C. Zhu, M.-c. He, B. Jiang, X.-z. Qin, Q. Yin, and Y. Zhou, "Numerical investigation on the fatigue failure characteristics of water-bearing sandstone under cyclic loading," *Journal of Mountain Science*, vol. 18, no. 12, pp. 3348–3365, 2021.

[5] M. Gao, J. Xie, Y. Gao et al., "Mechanical behavior of coal under different mining rates: A case study from laboratory experiments to field testing," *International Journal of Mining Science and Technology*, vol. 31, no. 5, pp. 825–841, 2021.

[6] D. H. Chen, H. E. Chen, W. Zhang, J. Lou, and B. Shan, "An analytical solution of equivalent elastic modulus considering confining stress and its variables sensitivity analysis for fractured rock masses," *Journal of Rock Mechanics and Geotechnical Engineering*, pp. 1674–7755, 2021.

[7] A. Leemann and R. Loser, "Analysis of concrete in a vertical ventilation shaft exposed to sulfate-containing groundwater for 45years," *Cement and Concrete Composites*, vol. 33, no. 1, pp. 74–83, 2011.

[8] E. Gruyaert, P. Van den Heede, M. Maes, and N. De Belie, "Investigation of the influence of blast-furnace slag on the resistance of concrete against organic acid or sulphate attack by means of accelerated degradation tests," *Cement and Concrete Research*, vol. 42, no. 1, pp. 173–185, 2012.

[9] Y.-c. Zhou, J.-h. Liu, S. Huang, H.-t. Yang, and H.-g. Ji, "Performance change of shaft lining concrete under simulated coastal ultra-deep mine environments," *Construction and Building Materials*, vol. 230, Article ID 116909, 2020.

[10] M. L. Nehdi, A. R. Suleiman, and A. M. Soliman, "Investigation of concrete exposed to dual sulfate attack," *Cement and Concrete Research*, vol. 64, pp. 42–53, 2014.

[11] M. F. Najjar, M. L. Nehdi, A. M. Soliman, and T. M. Azabi, "Damage mechanisms of two-stage concrete exposed to chemical and physical sulfate attack," *Construction and Building Materials*, vol. 137, pp. 141–152, 2017.

[12] Z. Zhang, X. Jin, and W. Luo, "Long-term behaviors of concrete under low-concentration sulfate attack subjected to natural variation of environmental climate conditions," *Cement and Concrete Research*, vol. 116, pp. 217–230, 2019.

[13] T. Aye and C. T. Oguchi, "Resistance of plain and blended cement mortars exposed to severe sulfate attacks," *Construction and Building Materials*, vol. 25, no. 6, pp. 2988–2996, 2011.

[14] C. Zhu, Z. Yan, Y. Lin, F. Xiong, and Z. Tao, "Design and application of a monitoring system for a deep railway foundation pit project," *IEEE Access*, vol. 7, pp. 107591–107601, 2019.

[15] Z. Dou, Y. Liu, X. Zhang et al., "Influence of layer transition zone on rainfall-induced instability of multilayered slope," *Lithosphere*, vol. 2021, no. 4, Article ID 2277284, 2021.

[16] C. Cao, W. Zhang, J. Chen, B. Shan, S. Song, and J. Zhan, "Quantitative estimation of debris flow source materials by integrating multi-source data: A case study," *Engineering Geology*, vol. 291, Article ID 106222, 2021.

[17] Z. Dou, S. Tang, X. Zhang et al., "Influence of shear displacement on fluid flow and solute transport in a 3D rough fracture," *Lithosphere*, vol. 2021, no. 4, Article ID 1569736, 2021.

[18] X. M. Zhou, G. Q. Zhou, Q. S. Hu, and C. Ma, "Model test research on shaft lining built in high pressure rock aquifer," *Chinese Journal of Rock Mechanics and Engineering*, vol. 30, no. 12, pp. 2514–2522, 2011.

[19] Z. S. Yao, G. H. Yu, H. Cheng, and C. X. Rong, "Research on vertical bearing capacity of shaft lining structure of high strength concrete and double steel cylinders in super-thick alluvium," *Rock and Soil Mechanics*, vol. 31, no. 6, pp. 1687–1691, 2010.

[20] Z. S. Yao, H. Cheng, and C. X. Rong, "Experimental study on shift-boring lining of high performance concrete and double steel cylinder in super-deep alluvium," *Chinese Journal of Rock Mechanics and Engineering*, vol. 26, no. S2, pp. 4264–4269, 2007.

[21] Z. S. Yao, H. Chen, and X. B. Ju, "Research and application of high strength steel fiber concrete compound shaft lining with

inner steel plate in deep alluvium shaft repair," *Journal of China Coal Society*, vol. 42, no. 9, pp. 2295–2301, 2017.

[22] C. X. Rong, X. X. Wang, and H. Cheng, "Research on mechanical characteristics of high-strength reinforced concrete shaft lining in deep alluvium," *Chinese Journal of Rock Mechanics and Engineering*, vol. 27, no. S1, pp. 2841–2847, 2008.

[23] Z. S. Yao, "An experimental study on steel fiber reinforced high strength concrete shaft lining in deep alluvium," *Chinese Journal of Rock Mechanics and Engineering*, vol. 24, no. 7, pp. 1253–1258, 2005.

[24] T. Han, W. H. Yang, and Y. L. Ren, "Horizontal ultimate bearing capacity of encased steel concrete shaft lining," *Journal of Mining and Safety Engineering*, vol. 28, no. 2, pp. 181–186, 2011.

[25] B. D. Ding, Z. Y. Han, G. C. Zhang, X. Beng, and Y. Yang, "Flexural toppling mechanism and stability analysis of an anti-dip rock slope," *Rock Mechanics and Rock Engineering*, vol. 54, no. 1, pp. 1–15, 2021.

[26] G. S. Zhao, M. H. Ren, X. H. Qiu, and Q. Xue, "The unified strength theory for plastic limit load analysis of vertical shaft lining," *Advances in Civil Engineering*, vol. 2018, Article ID 1949324, 8 pages, 2018.

[27] X. Z. Lyu and W. M. Wang, "Deformation monitoring and stability analysis of shaft lining in weakly cemented stratum," *Advances in Civil Engineering*, vol. 2018, Article ID 8462746, 18 pages, 2018.

[28] G. Li, Y. Hu, S.-m. Tian, M. weibin, and H.-l. Huang, "Analysis of deformation control mechanism of prestressed anchor on jointed soft rock in large cross-section tunnel," *Bulletin of Engineering Geology and the Environment*, vol. 80, no. 12, pp. 9089–9103, 2021.

[29] J. H. Liu, R. D. Wu, and Y. C. Zhou, "Experiment of bursting liability of deep underground concrete under complex stress conditions," *Journal of China Coal Society*, vol. 43, no. 1, pp. 79–86, 2018.

[30] M. Z. Gao, H. C. Hao, S. N. Xue, L. Tong, and C. Pengfei, "Discing behavior and mechanism of cores extracted from Songke-2 well at depths below 4,500 m," *International Journal of Rock Mechanics and Mining Sciences*, vol. 149, Article ID 104976, 2022.

[31] H. Peng, X. M. Ma, J. J. Jiang, and L. Peng, "Research on stress field and hydraulic fracturing in-situ stress measurement of 1 000 M deep hole in Zhao-Lou coal mine," *Chinese Journal of Rock Mechanics and Engineering*, vol. 30, no. 8, pp. 1638–1645, 2011.

[32] Y. C. Zhou, J. H. Liu, and H. G. Ji, "Study on bursting liability of fiber reinforced shaft lining concrete based on temperature and compound salt," *Materials Reports*, vol. 33, no. 16, pp. 2671–2676, 2019.

[33] H. G. Ji, D. L. Quan, and X. B. Su, "Influence of grouting on stability of supporting structure in deep roadway intersection area," *Journal of Mining and Safety Engineering*, vol. 38, no. 5, pp. 929–936, 2021.

[34] X. F. Yu, Y. R. Zheng, and H. H. Liu, *Stability Analysis of Surrounding Rock Of Underground Engineering*, coal Industry Press, Beijing, China, 1980.

[35] M. W. Lu and X. F. Luo, *The theoretical Basis Of Elasticity*, Tsinghua University Press, Beijing, China, 2001.

[36] Y. F. Wang and Y. P. Liang, "Study on modulus of elasticity and Poisson ratio of high performance concrete," *Journal of Beijing Jiao Tong University*, vol. 28, no. 1, pp. 5–7, 2004.

[37] Y. S. Liu, X. J. Wang, and T. Jin, "Study on the mechanical properties and constitutive relation of steel fiber reinforced concrete," *Journal of University of Science and Technology of China*, vol. 37, no. 7, pp. 717–723, 2007.

[38] H. X. Du and Y. N. Fan, "Meso-structure damage of C60 high performance concrete at high temperature on X-CT," *Journal of Building Materials*, vol. 23, no. 1, pp. 210–215, 2020.

Hindawi
Advances in Materials Science and Engineering
Volume 2022, Article ID 6494812, 11 pages
https://doi.org/10.1155/2022/6494812

Research Article

Predicting the Remaining Service Life of Civil Airport Runway considering Reliability and Damage Accumulation

Baoli Wei [1,2] **and Chengchao Guo** [3]

[1]*School of Civil Engineering and Architecture, Zhengzhou University of Aeronautics, Zhengzhou 450046, China*
[2]*School of Water Conservancy and Environment, Zhengzhou University, Zhengzhou 450001, China*
[3]*School of Civil Engineering, Sun Yat-Sen University, Zhuhai 519082, China*

Correspondence should be addressed to Baoli Wei; bdgway@yeah.net

Received 25 November 2021; Revised 16 December 2021; Accepted 18 December 2021; Published 17 January 2022

Academic Editor: REN Fuqiang

Copyright © 2022 Baoli Wei and Chengchao Guo. This is an open access article distributed under the Creative Commons Attribution License, which permits unrestricted use, distribution, and reproduction in any medium, provided the original work is properly cited.

Based on the MEPDG method, the operation process of MEPDG was analyzed and the MEPDG correction method applied to the remaining life prediction of airport pavement was obtained. According to the theory of structural reliability, the performance function of airport pavement was obtained based on the limit state equation represented by flexural stress. Considering the characteristics of airport cement concrete pavement design, the calculation formula of the number of allowable load actions was obtained based on reliability by NCHRP126 fatigue equation without considering the temperature stress when the flexural fatigue strength of pavement plate cement concrete was less than 1.25 times of the design strength. Based on the actual situation of local civil airport runways in Henan Province, the proposed MEPDG correction method was used to analyze the flexural stress of the actual operating airport runway pavement at 95% reliability level based on the mechanical numerical model of airport runway, and the number of allowable load actions of three aircraft models was obtained. Given the impact of pass-to-coverage ratio P/C, the cumulative damage factor CDF of the major aircraft models was calculated; the annual average growth rate of different aircraft models in the airport pavement evaluation stage was obtained based on the trend extension method. According to the predicted average annual cumulative damage, the remaining life of pavement was predicted. Compared with the actual conditions of the airport, the remaining life predicted in this paper was consistent with the actual life, which verifies the effect of the prediction of the remaining life of airport runway considering the impact of reliability and damage accumulation.

1. Introduction

In the mid-20th century, the airport management department for the airport runway only proposed "a palliative rather than a cure" for the operation and maintenance. In the early 10 years of the 21st century, the airport management department cast away the passive postmaintenance and adopted the preventive maintenance, a more active maintenance, to reduce the frequency of damage. Preventive maintenance is a time-based maintenance, but it will cause runway maintenance in an uneven manner: the consistent maintenance cycle will lead to unnecessary maintenance in some pavements but improper maintenance in other pavements. Also, the preventive maintenance is up to the expertise of technicians and is the lack of data support.

Currently, predictive maintenance (PdM), which emerges in many sectors, especially industry, is a typical way of intelligent maintenance. As a data-driven maintenance mode, it is an integration of sensor technology, signal processing technology, reliability analysis, statistics, machine learning, and other methods for determining potential diseases, which lays a foundation for a more reasonable and effective maintenance plan [1] Remaining Service Life (RSL) can be used by civil engineers to schedule maintenance times, optimize operational efficiency, and avoid unplanned stops. Therefore, predicting RSL should be prioritized in the predictive maintenance.

Therefore, in this paper, the remaining life prediction method of the airport runway was analyzed. The operation process of MEPDG was analyzed and summarized, and the MEPDG correction method was applied to the remaining life prediction of the airport runway. MEPDG provides technical support for the maintenance decision of airport runway and also provides reference for reasonable allocation of limited operation and maintenance funds in the airport management department [2].

2. Current Research Studies on the Remaining Life Prediction of Airport Pavement

The input in the RSL prediction model is the state indicator of airport runway. The features are taken from the monitoring sensor data or daily maintenance data, and behavior changes with runway performance degradation or usage state changes, but the changes can be predicted based on the model. RSL prediction methods applied to predictive maintenance can be divided into three categories: similarity prediction, performance degradation model prediction, and survival curve prediction methods.

At present, as a representative method, the similarity prediction method is the constrained polynomial regression model proposed by American scholar Shahin [3]. This model is very practical. It has been incorporated into the Micro-Paver system [4] and has been widely used in countries around the world. In addition, the two-parameter nonlinear model created by Chinese scholar Sun Lijun is widely used in China [5]. At the same time, many researchers have studied the similarity prediction methods [6–9].

To study the performance degradation model based on the prediction method for the remaining life prediction of airport runway, most scholars at home and abroad fit a general fatigue equation using the site or laboratory data from performance degradation equation of a linear or exponential function. Then, they use the fatigue equation as the performance degradation model for predicting the future performance degradation process of airport runway, to further predict the remaining life of airport runway. For example, Ji and Sheng [10] took the design program FAARFIELD [11] as the analysis tool and predicted the remaining life of pavement using data by FAARFIELD with the back-calculated airport concrete pavement modulus as the prediction index. Taking the cumulative damage as the status indicator, Zhao et al. proposed the estimation method for the remaining life of flexible airport pavement and carried out case analysis [12].

Lytton applied the survival curve in highway engineering [13]. According to Lytton, the survival curve is mostly used for design of pavement maintenance and reconstruction scheme in the road network. In the performance prediction for a single section, the distribution function (i.e., survival function) is used to conduct life analysis and prediction based on preset pavement performance. Mishalani and Madanat [14]; Yang et al. [15]; and Kobayashi et al. [16] conducted a survival curve analysis according to the data of pavement performance failure, cracks in reinforced concrete bridge deck, and full cycle life cost of pavement and pointed out that the survival curve prediction analysis may be feasible for pavement engineering.

Based on the above analysis, as the remaining life prediction of airport pavement is quite complicated, scholars at home and abroad used different methods to predict the changes of pavement performance, or established suitable statistical prediction models based on the survey results of pavement performance. However, most of the methods failed to take the actual maintenance of pavement into consideration and the model only had the theoretical significance rather than could be applicable to the actual service pavement. Also, they failed to consider the reliability of service pavement and the impact of damage accumulation. In fact, there are many factors that affect the service life of airport runways, such as airport flight traffic loading, runway structural characteristics, and the level of field maintenance technology, all of which affect the remaining service life of runways. Therefore, this paper proposes a prediction method that can be used in practical engineering projects to address the effects of airport flight traffic load, runway structural characteristics, and maintenance technology level on the remaining service life.

3. MEPDG Correction for the Remaining Life Prediction of Airport Runway

3.1. Operation Process of MEPDG. Mechanistic-Empirical Pavement Design Guide (MEPDG) aims to provide a design and analysis method for newly built and repaired pavements based on the mechanistic-empirical principle [17].

The design method in MEPDG includes three phases. The first phase is to develop input values. The design requirements objectives are identified, basic analysis is conducted, and the characteristics data are taken as input, including the data for pavement material, the characteristics data of traffic, and the hourly climate data of weather station (temperature, precipitation, solar radiation, cloud cover, and wind speed). In the second phase, structural and performance analysis is conducted. An initial test design value is chosen and analyzed based on the relationship model between pavement response and damage (generally an expression over time). The output of the analysis is the cumulative damage and flatness over time. Based on the iteration, the predicted performance with the design indicators of multiple predicted damages has been compared until all the design indicators meet the specified reliability requirements, and the required pavement can be obtained. The third phase is to evaluate the structurally feasible alternatives, such as engineering analysis and life cycle cost analysis.

3.2. Flowchart of MEPDG Correction. Given the reliability of runway, the pass-to-coverage ratio (P/C) of aircraft model, and the cumulative damage of airport runway, MEPDG correction was needed for predicting the remaining life of airport runway. The flowchart of MEPDG correction is shown in Figure 1.

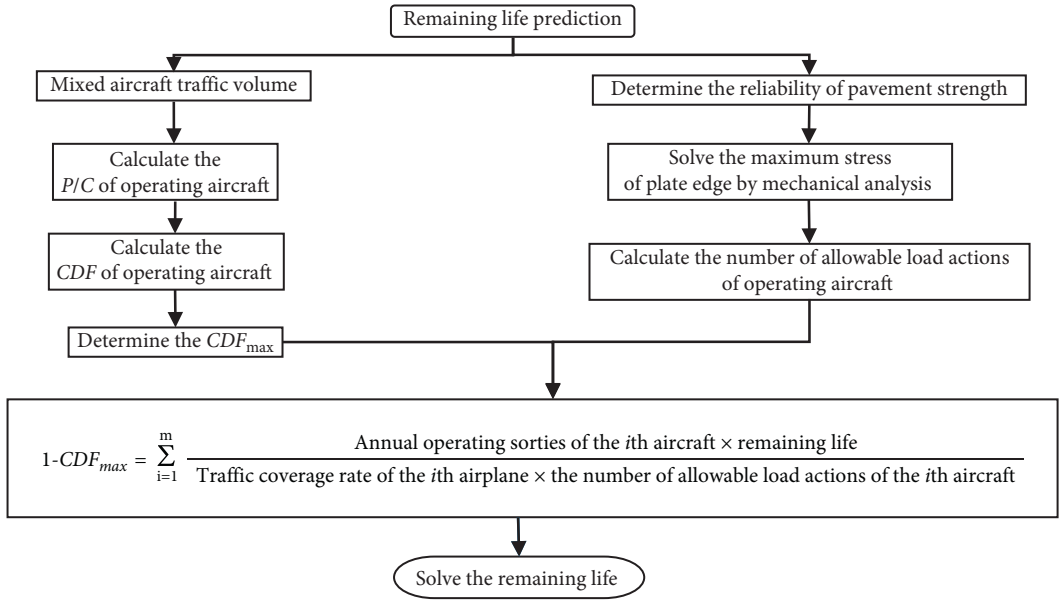

Note: P/C in the figure was the pass-to-coverage ratio, and CDF was the cumulative damage factor.

Figure 1: Flowchart of MEPDG correction for the remaining life prediction of airport runway.

3.3. Analysis of the Strength Reliability of the Cement Concrete of Airport Runway Pavement. According to the *Specification for Design of Highway Cement Concrete Pavement*, and based on the structural characteristics of airport runway pavement, its strength reliability was explained as follows: based on the specified time and conditions, the actual probability that pavement played a specific function was obtained, as shown in the following formula [18]:

$$P_r = P\left(\sigma_{\text{pr}} + \sigma_{\text{tr}} \le f_{\text{rm}}\right), \tag{1}$$

where P_r was the reliability achieved by the pavement; σ_{pr} meant the fatigue stress of the pavement plate under the action of aircraft load (unit: MPa); σ_{tr} meant the flexural stress of pavement plate caused by temperature; and f_{rm} referred to the standard value of flexural-tensile strength of cement concrete (unit: MPa).

The corresponding function was obtained based on the limit state equation corresponding to the flexural-tensile stress, which was shown in the following formula:

$$Z = f_{rm} - \left(\sigma_{pr} + \sigma_{tr}\right). \tag{2}$$

In this paper, the strength reliability of cement concrete of airport runway pavement needed to follow Formula (2). As the temperature and fatigue stress of cement concrete were closely related to the fatigue stress of aircraft load, the interference theory had nothing to do with and cannot help solve the strength reliability. In this paper, the control failure mode was assumed to remain constant and then a reliability analysis was conducted. According to the *Specification for Design of Highway Cement Concrete Pavement* and based on the different airport cement concrete pavement design and the literature proposed by Cai [19], lg (N) was obtained, as shown in the following formula by NCHRP126 fatigue equation:

$$\lg(N) = \begin{cases} -1.7136e + 4.284 & e > 1.25 \\ 2.812e^{-1.2214} & e \le 1.25 \end{cases}, \tag{3}$$

$$e = \frac{f_{\text{rm}}}{f_{\text{cm}}}, \tag{4}$$

where N was the number of coverages at 50% pavement plate cracking, namely, the fatigue life of pavement plate; e referred to the stress ratio; f_{rm} was the flexural-tensile fatigue strength of concrete; and f_{cm} meant the concrete design strength of pavement.

To make the calculation procedure simple and easy to use, the fatigue equation for temperature stress was not considered in the analysis of fatigue life.

According to the design documents and the design specifications, the flexural-tensile fatigue strength of the concrete of pavement plate usually shall be less than 1.25 f_{cm} under aircraft load and temperature. The formula of f_{rm} was obtained by Formula (4), shown as follows:

$$f_{\text{rm}} = f_{\text{cm}} \cdot \left(\frac{2.812}{\lg(N)}\right)^{0.8187}. \tag{5}$$

By substituting Formula (5) into Formula (2), the performance function Z was transformed into the following formula:

$$Z = f_{cm} \cdot \left(\frac{2.812}{\lg(N)}\right)^{0.8187} - \sigma_{\text{pr}}. \tag{6}$$

3.4. Calculation Principle behind the Cumulative Damage of Airport Runway. According to studies, aircraft wheel track is almost distributed in a normal manner when the aircraft

takes off and lands. A pass of the aircraft wheel through the maximum stress point on the pavement was called a coverage. The ratio of the number of passes required to apply a full load on the pavement of unit area was expressed as the P/C.

The statistical analysis was conducted on the distribution data of measured aircraft track, and the number of coverages was calculated based on the P/C of aircraft on the pavement. Figure 2 (schematic diagram of the calculation of P/C) shows the area between $f(x)$ and x axis; that is, the number of coverages during the actual operating of aircraft was equal to l, and the area of W_t was $C_x W_t$. Thus, the calculation formula of the P/C of single-wheel aircraft was as follows [20]: where P/C was the pass-to-coverage ratio; C_x referred to the track probability density of operating aircraft at x coordinate; and W_t meant the effective tire contact width of aircraft, which was selected based on the design parameters of aircraft.

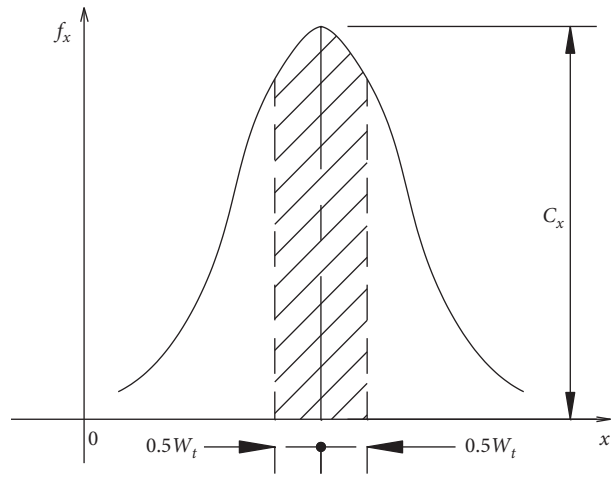

Figure 2: Schematic diagram of the calculation of P/C.

$$\frac{P}{C} = \frac{1}{C_x W_t}, \tag{7}$$

In the airport pavement design, Miners law is widely used to show the linear cumulative fatigue damage, which can be expressed by the cumulative damage factor (CDF). As the fatigue life of pavement was expressed as the number of allowable load action repetitions, the CDF stood for the fatigue life for pavement that has been used [21]. It was equal to the ratio of the current number of actual cumulative actions on the pavement plate and the number of allowable load action repetitions of the ith aircraft (the number of load action repetitions till pavement damage).

4. Analysis on Engineering Application Case

This paper selected the civil Airport A's runway in Henan for the case study. This airport was the Chinese trunk transport airport and a national first-class aviation port. In 2016, the passenger throughput of the airport ranked the 15th among civil airports in China. The airport was opened to traffic in 1997, and its south flight area has been used for 22 years in 2017. The south runway of the airport was 3,400 m long and 45 m wide, to grasp the comprehensive situation of the pavement in the flight area and learn about the basic information about the recent management and renovation plan of the area; the airport management department conducted comprehensive testing on the pavement of runway, taxiway, and contact surfaces in the south flight area of the airport in 2007, 2013, and 2017, respectively. The department conducted comprehensive analyses of the field test data to form a high-value database. According to the remaining life prediction process of airport runway (shown in Figure 1), the prediction for RSL of Airport A was established to verify the feasibility and implementation effect of MEPDG correction method.

4.1. Calculation on the Number of Allowable Load Actions Based on the Strength Reliability of Airport Pavement Cement Concrete. Based on the actual demands and according to the statistics of Airport A in 2017, the statistical table of the annual takeoff and landing sorties of operating aircraft at Airport A is shown in Table 1. According to Table 1, when it comes to the determination of aircraft load simulation, Boeing B737-800, Airbus A320, and Boeing B737-700 were taken into consideration in 2017.

According to the reliability calculation method under Section 3.3, the distribution type and distribution parameters of each input variable need to be defined in the reliability analysis model. Based on the literature proposed by Zhang [22] and Gao [23], and given the actual conditions of airport runway, the actual thickness of pavement plate, the response modulus of base course, the flexural-tensile design strength, and flexural-tensile modulus of surface course concrete were determined as the random variables of airport runway in this paper. The following showed the determination of the statistical properties of the random variables.

4.1.1. Determination on the Actual Thickness of Cement Concrete Pavement Plate. The radar detection of pavement was adopted to measure the thickness of surface layer of south runway pavement. The radar detection results of typical section are shown in Figure 3. The measured thickness of surface course of south runway pavement is shown in Table 2.

Based on Table 2, the measured thickness of surface layer of both ends of south runway pavement exceeded 37.5 cm, fully meeting the requirement for design thickness. Based on this table, the mean thickness of surface layer of south runway pavement was determined to be 38 cm, and the coefficient of variation was 0.03 in this paper.

4.1.2. Determination on the Modulus of Base Reaction. This paper adopted an HWD for the detection around the center of the plate. Based on the obtained HWD data and the actual pavement structure, the modulus of subgrade reaction was calculated. The back-calculated results are shown in Table 3.

Table 1: Statistical table of the annual takeoff and landing sorties of operating aircraft of Airport A.

Aircraft	Annual takeoff and landing sortie	Annual takeoff and landing ratio (%)	Notes
B737-800	38121	51.40	Main model
A320	17425	23.50	Main model
B737-700	4223	5.70	Main model
A319	3493	4.70	
B737-300	2135	2.90	
A321	2004	2.70	
ERJ-190	1679	2.30	Secondary models, with ratio less than 5%
B747-400	1211	1.60	
MA60	870	1.20	
Others	3064	4.10	

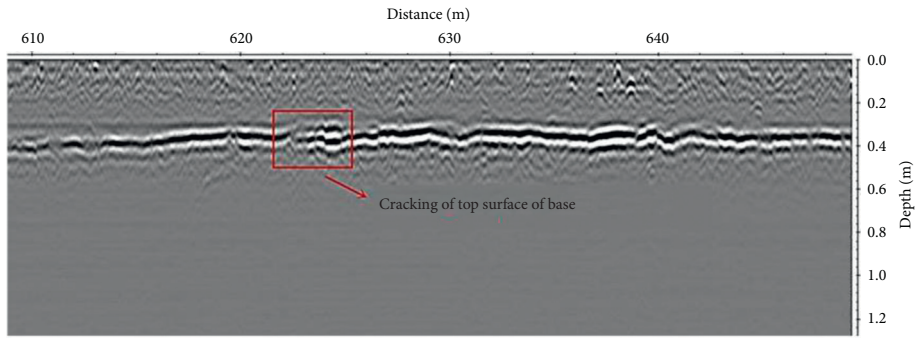

Figure 3: Radar detection results of typical section.

Table 2: Comparison between the measured thickness of runway pavement surface layer and the design thickness.

Section	Position (m)	Number of sample (pcs)	Full-thickness mean (cm)	Standard deviation (cm)	Representative value (cm)	Design value (cm)
South runway	0–500 m	500	38.18	1.32	38.08	38
	500–2900 m	2400	34.01	1.79	33.95	34
	2900–3400 m	500	38.06	1.7	37.93	38

Table 3: Calculation table of the modulus of the subgrade reaction and the base reaction of south runway pavement.

Zone (m)		Modulus of subgrade reaction (MN/m^3)	Equivalent thickness of base course (cm)	Modulus of base reaction (MN/m^3)
Runway	0–500	58	48	104
	500–2900	52	48	100
	2900–3400	47	48	95

The pavement foundation comes from the compacted pavement bed soil, and the pavement foundation modulus is often affected by the material properties. It is worth noting that the environmental factors directly affect the performance of the pavement foundation, and the significant differences in soil quality also directly affect varied characteristics of pavement foundation. Considering the above factors and the variation coefficient in the literature proposed by Li [24], the variation coefficient of the modulus of base reaction was set as 0.3.

4.1.3. Determination on the Flexural Strength and the Elastic Modulus of Airport Runway Cement Concrete. The sampling scheme of pavement core was as follows: in the south runway, a total of 18 core samples were drilled alternately every 180 m along both sides of the centerline. The drilled cement concrete core samples shall be subject to the splitting tensile strength test according to the *Technical Specification for Construction of Cement Concrete Surface of Civil Airport*. The test results of the drilled cement concrete core samples are shown in Table 4. The section structures of typical cement concrete core samples after the test are shown in Figure 4.

According to Table 4, the mean of the flexural strength of cement concrete of runway pavement surface course was 5.78 MPa, and the coefficient of variation was 0.15; the mean of the flexural elastic modulus was 38,537.77 MPa, and the coefficient of variation was 0.09. Given the fact that the airport pavement cement concrete has been used for nearly

Table 4: Tensile strength test results of the cement concrete core samples of runway pavement.

Core sample no.	Test piece diameter (mm)/ height (mm)	Failure load (kN)	Splitting strength (MPa)	Flexural strength (MPa)	Flexural elastic modulus (MPa)
1#	147.5/203	139.807	2.97	4.82	34342.65
2#	147.5/198	161.641	3.52	5.59	37922.91
3#	147.5/199	197.105	4.27	6.62	42192.64
4#	147.5/201	175.513	3.77	5.93	39387.19
5#	147/301	211.352	3.04	4.92	34811.10
6#	147.5/299	279.592	4.04	6.3	40901.97
7#	147.5/302	202.168	2.89	4.71	33763.08
8#*	147/301	285.587	4.11	6.4	41302.77
9#	146.5/299	201.403	2.93	4.76	34027.75
10#	147/300	262.883	3.79	5.97	39539.02
11#	148/298	303.461	4.38	6.76	42743.19
12#	148/297	337.33	4.89	7.44	45241.95
13#*	148/301	324.969	4.64	7.12	44075.51
14#	147.5/298	307.293	4.45	6.86	43104.91
15#	148/298	283.163	4.09	6.37	41184.52
16#	147.5/300	236.735	3.41	5.43	37193.95
17#*	147.5/298	194.210	2.81	4.6	33220.36
18#	148/302	224.617	3.2	5.14	35868.57
Mean (MPa)				5.78	38537.77
Standard deviation (MPa)				0.84	3605.52
Representative value at 95% guarantee rate (MPa)				5.39	36897.26

Note. The 8 #, 13 #, and 17 # core samples were not completely split, so their data were discarded in this calculation.

(a) (b)

Figure 4: Section structures of typical cement concrete core samples after the splitting tensile strength test. (a) Core sample # 7. (b) Core sample # 12.

20 years and for the sake of design safety, the mean of the flexural strength of cement concrete of runway pavement surface course was set as 4.50 MPa, and the coefficient of variation took 0.15.

4.1.4. Number of Allowable Load Actions of the Cement Concrete Runway of the Operating Airport. According to the calculation method of reliability under Section 3.3 mentioned above, the distribution parameters of input variables were defined. The thickness of surface course, the strength and modulus of surface course, and the modulus of base reaction were regarded as random variables. Except for the distribution of the modulus of base reaction which was in logarithmic normal distribution, the other random variables tended to be in normal distribution.

The semirigid base of that airport runway pavement is likely to crack and lead to the damage of the base. At the same time, the coefficient of variation will increase. These problems generally occur in the early stage of the runway. Therefore, the random variables of runway were set according to the actual detection values described above. Based on the literature proposed by Guo [25] and Gao [26], the appropriate interval for coefficient of variation was set; the scientific and effective quality control was generally made on the surface course during construction; the base showed significant deformation. The mean and coefficient of variation of the random variables are shown in Table 5.

Take the load of twin-wheel B737-800 as an example. The load was distributed in the middle of the cross-seam edge of pavement plate because of the spacing of wheels. Based on the target reliability of II, III, and IV airports in the literature proposed by Li [27], the target reliability was set to 95%. By inputting the target reliability into the numerical analysis program, the allowable action times of B737-800 aircraft acting on the pavement were calculated. The specific results are as follows.

In general, the response surface method for reliability analysis does not experience many cycles and can be analyzed in low probability. The fitting coefficient can represent the approximation between the actual response values, and can inform the users to update the definition parameters with the poor effect of the fitting of approximate function, so it is ideal for parallel processing. Thus, when calculating reliability, this paper used the Box–Behnken matrix sampling of response surface method for analyzing probability [28]. The precision test of response surface followed the formula as [29]

$$R^2 = \frac{\sum_{i=1}^{n} \left(\widehat{y}_i - \overline{y}\right)^2}{\sum_{i=1}^{n} \left(y_i - \overline{y}\right)^2}, \tag{8}$$

where $\widehat{y}_i$ was the calculation value of response surface model; y_i referred to the true value (calculation result of finite element analysis); and $\overline{y}$ was the average value corresponding to true value. R^2 ranged from 0-1. If R^2 was large, the regression model will be more fit with the actual case.

Based on the square response surface regression results, the comparison between the response surface estimation value and the finite element true value was made, as shown in Figure 5. As can be seen from Figure 5, except for the individual data points, the other data points were distributed near the 45° line, which indicated that there was good fitting between the response surface estimation value and the finite element true value.

For the response surface functions that have been fitted, the Monte-Carlo method was used for 10,000 times of sampling and a series of performance function corresponding to the sampling value distribution diagram was obtained (see Figures 6 and 7 for details). Due to the limited space, the following only listed the figure of performance functions during the B738 load action.

As can be seen from Figures 6 and 7, sampling based on the response surface function will achieve excellent convergence. Thus, the number of samples was set to 10^4 to meet the preproposed reliability standard. At this point, the failure probability reached $P_f = 5.412 \times 10^{-2}$, and z at 95% target reliability was 0.476 Mpa. By substituting it into Formula (5), the number (N) of allowable load actions of B738 meeting 95% target reliability was 133,195. Similarly, 4,175,184 times of allowable load actions of A320 and 477,806 times of allowable load actions of B737-700 met 95% target reliability, respectively.

4.2. Calculation of Airport Pavement CDF and the RSL Prediction Based on P/C. As mentioned above, the B737-800, A320, and B737-700 were the major aircraft of Airport A since the calculation of CDF needed the number of coverages of aircraft loads, which must be converted through the takeoff and landing sorties of different aircraft by means of P/C. So, separate calculation was required for the major aircraft of Airport A. Because the runway cumulative damage factor CDF is calculated based on the number of aircraft load coverage, and the number of aircraft load coverage needs to be converted by the number of takeoff and landing sorties of different aircraft types through the P/C of traffic coverage, it needs to be calculated for the main aircraft types of Airport A, respectively.

Based on the theoretical analysis under Section 3.4 aforementioned, given the B738 parameters, the main landing gear spacing of single-wheel B738 was set to T_W, and then the wheel track status of its left and right wheels was determined. If T_W was less than or equal to the passage width of aircraft pavement, the tracks of the left and right wheels did not coincide. In this process, the main landing gear spacing was 5.72 m, the wheel spacing was set to 0.86 m, and the standard deviation in the x direction took 0.775 m according to the data from Federal Aviation Administration (2012). The distribution function for the wheel track curve of the main landing gear spacing of B738 was as follows:

$$F(x) = \frac{1}{0.775\sqrt{2\pi}} e^{-1/2(x+3.29/0.775)^2} + \frac{1}{0.775\sqrt{2\pi}} e^{-1/2(x+2.43/0.775)^2}. \tag{9}$$

Through calculation, when $x = 2.86$ m, the maximum function value was 0.8827, the wheelmark width reached 0.296 m, and the P/C was about 3.83 based on Formula (7).

According to the above methods, the P/C of A320 and B737-700 was calculated and the results are summarized in Table 6. According to the number of allowable load actions for various aircraft calculated under Section 4.1, the CDF of the major aircraft can be calculated based on the actual traffic volume of Airport A in 2017, as shown in Table 6.

In this paper, the annual average growth rate of different aircraft models in the airport pavement evaluation stage was 0.20 based on trend extension method. In this way, the number of annual aircraft operations in future can be estimated and the cumulative pavement damage can be calculated (see Table 7 for details). Given the predicted average annual cumulative damage of 0.2568 and the remaining fatigue strength of 0.2958, the remaining life of pavement was predicted to be 0.2958/0.2568 = 1.15 years. The Airport A has been shut down for maintenance and renovation in 2019, which was consistent with the remaining life predicted in this paper.

Table 5: Mean and coefficient of variation of the random variables.

Random variable	Surface thickness	Flexural strength	Modulus of surface course	Modulus of base reaction
Mean	0.38 m	4.5 MPa	38.54 GPa	100 MPa
Coefficient of variation	0.03	0.15	0.09	0.3

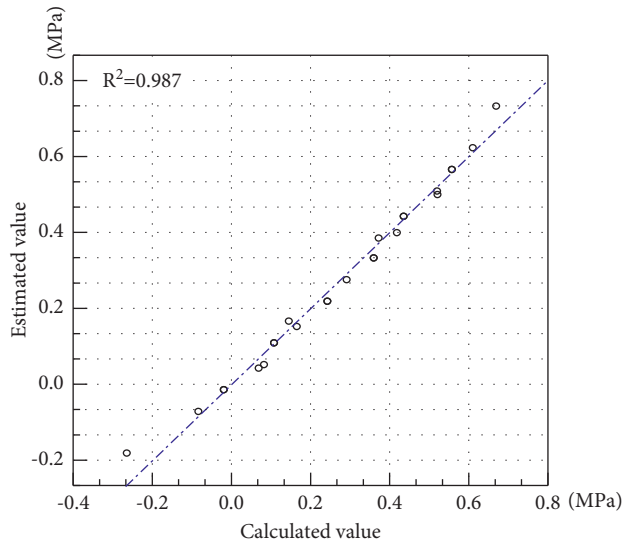

Figure 5: Comparison between the response surface estimation value and the finite element true value (B738).

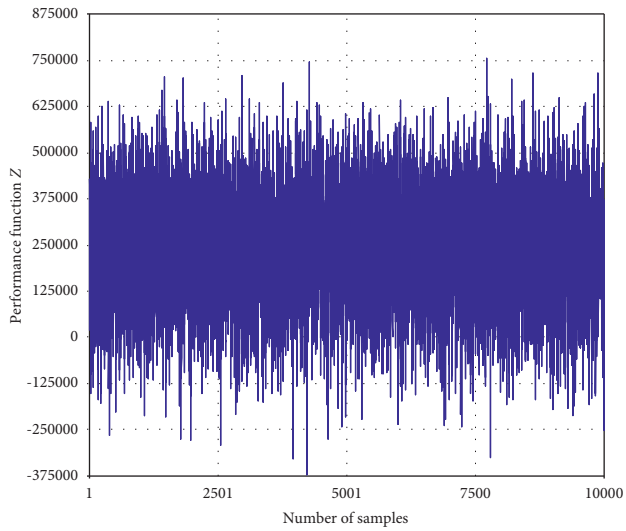

Figure 6: Sampling value distribution diagram of performance function Z (B738).

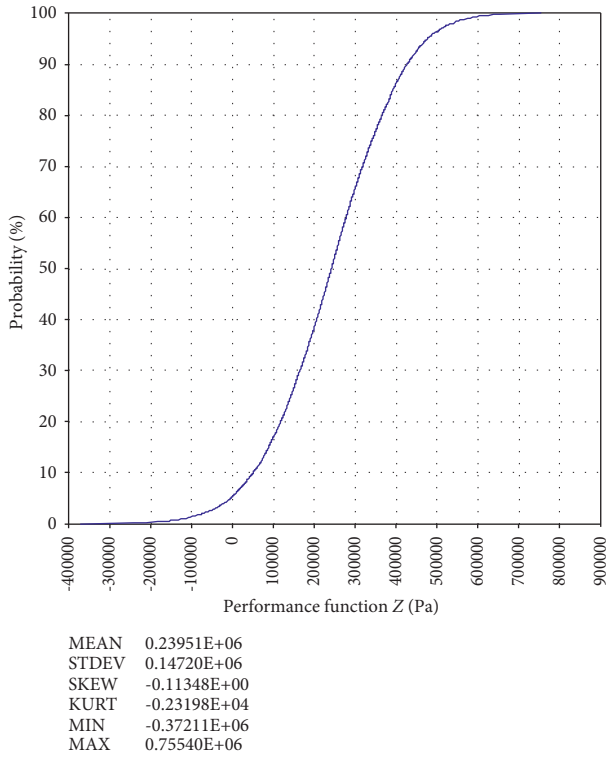

Figure 7: Cumulative probability distribution diagram of performance function Z at 95% reliability level (B738).

Table 6: Summary on the P/C and CDF of different aircraft.

Airplane	B737-800	A320	B737-700
Tire contact width W_t (m)	0.296	0.235	0.287
Value of x	2.86	3.8	2.86
Maximum probability function value $F(x)$	0.8827	0.9071	0.8827
Pass-to-coverage ratio P/C	3.83	4.69	3.95
Number of allowable load actions	133195	4175184	477806
Number of actual cumulative coverages	91584	34186	9837
CDF	0.6876	0.0082	0.0085
Sum of cumulative fatigue consumption of each model $\sum$CDF		0.7042	
Remaining fatigue strength of pavement		0.2958	

Table 7: Prediction for the annual average cumulative damage of different aircraft models.

Airplane	B737-800	A320	B737-700
Number of annual average operations in future	125737	57474	13929
Pass-to-coverage ratio P/C	3.83	4.69	3.95
Number of annual repeated actions	32830	12255	3526
Maximum number of allowable actions	286719	96762	1162864
Fatigue consumption	0.2465	0.0029	0.0074
Sum of the fatigue consumption of each model		0.2568	

Note. The data in the table were those predicted of an airport in 2017.

5. Conclusions

In this paper, the remaining life prediction method of airport runway was analyzed. The operation process of MEPDG was analyzed and summarized, and the MEPDG correction method was applied to the remaining life prediction of the airport runway. Since the airport runway was different from the expressway, the reliability calculation method of finite element numerical analysis was used to deal with the design stress of pavement plate edge that met 95% target reliability. The remaining life of airport runway was analyzed based on the actual data from the MEPDG correction method. The main conclusions were as follows:

(1) According to the theory of structural reliability, the performance function of airport pavement was obtained based on the limit state equation represented by flexural stress; the calculation formula of the number of allowable load actions can be obtained based on reliability by NCHRP126 fatigue equation without considering the temperature stress when the flexural fatigue strength of pavement plate cement concrete was less than $1.25 f_{cm}$.

(2) This paper selected a runway of the civil airport in Henan as the application case and adopted the MEPDG correction method. The flexural stress of the actual operating airport runway pavement at 95% reliability level was analyzed based on the mechanical numerical model of airport runway, and the number of allowable load actions of three aircraft models was obtained; given the impact of P/C, the CDF of the major aircraft models was calculated; the annual average growth rate of different aircraft models in the airport pavement evaluation stage was 0.20 obtained based on the trend extension method. In this way, the number of annual aircraft operations in future can be estimated and the cumulative pavement damage could be calculated. Given the predicted average annual cumulative damage of 0.2568 and the remaining fatigue strength of 0.2958, the remaining life of pavement was predicted to be 1.15 years. Airport A has been shut down for maintenance and renovation in 2019, which was consistent with the remaining life predicted in this paper.

Data Availability

The figure and table data used to support the findings of this study are included in the paper. In addition, the data and the models of analysis are available from the corresponding author upon request.

Conflicts of Interest

The authors declare that there are no conflicts of interest regarding the publication of this paper.

Acknowledgments

This research was funded by the Key Research Program in Universities of Henan Province (No. 21B580008) and the Science and Technology Project of Henan Province (No. 182102310747), for which the authors are grateful.

References

[1] Z. S. Quan, Q. Wang, and Z. X. Wu, *Intelligent Technology and Industrial Application*, pp. 268–270, Shanghai Science and Technology Press, Shanghai, China, 2019.

[2] H. Huang, M. Huang, W. Zhang, S. Pospisil, and T. Wu, "Experimental investigation on rehabilitation of corroded RC columns with BSP and HPFL under combined loadings," *Journal of Structural Engineering*, vol. 146, no. 8, Article ID 04020157, 2020.

[3] M. Y. D. M. Shahin, "Development of a pavement maintenance management system," *Airfield Pavement Distress Identification Manual. concrete pavements*, vol. II, 1976.

[4] T. Freeman and G. B. Dresser, *Update: Implementation of the Micropaver Pavement Management System on texas Division of Aviation Airfields*, Texas A&M University, College Station, Texas, 1999.

[5] L. J. Sun and X. P. Liu, "General deterioration equation for pavement performance," *Journal of Tongji University*, vol. 5, pp. 512–518, 1995.

[6] S. A. Kwon, H. S. Yang, and Y. C. Suh, "Development of fatigue model for airfield concrete pavement," *International Journal of Highway Engineering*, vol. 6, no. 3, pp. 27–35, 2004.

[7] J. M. Ling, Y. F. Zheng, and J. Yuan, "Prediction model of remaining life for asphalt concrete pavement of runway," *Journal of Tongji University*, vol. 4, pp. 56–59, 2004.

[8] M. A. Mooney, V. Khanna, J. Yuan, T. Parsons, and G. A. Miller, "Web-Based pavement infrastructure management system," *Journal of Infrastructure Systems*, vol. 11, no. 4, pp. 241–249, 2005.

[9] H. P. Bell, I. L. Howard, R. B. Freeman, and E. R. Brown, "Evaluation of remaining fatigue life model for hot-mix asphalt airfield pavements," *International Journal of Pavement Engineering*, vol. 13, no. 4, pp. 281–296, 2012.

[10] R. Ji and B. Sheng, "Reliability considerations of airport concrete pavement design using variation of back calculated modulus," in *Proceedings of the International Conference on Transportation and Development 2018: Airfield and Highway Pavements*, pp. 45–55, Pittsburgh, Pennsylvania, USA, July 2018.

[11] D. R. Brill and I. Kawa, "Advances in FAA pavement thickness design software: FAARFIELD 1.41," in *Proceedings of the International Conference on Highway Pavements and Airfield Technology 2017*, pp. 92–102, Philadelphia, Pennsylvania, USA, August 2017.

[12] H. Zhao, L. Ma, and J. Zhang, "Estimating the remaining life of airfield flexible pavements considering environmental factors," *HKIE Transactions*, vol. 25, no. 3, pp. 208–216, 2018.

[13] R. L. Lytton, "Concepts of pavement performance prediction and modeling," in *Proceedings of the Second North American Conference on Managing Pavements*, Toronto, Canada, November 1987.

[14] R. G. Mishalani and S. M. Madanat, "Computation of infrastructure transition probabilities using stochastic duration models," *Journal of Infrastructure Systems*, vol. 8, no. 4, pp. 139–148, 2002.

[15] Y. N. Yang, H. J. Pam, and M. M. Kumaraswamy, "Framework development of performance prediction models for concrete bridges," *Journal of Transportation Engineering*, vol. 135, no. 8, pp. 545–554, 2009.
[16] K. Kobayashi, K. Kaito, and N. Lethanh, "Deterioration forecasting model with multistage Weibull Hazard functions," *Journal of Infrastructure Systems*, vol. 16, no. 4, pp. 282–291, 2010.
[17] C. L. Ji and H. L. Zhang, "Introduction to asphalt pavement mechanics - empirical design method (MEPDG)," *Journal of Highway and Transportation Research and Development*, vol. 12, no. 10, pp. 119–121, 2016.
[18] China Communications Highway Planning and Design Institute Co., Ltd, *JTG D40-2011 Specifications for Design of Highway Cement concrete Pavement*, China Communications Press Co., Ltd., Beijing, China, 2011.
[19] L. C. Cai, H. F. Wang, and L. L. Zhang, "Prediction model of remaining life for airport pavement based on cumulative damage," *Journal of Traffic and Transportation Engineering*, vol. 14, no. 4, pp. 1–6, 2014.
[20] K. Izydor, "Pass-to-Coverage computation for arbitrary gear configuration in the FAARFIELD program. SRA, International. Federal Aviation Administration," Report No. DOT/FAA/TC-TN12/47, 2012.
[21] Federal Aviation Administration, "Airport pavement design and evaluation," Advisory Circular (AC) 150/5320-6F, November 10, 2016.
[22] L. L. Zhang, *Geotechnical Engineering Reliability Theory*, Tongji University Press, China, 2011.
[23] G. Mingzhong, H. Haichun, X. Shouning et al., "Discing behavior and mechanism of cores extracted from Songke-2 well at depths below 4,500 m," *International Journal of Rock Mechanics and Mining Sciences*, vol. 149, Article ID 104976, 2022.
[24] L. Li and G. P. Cen, "Effect of parameter design value on reliability of airfield cement concrete pavement," *Sichuan Building Science*, vol. 34, no. 4, pp. 89–92, 2008.
[25] S. H. Guo, *Research on the Reliability Evaluation Method of Cement concrete Pavement Structure*, Harbin Institute of Technology, Harbin, 2014.
[26] M. Z. Gao, J. Xie, Y. N. Gao et al., "Mechanical behavior of coal under different mining rates: a case study from laboratory experiments to field testing," *International Journal of Mining Science and Technology*, vol. 31, no. 2021, pp. 825–841, 2021.
[27] L. Li, *Research on Reliability Design Method of Airport Cement concrete Pavement*, Air Force Engineering University, Xi'an, China, 2006.
[28] M. Saeed, *Finite Element Analysis: ANSYS Theory and Applications*, Electronic Industry Press, China, 4th edition, 2015.
[29] D. C. Montgomery, *Design and Analysis of Experiments*, Wiley, New York, NA, USA, 2003.